Mechanisms of Vapor Absorption into Hygroscopic Liquid Desiccant Droplets

王, 振英

https://doi.org/10.15017/2534404

出版情報：Kyushu University, 2019, 博士（工学）, 課程博士
バージョン：
権利関係：

Mechanisms of Vapor Absorption into Hygroscopic Liquid Desiccant Droplets

Zhenying Wang

Thesis submitted for the degree of
Doctor of Engineering
at
Kyushu University

九州大学
KYUSHU UNIVERSITY

Acknowledgments

At the start of this thesis, I would like to express my sincere thanks to the many people who have instructed me, helped me, encouraged me, and inspired me in the past years.

I would like to express my sincere appreciation to Prof. Yasuyuki Takata, my supervisor during the PhD study. He is an intelligent scholar, an excellent leader, and a far-sighted advisor. I am deeply grateful for the many precious visiting and conference opportunities provided by him. I also benefit a lot from the many thoughtful advices from him both in the research and in my self-development.

I would like to express my heartfelt thanks to Dr. Daniel Orejon, who has helped and instructed me in the experimental part. He is always patient and modest, and would like to listen to my thoughts and provide valuable advices. I am also greatly affected by his meticulous research attitude and always-positive lifestyle.

I am very much indebted to Dr. Prashant Valluri, and Dr. George Karapetsas. During my staying in Edinburgh, we worked closely on the simulation part. I can never forget our problem shooting together into the deep night of Christmas eve. Their passion for research greatly infected me, and strengthened my confidence to do more challenging research.

I have to express my deep gratitude to Prof. Khellil Sefiane. He can always point out the key weaknesses in my research, and taught me how to tell a good academic story. I am also grateful for the many helps from him during my staying in Edinburgh, and for his valuable advices and instructions in my future career.

My sincere thanks also goes to the exceptional individuals in the Thermofluid Physics Laboratory. Dr. Hidaka helped me a lot in the preparation of experimental materials. Shuto-san provided the warmest help for my living and studying in Japan. I also want to express my gratitude to Alex-san, Shen-san, Kita-san and Harish-san, who

offered valuable suggestions to my research work. We also spent a lot of joyful and memorable time together during our lab activities.

I am forever indebted to the many teachers who have guided me in the past twenty years. I always feel lucky for being a student of them. I appreciate the knowledge and life experiences they taught me, which will be my lifelong treasures.

My special gratitude also goes to Prof. Zhen Li, Prof. Xing Zhang, Prof. Zengyuan Guo, and Prof. Bingyang Cao. They are my respected seniors and supervisors in Tsinghua, who provided valuable instructions to my master study, and continuously cared for me after my graduation.

Lastly, I want to express my sincere love and gratitude to my family, my grandma, my mom and dad, and my little sister. They are my power sources. Due to my studying abroad, I felt guilty for my lack of companions to them, but they are always considerate, and are in favor of any decisions made by me. I also have to express my special thanks to my husband, Dr. Qinyi Li. He is the best listener and the timeliest advisor for me. My life would not be so colorful without his companions and selfless contributions.

Abstract

Liquid desiccant is one type of salt solution characterized by its hygroscopic properties, which has been widely applied in the fields of air conditioning, heat recovery, and desalination. This thesis focuses on the physical process of vapor absorption into hygroscopic liquid desiccant droplets. Especially, we reveal the droplet kinetics, the motion of contact line, the heat and mass transfer, as well as the evolution of interfacial parameters of absorptive droplets.

Experiments on hydrophobic and hydrophilic substrates aim to reveal the effect of surface wettability on the droplet behaviors and on the rate of vapor absorption. Results show that droplets grow in a quasi-constant-contact-angle mode on hydrophobic PTFE substrates, while apparent droplet spreading is observed on hydrophilic glass substrates. Moreover, the rate of vapor absorption is higher on hydrophilic substrates than that on hydrophobic ones owning to the apparently shorter characteristic length of solute diffusion within the droplets. Besides, the slowly-spreading phenomena of droplets on hydrophilic glass substrates are explained based on a force balance analysis at the triple contact line, by the evolution of liquid-gas surface tension, and by the development of a precursor film during vapor absorption.

The coupled heat and mass transfer process is then investigated combining optical imaging and infrared thermography. Results show that the droplet experiences the highest temperature right after contacting the substrate owning to the rapid vapor absorption during droplet deposition. The droplet then gradually cools down as a joint result of heat dissipation and decreasing rate of vapor absorption. The vapor pressure difference between the droplet interface and the ambient is further evaluated combining the evolution of interfacial temperature and solute concentration. The results explain the saturation increasing trend of droplet volume along with time for six representative experimental conditions. Besides, a summary is given to elucidate the similarities and

differences between droplet evaporation and vapor absorption.

For better understanding the droplet dynamics during vapor absorption/desorption, a lubrication model is developed by direct numerical simulation, and solved with finite element method. The model allows for the free motion of contact line with the assumption of a precursor film in front of the droplet bulk. The simulation results reveal the distribution of mass flux across the droplet surface, and also demonstrate the evolutions of droplet profile, interfacial temperature, interfacial water concentration, and surface tension along with time. We further relate the contact line motion with the decomposed interior flow, which explains the spreading phenomena of hygroscopic droplets on hydrophilic substrates along with vapor absorption and desorption.

Key words: vapor absorption, liquid desiccant droplet, wetting and spreading, heat and mass transfer, lubrication model, finite element method

Contents

Nomenclature

Acronyms

CCA	Constant Contact Angle
CCR	Constant Contact Radius
FEM	Finite Element Method
LHS	Left Hand Side
PTFE	Polytetrafluoroethylene
RH	Relative Humidity
RHS	Right Hand Side
TCL	Triple Contact Line

Physical properties

α	Thermal diffusivity	$m^2\ s^{-1}$
c_p	Specific heat capacity	$J\ kg^{-1}\ K^{-1}$
D	Diffusion coefficient	$m^2\ s^{-1}$
g	Acceleration of gravity	$m\ s^{-2}$
k	Thermal conductivity	$W\ m^{-2}\ K^{-1}$
κ	Radius of curvature	m
M	Molecular weight	$g\ mol^{-1}$
P	Pressure	Pa
ρ	Density	$kg\ m^{-3}$
θ	contact angle	
S_q	Surface roughness	m
t	Time	s
T	Temperature	K
μ	Dynamic viscosity	Pa s
σ	Surface tension	$N\ m^{-1}$
χ	Concentration	

Other variables

L_{vl}	Latent heat of water vaporization	J kg^{-1}
J	mass flux	kg m^{-1} s^{-1}
Φ_q	Heat flux	W m^{-2}
V	Droplet volume	m^3

Dimensional analysis

$\hat{x}$	Dimensional variable
x	Dimensionless variable

Subscripts and superscripts

amb	Ambient
e	Equilibrium state
g	Gas phase
G	Gravity
LS	Liquid-solid interface
LV	Liquid-vapor interface
ref	Reference state
s	Droplet surface
sat	Saturation state
SV	Solid-vapor interface
v	Vapor phase

Dimensionless numbers

$\mathcal{A}$	Hamaker number	$\mathcal{A} = \dfrac{\hat{\mathcal{A}}}{6\pi\hat{\mu}_{H_2O}\hat{u}^*\hat{R}_0\hat{H}_0}$
ε	Droplet aspect ratio	$\varepsilon = \dfrac{\hat{H}_0}{\hat{R}_0}$

E	Evaporation number	$E = \frac{\hat{D}_{\mathrm{H_2O}} \hat{R}_0 \Delta\chi_{\mathrm{H_2O}}}{\hat{H}_0^2 \hat{u}^*}$
Kn	Knudsen number	$\mathrm{Kn} = \frac{\hat{\rho}_{\mathrm{H_2O}} \hat{D}_{\mathrm{H_2O}} \Delta\chi_{\mathrm{H_2O}}}{\hat{H}_0 \hat{p}_{\mathrm{v,sat}}} \left(\frac{2\pi \hat{R}_g \hat{T}_g}{\hat{M}_{\mathrm{H_2O}}} \right)^{1/2}$
Ma	Marangoni number	$\mathrm{Ma} = \frac{\hat{\eta}_\sigma \Delta\chi_{\mathrm{H_2O}}}{\hat{\sigma}_{\mathrm{H_2O}}}$
Pe	Péclet number	$\mathrm{Pe} = \frac{\hat{u}^* \hat{R}_0 \hat{\rho}_{\mathrm{H_2O}}}{\hat{D}_{\mathrm{H_2O}}}$
Pr	Prandtl number	$\mathrm{Pr} = \frac{\hat{\mu}_{\mathrm{H_2O}} \hat{c}_{p,\mathrm{H_2O}}}{\hat{k}_{\mathrm{H_2O}}}$
Re	Reynolds number	$\mathrm{Re} = \frac{\hat{\rho}_{\mathrm{H_2O}} \hat{u}^* \hat{H}_0}{\hat{\mu}_{\mathrm{H_2O}}}$
St	Stokes number	$\mathrm{St} = \frac{\hat{\rho}_{\mathrm{H_2O}} \hat{g}_{\mathrm{G}} \hat{H}_0^3}{\hat{\mu}_{\mathrm{H_2O}} \hat{u}^* R_0}$

Part I Introduction

Chapter 1 Introduction

1.1. History

Wetting, spreading, and phase change are common phenomena in the natural world, and have been of interest to scientists for a long time. Up to the early 1800s, Thomas Young [1] investigated the wetting phenomena of liquid in contact with a solid, and developed the theory of capillary phenomena on the principle of surface tension. Young's theory provided a qualitative explanation to the various interfacial phenomena in three phase fluid systems. Later in 1805, Pierre-Simon Laplace[2] completed the mathematical description which relates the concept of surface tension and the capillary action. In 1830, the German Mathematician, Carl Friedrich Gauss, unified their work and derived the differential equation[3], known as the Young-Laplace equation.

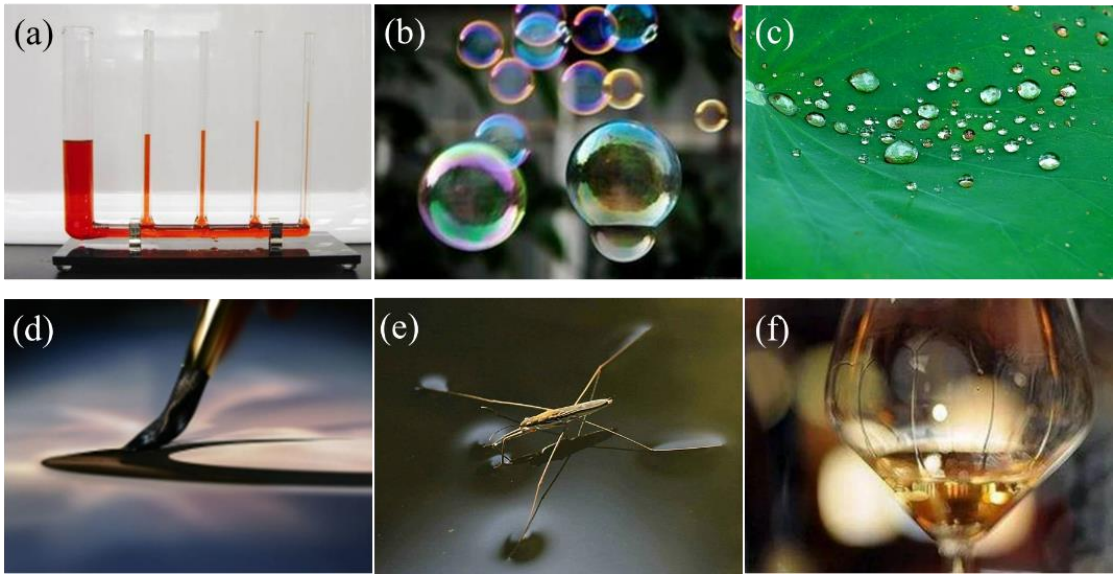

Figure 1.1 Commonly observed phenomena as evidences of surface tension. (a) Liquid height in a capillary tube is inversely proportional to the inner diameter; (b) Colorful soap bubbles stay stable in air; (c) Dewdrops on a lotus leaf show spherical shapes and are easy to fall off; (d) A brush pen takes up ink by the capillary effect, and generates homogeneous ink marks by the balance between adhesion force and capillary force; (e) A gerridae walks freely on water surface; (f) Tears of wine form due to surface tension gradient induced by preferential solute evaporation.

The Young-Laplace equation describes the capillary pressure difference sustained across the interface between two static fluids, and relates the shape of the surface with the interfacial surface tension. Shown in Figure 1.1, due to the effect of surface tension, bubbles are generated from surfactant-water mixture, and the tendency to minimize surface energy pulls the bubbles into spherical shapes. On a lotus leaf with nanostructures, dewdrops show spherical shapes due to the stronger wall tension at the droplet interface compared to the much lower adhesion force of the leaf surface. In capillary tubes, the liquid level is higher than the height of open water, and the surface height is inversely proportional to the inner diameter as a joint result of the adhesion force of wall and the surface tension at the liquid surface. Other commonly observed phenomena or application of surface tension also include the water striders, and the writing brushes which take use of the balance between the adhesion force of paper to ink and the capillary force of the pen hair.

When involving phase change at the liquid surface, the interfacial phenomena become more complex and interesting. The liquid-vapor phase change involves heat and mass transfer, and induces surface tension gradient due to the non-uniform distribution of interfacial temperature or solute concentration. Commonly observed tears of wine is a representative phenomenon of solutal Marangoni effect induced by surface tension gradient due to the preferential solute evaporation[4].

As a common phenomenon in daily life, the liquid droplet acts as an ideal object to investigate both the contact line kinetics and phase change at the liquid-air interface. In the late nineteenth century, James Clerk Maxwell firstly derived the equation of droplet evaporation induced by vapor diffusion[5]. In this model, Maxwell considered the simplest case where a motionless spherical bulb of pure water contacts with an infinite uniform air bulk. In 1915, Langmuir pointed out that there is a rapid concentration change of water vapor at the surface of an evaporating droplet[6]. Taking account of the effect of concentration change on evaporation, the evaporation rate can be approximated by the interchange of molecules within a thin layer adjacent to the droplet surface, and then by

vapor diffusion described with the Fick's equation[7]. In 1977, Picknett and Bexon[8] proposed that the evaporation of droplets can be distinguished with two pure modes: at constant contact angle (CCA) and at constant contact area or radius (CCR). They then derived prediction equations for the evaporation rate and residual mass of droplets by theoretical analysis, which showed good correspondence with the experimental measurements for a wide range of contact angles.

In 1997, Deegan et. al.[9]-[11] proposed an important theory for the formation of coffee stain from evaporating suspension liquid droplets. The important work revealed the interesting mechanisms underneath the commonly observed daily phenomena, and opened up a new avenue for the study of interior microflow and the particle self-assembly in the drying out process of different types of droplets. In 2002, Hu and Larson[12] derived an analytical solution to predict the evaporation rate by theoretical analysis and by computations with the Finite Element Method (FEM). The approximation equations, $\dot{m}(t) = -\pi RD(1 - \dot{RH})c_{\mathrm{v}}(0.27\theta^2 + 1.30)$, agreed well with the theoretical results by Picknett and Bexon[8] for any initial contact angle between 0 and $\pi/2$. In the subsequent studies of droplet evaporation, the Hu and Larson's equation is widely applied as a theoretical comparison with the experimental evaporation rate of pure liquid droplets.

The evaporation of droplets in contact with solid surfaces is a common and seemingly simple phenomenon, while there are a lot more interesting mechanisms worth exploring underneath. Firstly, the system is a gas-liquid-solid three phase system, which involves interfacial problems especially at the liquid-gas interface. When water evaporation takes place, the water-vapor phase change induces an effect of evaporative cooling at the droplet surface. Due to nonuniform evaporation flux and flow instability, interfacial phenomena such as Marangoni flow and triggered hydrothermal waves appear. The Marangoni flow is induced by the surface tension gradient due to temperature or concentration difference across the droplet surface. Hu and Larson studied the effects of Marangoni stresses on the interior flow in an evaporating sessile droplet using a lubrication-type model[13], and pointed out the reversing effect of Marangoni flow on the

coffee-ring formation[14]. Sefiane et. al.[15] reported the self-excited hydrothermal waves in evaporating sessile droplets using infrared thermography. Different from previous observations of hydrothermal waves in shallow liquid layers subjected to an imposed temperature gradient, the thermal pattern observed in droplets is a natural consequence of the evaporation, and both the temperature gradients and the drop thickness vary spatially and temporally. Later, Karapetsas et. al.[16] proposed a theoretical explanation for the observed thermal patterns using a linear stability analysis of a lubrication-type model.

The properties of solid substrates, such as the surface wettability, temperature, heat conductivity, etc., also proved to influence the droplet behaviors a lot. Regarding the effects of solid substrates, Dunn et. al.[17], Sobac et. al. [18], Sefiane et. al.[19], and David et. al.[20] revealed the thermal properties of the substrate on the evaporation rate by experiments and by numerical analysis. The surface roughness, on the other hand, influences the pinning and depinning behavior of the triple contact line, and is one candidate mechanism of the stick-slip phenomena of evaporating droplets[21][22]. The surface wettability directly decides the droplet profile and the contact area of sessile droplets with solid substrates. Depending on the surface wettability, the evaporating mode, the effective space for vapor diffusion, and the coefficient of heat transfer are all different. Therefore, proper empirical equations[23][24] should be sorted to accurately predict the evaporation rate of droplets with diverse contact angles. In recent years, the development of nanotechnologies makes it possible to realize superhydrophobic surfaces[25]. Studies of droplet evaporation on superhydrophobic surfaces with nanostructures have been carried out by McHale et. al.[24], Gelderblom et al.[26], Tam et al.[27], and Dash et al.[28]

In addition to single-component droplets, the evaporation of multi-component droplets is more complex and close to practical applications. The evaporation of colloidal droplets involves the formation mechanisms of residual patterns and the relevant microflow within the droplet bulk[29][30]. The evaporation of multi-component volatile droplets is more complex, where the solutal Marangoni flow comes into effect due to the preferential distribution of evaporation flux [31][32]. Moreover, due to the strong effect of

evaporative cooling, the absorption of water vapor towards the droplet surface have also been investigated[33][34].

All in all, the wetting and evaporation of sessile droplets is a diverse and promising subject. Research on this topic witnessed a rapid increase in recent years, and each sub-topic can be investigated intensively. Figure 1.2 gives an overview on all the research orientations extended from the basic concept of droplet wetting and evaporation. For more detailed understanding of each sub-topic, readers can refer to the excellent reviews by Erbil in 2012 (on the evaporation of sessile and suspended pure liquid droplets[35]), by Kovalchuk in 2014 (on the evaporation of sessile droplets[36]), by Sefiane in 2014 (on the patterns from drying droplets[37]), by Zhong et al. in 2015 (on the evaporation and pattern formation of nanofluid droplets[38]), by Mampallila and Eral in 2018 (on the utilization and suppression of coffee-ring effect[39]), and by Parsa et al. in 2018 (on the Mechanisms of pattern formation from dried sessile drops[40]).

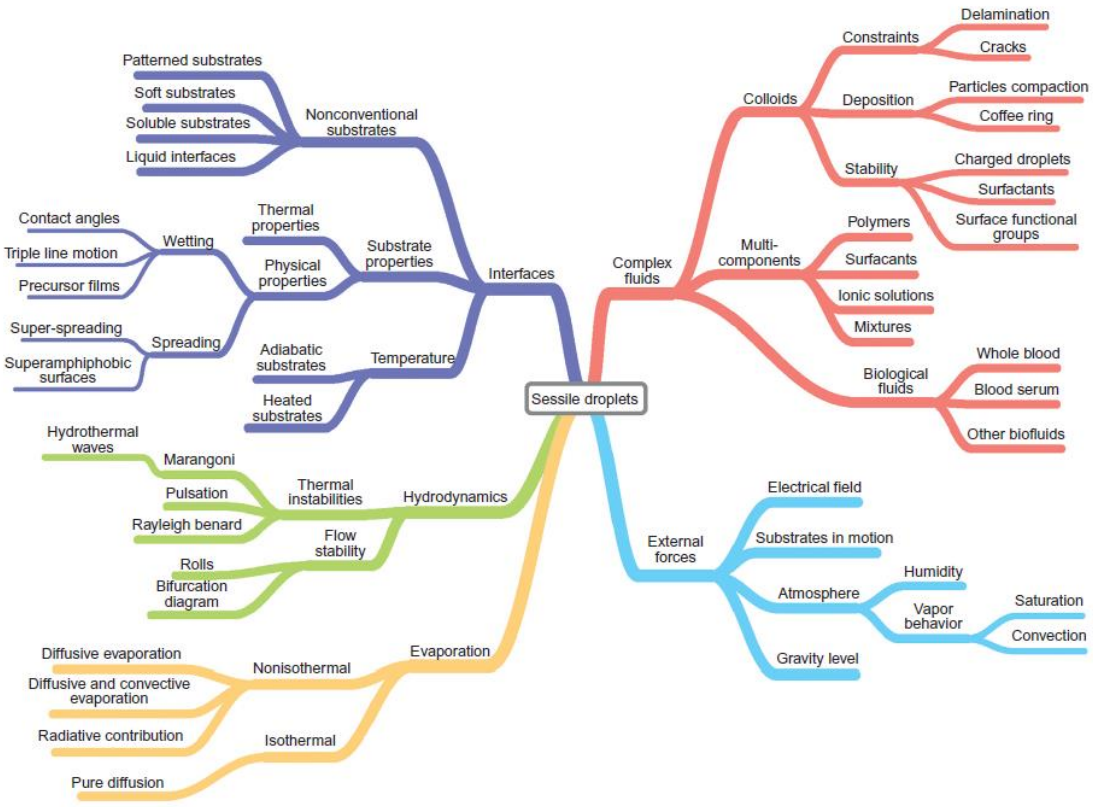

Figure 1.2 Overview of research topics on droplet wetting and evaporation[41][42].

1.2. Application background

The liquid desiccant investigated in this thesis is a type of aqueous salt solution characterized by its hygroscopic properties[43]. Taking advantage of this specific characteristic, a lot of practical systems have been developed both for domestic and industrial uses, which can be divided into two types: the close-type absorption heat pump systems[44] and the open-type dehumidification systems[45].

In the open-type dehumidification system, liquid desiccant directly contacts with humid air at normal atmospheric pressure. Due to the hygroscopic property of liquid desiccant, the water vapor contained in humid air is absorbed by liquid desiccant, and the air is dried. Taking use of the dehumidification capacity of liquid desiccant, systems combining dehumidifier, regenerators and different type of heat exchangers are developed for various uses, such as the liquid desiccant air conditioning system[46][47], the open-type system for waste heat recovery from industrial flue gases[48]-[50], the open-type desalination system[51], etc.

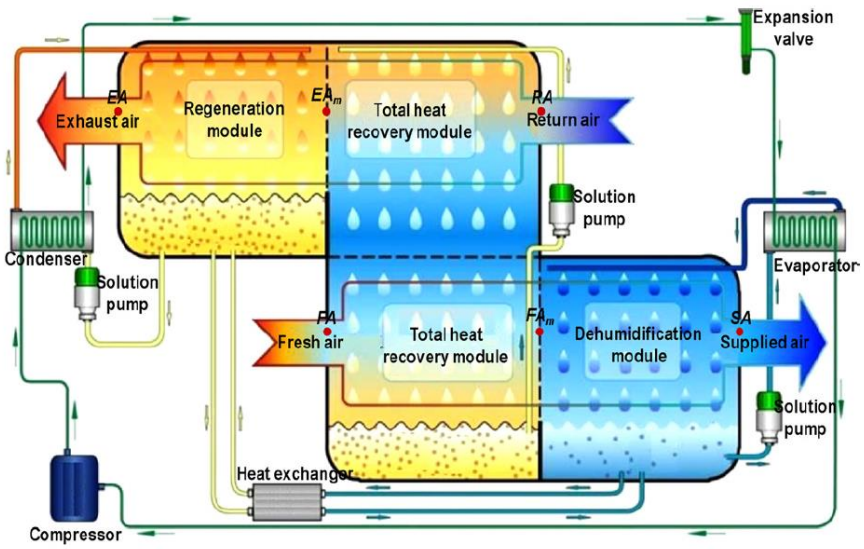

Figure 1.3 Schematic diagram of a typical liquid desiccant dehumidification system for air conditioning use. (Zhao, et al. [52])

The liquid desiccant air conditioning system makes it possible to independently control the temperature and humidity of indoor environments. Figure 1.3 shows the working principle of a typical liquid desiccant dehumidification system for air

conditioning use in hot and humid climatic regions. The system consists of three modules: a dehumidification module, a total heat recovery module, and a regeneration module.

In the dehumidification module, the humid air makes fully contact with strong liquid desiccant, and gets dehumidified. The dry air is then supplied to the temperature control units for indoor use. In the regeneration module, the hot diluted liquid desiccant contacts with dry return air, releases water vapor, and gets regenerated. The dry return air is humidified during the regeneration process, and emitted to the outdoor atmosphere. The liquid desiccant dehumidification system is usually combined with an independent temperature control unit, such as the radiant panel, etc. By separating the humidity control process and temperature control process, the system can avoid the cooling and reheating problems which happens in traditional compression refrigeration systems. Moreover, since the fresh air has already been dried by the dehumidification system, the radiant panel can work with high temperature chilled water, *e.g.* 17.5 °C, which greatly saves energy in the production process of chilled water.

(a) 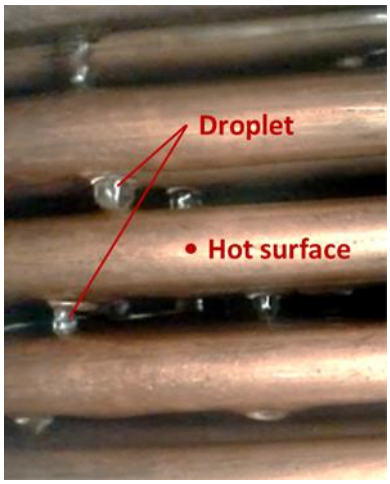

(b) 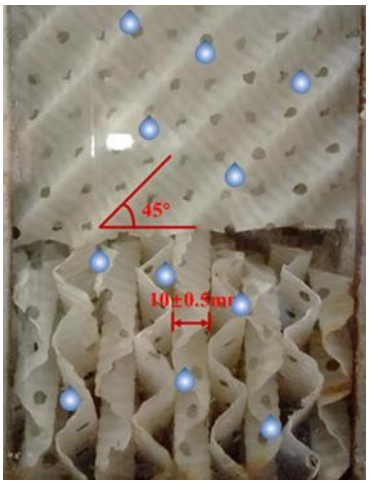

Figure 1.4 Inner structures of (a) a falling-film generator in an absorption heat pump, and (b) an adiabatic packed-type dehumidifier in a liquid desiccant dehumidification system.

In those practical systems, the components where liquid desiccant directly contacts with water vapor or humid air are crucial. Figure 1.4 (a) shows the inner structure of a falling-film generator in an absorption heat pump. Within the generator, liquid desiccant is evenly distributed to the copper coil from a solution distributor, and liquid desiccant

film forms on the surface of copper coils. Due to the effect of gravity, desiccant solution from the top coil accumulates and flows down in the form of droplets. Upon contact with the downward copper surface, the desiccant droplets spread and coalesces with the desiccant solution film on the downward surface. Heated by the hot fluid within the copper coil, liquid desiccant gets concentrated as it flows from top to bottom, and water vapor is generated at the same time.

Figure 1.4(b) shows the inner structure of an adiabatic packed-type counter-flow dehumidifier in a liquid desiccant dehumidification system[53]. Within the counter-flow dehumidifier, liquid desiccant flows from the top to the bottom of the packed tower, while the humid air flows inversely from bottom to top. During the process, the water vapor contained in the humid air is absorbed by liquid desiccant, and the liquid desiccant gets diluted. Moreover, due to the release of latent heat during the absorption process, the temperature of liquid desiccant increases.

Table 1.1 Summary of representative experimental studies on the heat and mass transfer process between humid air and liquid desiccant within adiabatic dehumidifiers.

Author	Desiccant type	Flow pattern	$\dot{m}_a$ (kg/(m^2 s))	$T_{a,in}$ (°C)	$\omega_{a,in}$ (g/kg air)	$\dot{m}_s$ (kg/(m^2 s))	$T_{s,in}$ (°C)	$x_{s,in}$ (wt.%)
Zurigat et al.[61]	TEG	Counter	1.50~2.61	25.4~44.0	16.1~21.8	0.13~0.82	25.0~45.5	93~98
Longo et al.[62]	KCOOH	Counter	0.48~0.52	22.6~35.8	8.8~20.7	0.09~1.23	21.9~24.8	73~74
Liu et al.[63]	LiBr	Cross	1.59~2.43	24.7~33.9	10~21	2.15~4.55	20.1~29.5	42~49
Moon et al.[64]	$CaCl_2$	Cross	0.91~1.99	26.8~39.0	16~24	1.26~2.57	26.2~38.2	33~43
Zhang et al.[65]	LiCl	Counter	Summer: 0.24; 0.48	34.5~35.6	14.9;15.3	0.050~0.106	14.0~16.8	30~40
			Winter: 0.25~0.48	6.31~7.49	2.73~2.94	0.050~0.079	-2.17~ -0.78	30~40
Gao et al.[66]	LiCl	Cross	0.53~0.93	27~38	9.3~21.3	3.33~8.67	22~50	32~40
Wang et, al.[53]	KCOOH	Counter	1.01	55-70	24~169	0.88~5.43	33-43	44-64

Up to now, most of the research concerning liquid desiccants addresses: the performance of dehumidifiers with different flow patterns[54][55], different type of inner packing[56][57], presence or absence of inner heat sources[58][59], and different desiccant solutions or ambient conditions[53][60], for practical applications. Some of the representative experimental studies on the heat and mass transfer process within adiabatic dehumidifiers are summarized in Table 1.1.

Despite of the existing studies at the macro scale, the performance of single liquid desiccant droplets during the vapor absorption process has been rarely reported. At the inlet of the dehumidifier, desiccant droplets are formed at the liquid distributor before impinging onto the inner packing. Upon impingement, discrete drops varying in size and shape appear at the top of the packing and flow down in a dropwise or filmwise fashion depending on the surface wettability. In practical applications, the inner fillers vary from light polymers, non-corrosive ceramics, to high-strength metals[67], which provide different surface wettability, therefore the flow regime of the desiccant solution inside also differs.

Studies on the vapor absorption process at the droplet scale make it possible to understand the behaviors of single droplet within the packed towers in more details. The conclusions will contribute both to a more accurate prediction of the vapor absorption process and to the optimization of practical dehumidification devices.

1.3. Organization of this thesis

This thesis aims to fully reveal the droplet kinetics, the contact line motion, the coupled heat and mass transfer process, and the governing mechanisms during vapor absorption into hygroscopic liquid desiccant droplets. Research is conducted combining experimental investigations and numerical simulations. A schematic of the thesis structure is shown in Figure 1.5. The context contains four main parts: Introduction, Experiments, Simulations, and Conclusions. d

In Part I “Introduction”, Chapter 1 presents the academic history (section 1.1) and

application background (section 1.2) of this research. A thorough literature review is given in Chapter 2, including the mechanisms governing droplet evaporation (section 2.1), the evaporation of ionic aqueous solution droplets (section 2.2), and the development of lubrication-type models for droplet evaporation (section 2.3). Based on the result of literature review, we propose the research topics and highlights the originality of this thesis (section 2.4).

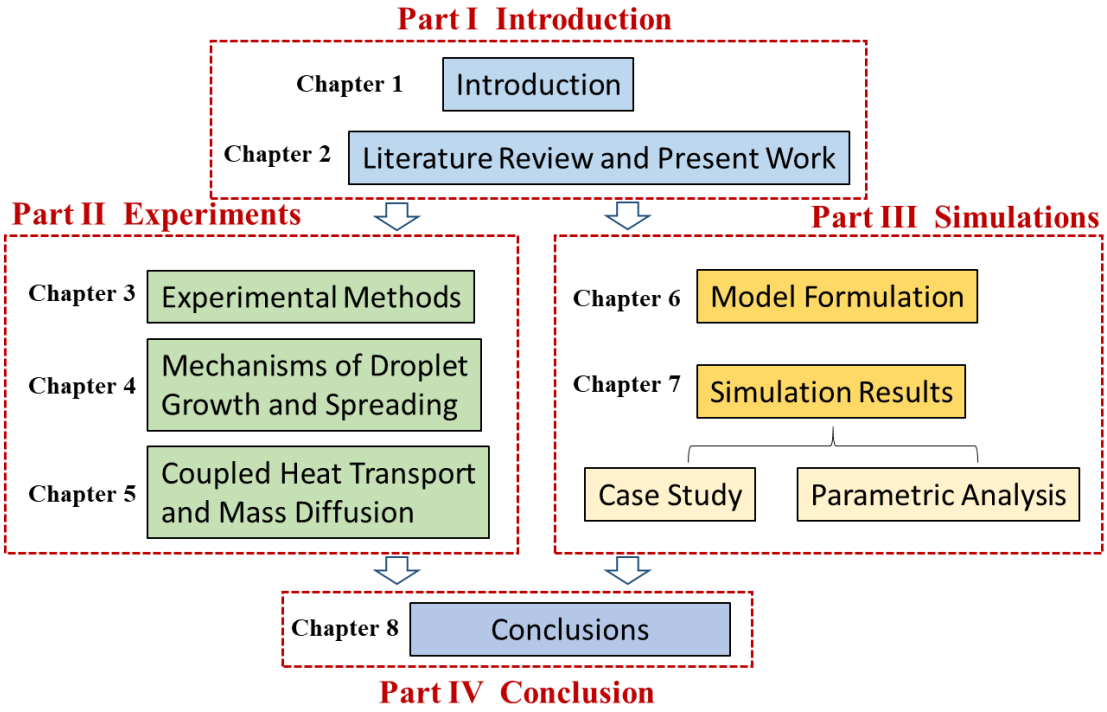

Figure 1.5 Structure of this thesis

Part II "experiments" presents the experimental methods and experimental results. The experimental details will be illustrated in Chapter 3, including system setup, measuring techniques, material preparation, and data analysis. Based on the experimental results, two important issues will be presented: the mechanism of droplet growth and spreading (Chapter 4), and the process of heat transport and mass diffusion (Chapter 5).

Numerical simulations are further carried out regarding the problems that have not been solved by experimental methods. Part III "Simulations" focuses on the development of a numerical model and presents the simulations results. Chapter 6 illustrates the detailed formulation of a lubrication-type model, including problem description, main

assumptions, and the derivation of the governing equations. Chapter 7 shows the simulation results, including model validation (section 7.1), case studies for two representative conditions (section 7.2), and parametric analyses of several important dimensionless numbers (section 7.3).

Part IV “Conclusions” summarizes the main conclusions of the thesis, and discusses the instructional significance of the droplet-scale study to practical dehumidification systems.

Chapter 2 Literature review and present work

2.1. Overview of droplet evaporation

A sessile droplet refers to a liquid droplet body sitting on a solid substrate, where a wetting area is formed constricted by the triple contact line. As a joint effect of the gravitational force and surface tension, the droplet will present as a compressed spherical cap. For a droplet with a contact radius smaller than the capillary length, the effect of gravity can be neglected, and the droplet can be regarded as an ideal spherical cap[68], which applies for most of the droplets discussed in this thesis.

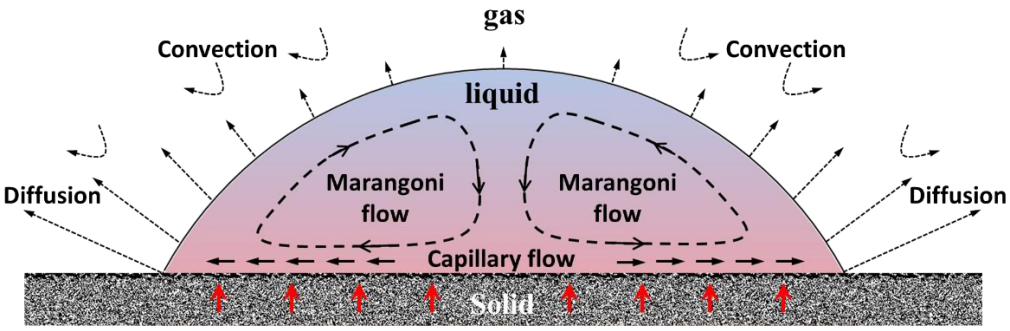

Figure 2.1 Schematic of an evaporating water droplet sitting on a solid substrate. Red arrow: direction of heat flux; Dotted arrow: mass flux by diffusion and convection; Dash arrow: direction of fluid flow induced by Marangoni effect; Solid arrow: direction of fluid flow induced by capillary effect; Gradient color within the droplet: temperature field from hot red to cold blue.

Research on droplet phase change involves both fluid dynamics and heat and mass transfer. Figure 2.1 describes the mechanisms governing the evaporation of a pure water droplet sitting on a solid substrate. In still air, the evaporation of water droplet is induced by vapor diffusion as a result of the concentration difference of water vapor between the saturated droplet interface and the unsaturated surrounding atmosphere. The evaporation mass flux at the droplet surface can be expressed as[69],

$$J(r,t) = D(\mathbf{n}\cdot\nabla c)\Big|_{z=h(r)}, \tag{2.1}$$

where J denotes the evaporation mass flux at the droplet surface, D denotes the diffusion

coefficient of water vapor in air, ∇c denotes the concentration gradient of water vapor on the air side, **n** is a unit vector normal to the free surface, *r* is the radial coordinate, *z* is the vertical coordinate, and *h*(*r*) defines the surface of the droplet.

Due to the geometric effect of droplet shape, the concentration field of water vapor distribute unevenly along the droplet interface, which can be analogized with an equivalent electrostatic problem[70], and can be solved with the steady-state Laplace equation, $\nabla^2 c = 0$, along with boundary conditions at the liquid-air and solid-air interfaces. Due to the non-uniform vapor concentration gradient and the variation of droplet height along the radius, the evaporative mass flux distributes unevenly across the droplet interface, and depends greatly on the contact angle. Derived from the Laplace equation, Deegan and co-workers[71][72] proposed that for contact angles less than 90°, the evaporation flux across the droplet surface can be approximated by a simple form,

$$J(r,t) = J_0(\theta) D\left(1-\tilde{r}^2\right)^{-\lambda(\theta)}, \tag{2.2}$$

where $\lambda(\theta)$ is a parameter denoting the uniformity of evaporation, and θ is the contact angle with units of radians. When the contact angle equals to 90°, $\lambda(\theta) = 0$, and the evaporation mass flux distributes uniformly across the droplet surface. For a droplet on a hydrophilic substrate with contact angle of 0~90°, Hu and Larson[73] derived the analytic solution for $\lambda(\theta)$ and $J_0(\theta)$.

$$\lambda(\theta) = \frac{1}{2} - \frac{\theta}{\pi}. \tag{2.3}$$

$$J_0(\theta) = \frac{Dc_v(1-RH)}{R}\left(0.27\theta^2 + 1.30\right)\left(0.6381 - 0.2239\left(\theta - \pi/4\right)^2\right), \tag{2.4}$$

where *RH* denotes the relative humidity of ambient air, and c_v is the saturation water vapor concentration.

By integrating eq. (2.2) along the droplet surface and combining eqs. (2.3) and (2.4), we arrive at an empirical correlation of the evaporation rate for droplets with pinned contact line on hydrophilic substrates, θ = 0° ~ 90°.

$$-\dot{m}(t)=\pi RD(1-RH)c_{v}\left(0.27\theta^{2}+1.30\right), \tag{2.5}$$

From eq. (2.5), it can be noticed that the evaporation rate is linearly proportional to the contact radius, R, and the concentration difference of water vapor, $(1-RH)c_v$. Moreover, the term containing θ, $\left(0.27\theta^{2}+1.30\right)$, indicates that the evaporation rate is weakly influenced by the contact angle, especially when the contact angle is less than 40° (0.7 rad), according to Hu and Larson's calculations. This means that for small contact angle less than 40°, the evaporation mass flux concentrates near the triple contact line, and is proportionally influenced by the perimeter of the contact line. Eq. (2.5) provides a fair prediction for the evaporation rate of droplets on hydrophilic substrates with pinned contact line, which corresponds well with the results of Picknett and Bexon[8], and is further discussed and developed in later studies[74]-[76] of pure water droplets evaporating in a constant contact radius (CCR) mode.

As indicated with solid arrows in Figure 2.1, the non-uniform distribution of evaporation mass flux across the droplet surface subsequently induces an outward flow within the droplet in the radial direction to replenish the greater water loss near the triple contact line. In the existence of colloid suspensions, the capillary flow will carry the suspension particle towards the contact line, and cause the commonly observed coffee ring depositions as initially revealed by Deegan, et, al.[9]

Along with droplet evaporation, the latent heat taken away due to phase change at the liquid-air interface tends to cool down the droplet surface. By taking account of the evaporative cooling effect, Dunn, Sefiane, and co-workers[17][77][78] proposed a modified model based on Hu and Larson's results, which reveals the strong effect of substrate conductivity and atmospheric condition on the evaporation rate. As a joint result of the heat of vaporization, the nonuniform path lengths for heat conduction, and the nonuniform distribution of evaporation mass flux, the temperature distribution across the droplet liquid-air interface is nonuniform, which further induces a surface tension gradient along the droplet interface. The surface tension gradient drives a thermal Marangoni flow across the droplet interface amd induces a circulation of microflow

within the droplet[13]. For a droplet sitting on a hydrophilic substrate, the direction of surface tension gradient is decided by two dominating factors, the characteristic length for heat conduction and the rate of evaporation. On the area near triple contact line, the distance for heat transfer from the substrate is short which tends to heat up the surface, while the evaporation mass flux is stronger which tends to cool down the surface. The study of Xu and Luo[79] shows that for a droplet evaporating on a hydrophilic substrate, a stagnation point exists at the droplet surface close to the triple contact line, where the surface flow, the surface tension gradient, and the surface temperature gradient change their directions. Further theoretical and experimental studies of Ristenpart, et. al., Xu, et. al., and Girard, et. al. revealed that the direction of Marangoni flow is also influenced by the droplet contact angle, the thermal conductivity of the liquid, as well as the thickness[80], the thermal conductivity[81] and the heating conditions of the substrate[82][83].

On a hydrophilic substrate with high thermal conductivity and with moderate contact angle as revealed in Figure 2.1, the local temperature at the area close to the substrate will be higher that the area far away from the substrate, *e.g.* near apex, due to shorter length for heat supply from the substrate. The temperature difference forms a surface tension gradient and subsequently induces an interfacial flow from the hotter droplet bottom near contact line to the colder top surface far away from the substrate. According to Hu and Larson's research[14], for clean interfaces, free from surfactant contamination, the interfacial flow induced by thermal Marangoni effect is strong enough to carry particles near the contact line toward the droplet top, and then plunges them downward where they can either adsorb onto the substrate near the center of the droplet or be carried along the substrate to the edge, where they are recirculated along the free surface back toward the top of the droplet. The circulation by thermal Marangoni flow induces a reversing effect to the coffee stain deposition opposite to the effect of capillary flow, which are further utilized to control the particle depositions in drying droplets. (See the work of Soltman et. al.[84], Thokchom et. al.[85], and Hendarto et. al.[86], etc.)

For pure water droplets, the Marangoni flow by is usually very weak, as water is well

known to highly attract surface-active agents. Therefore, the surface tension distribution is no longer sensitive to the small temperature difference induced by non-uniform evaporative cooling and heat conduction. By assistant uniform heating or local heating (by single point laser) from the substrate, the temperature gradient across the droplet surface can be strengthened, and apparent thermal Marangoni flow in water droplets is revealed in later studies[87]-[89] using Infrared thermography.

Other from thermal Marangoni effect due to temperature gradient, a solutal Marangoni effect can also be induced by the concentration gradient of solute in binary volatile droplets or in droplets with additional surfactant, which will be further discussed in section 2.1.2 on the evaporation of binary droplets.

The above description gives a brief overview of the physical mechanisms governing the evaporation of a pure liquid droplet. Other from the mechanisms mentioned above, along with time, the evaporation kinetics of pure liquid droplets is also greatly affected by the conditions of the underneath substrate. Depending on the surface roughness and surface structure, droplets evaporate in different modes. The widely accepted evaporation mechanisms, depending on the dynamics of the triple contact line, are the constant contact radius mode (CCR), the constant contact angle mode (CCA), and the CCR-CCA mixed mode[90][91]. Typically, the CCA mode happens on smooth hydrophobic substrates where the droplet contact line recedes while the contact angle remains constant to account for the liquid evaporated. On a hydrophilic and/or on a rougher substrate where the surface hysteresis is high, the triple contact line tends to be pinned while the contact angle decreases with time, namely, the CCR mode. In addition, during evaporation of nanofluid droplets[21][92] or pure fluid droplets on structured surfaces[93], a stick-slip behavior has been reported.

By taking account of the substrate wettability, Popov proposed an analytical diffusion model[23] for quasi-steady natural evaporation of a droplet based on the solution to the Laplace equation describing the concentration field at the droplet surface in a cylindrical coordinate system. Compared to Hu and Larson's model, Popov's model applies to the

full range of contact angles, and is more suitable for predicting the evaporation rate of droplets with large contact angles. In later studies of Dash et. al.[28][94], Gelderblom et. al. [95], Sobac et. al.[96], *etc.* on hydrophobic and superhydrophobic substrates, the experimental results show good correspondence with Popov's model, which well describes the distribution of evaporative mass flux across the droplet surface, and makes it possible to predict the lifetime of evaporating droplets with a wide range of contact angles[97].

2.2. Research on ionic aqueous solution droplets

In real applications such as ink-jet printing, medical diagnostics, internal combustion engine, and cosmetics, most of the droplets in action are not pure liquid droplets. Due to differential tendency of vaporization, the component of binary droplets changes both spatially and temporally, therefore the mechanisms are more complicated and intriguing. In this section, we review and summarize the existing studies on the evaporation of ionic solution droplets, which shares both similarities and differences with the vapor absorption process into hygroscopic ionic solution droplets.

Studies on the evaporation of ionic solution droplets mainly focuses on the evaporation behavior and on the crystalline deposits from drying droplets. Regarding the behavior of ionic solution droplet during evaporation, Soulie et al.[98] investigate the aqueous saline-water (NaCl-H_2O) solution droplets with different salt concentrations and contact angles. Their experimental results show the strong effect of small amount of salt addition to the pining of the contact line. The droplets evaporate following a constant contact angle mode, and the evaporation rate keeps almost constant for droplets with low salt concentrations. Moreover, they find that the evaporation rate is significantly lower for high salt concentrations and small contact angle, and attributed it to the Marangoni flows that are induced by surface tension gradient originating from the local evaporative periphery salt enrichment. Zhong et al.[99] concentrate on the effect of surface wettability on the evaporation of sessile saline droplets. On hydrophobic silicon wafer and poly plate,

the droplet experiences a constant contact radius model during the initial period, then the contact line starts to recede, the contact angle increases gradually until the salt precipitation. The increase in the contact angle is attributed to the increase of surface tension caused by increased salt concentration. On hydrophilic glass substrates, the droplet remains pinned throughout the droplet lifetime. Moreover, the crystalline patterns depend on the substrate wettability, which will be introduced later. Kuznetsov et al.[100] investigate the evaporation modes of several different saline solution droplets on aluminum surface. They summarize typical evaporation modes of studied aqueous salt solutions. Those are (1) increasing contact radius with decreasing contact angle, (2) pinning of the contact line, and (3) the formation of salt crystal (NaCl) or crystalline hydrates (LiBr, LiCl, and $CaCl_2$). Brenn[101] simulated the concentration distribution within aqueous salt solution droplets during evaporation, and proposed an analytic solution for this problem. Larger concentration gradient is reported at high evaporation rate, function of the radial coordinate. The conclusions are helpful for predicting the deposition morphology from drying droplet. Misyura[102][103] carried out experiments with aqueous salt solution droplets on smooth and structured heated surfaces. Results indicate the decreasing evaporation rate due to the decrease in vapor pressure at the droplet surface, which originates from the increasing salt concentration. The author then provides detailed analyses on the heat transfer and mass diffusion within the liquid layer, and points out the effect of crystallization on the evaporation rate.

On the other hand, the crystalline patterns from drying droplets have been investigated for its practical values in nano fabrication and salt damage prevention. Shahidzadeh et al.[104] study the evaporation and crystallization growth of sodium sulfate and sodium chloride in forms of droplets and square capillaries. The results indicate the strong effects of the wetting behavior of crystals on the crystallization growth and pattern evolution. On hydrophobic substrates, the crystallization pattern is more focused. On hydrophilic substrates, different levels of droplet spreading are observed which lead to the formation of crystallization patterns stretching from the drop edge. For sodium sulfate

droplets, an apparent precursor wetting film spreads from the drop edge, while for sodium chloride droplets, a slight droplet spreading is observed. Shahidzadeh et al.[105] further carried out experiments with sodium chloride and calcium sulfate droplets, and conclude that the salt crystal stains are mainly governed by the wetting properties of the crystal and the pathway of nucleation and growth. They also point out that the stain formation is independent of the evaporation rate and the thermal conductivity of the substrate. McBride et al.[106] investigate the formation of crystallization from evaporating droplets on superhydrophobic and liquid-impregnated surfaces. They summarize four disparate regimes to describe the interaction between calcium sulfate solution droplet and substrates with different solid fractions: Cassie-pinning, Cassie-gliding, Cassie-Wenzel transition, and Wenzel. Moreover, the morphology of the resultant crystal depositions differs depending on the regime of the droplet-substrate interaction. Kaya et al.[107] investigate the pattern formation in drying droplets of polyelectrolyte and salt. They present several different patterns from drying mixed droplet, including concentric rings, needle-like structure, chains of triangular-shaped crystallites, etc. They also propose a theoretical model to explain the occurrence of concentric rings during droplet evaporation. Gorr et al.[108] focus on the pattern formation during sessile droplet evaporation of aqueous lysozyme solutions with varying concentrations of NaCl. The results indicate three typical regions in the formed deposition which are similar with previous study of human biofluids. Moreover, increasing NaCl concentration will lead to a decrease in the width of the deposition due to earlier aggregation of particles. Harrington et al.[109] investigate the crystal patterns from a thin droplet of dilute NaCl solution (0.1 wt. % and 0.025 wt. %) on an air-cleaved mica surface. Ordered and structured crystal patterns are generated depending on the salt concentration. The method indicates application potential in surface patterning with technologically important crystals.

Figure 3.3 shows several typical crystallization patterns from drying droplets of different aqueous salt solutions. Depending on the type of salt and the wettability of the substrate, the crystallization patterns differ greatly. Studies on the crystallization

formation and deposition patterns will contribute to a better understanding on natural phenomena such as sea water corrosion and salt weathering. Research on complex fluids containing salt or protein is of significance to disease detection in the medical field. For a better understanding of different patterns from evaporating droplets, the reader is also referred to the review papers of Sefiane and Parsa et al.[110][111]

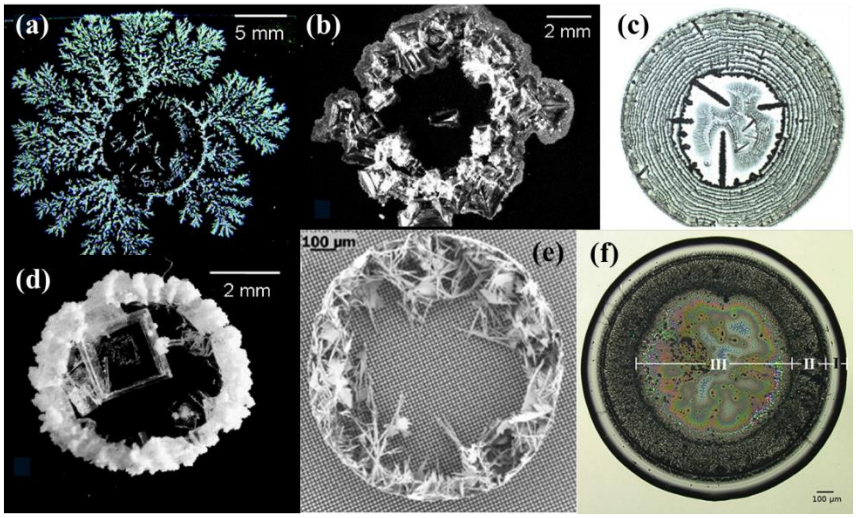

Figure 2.2 Examples of the crystalline patterns formed from drying aqueous saline solution droplet. (a) Saturated $NaSO_4$ droplets on a hydrophilic glass substrate.[104] (b) Saturated NaCl droplets on a hydrophilic glass substrate.[104] (c) Aqueous solution droplet of 0.5 g/l NaPSS and 0.1M salt on a hydrophilic glass substrate.[107] (d) Saturated NaCl droplets on a hydrophobic substrate.[104] (e) Droplet of saturated $CaSO_4$ solution on a superhydrophobic surface.[106] (f) Droplet of 1.0 wt.% lysozyme + 0.1 wt.% NaCl solution on a hydrophilic silicon wafer. [108]

2.3. Lubrication model for evaporating droplets

Droplet spreading is a moving-boundary problem which involves the interaction of liquid and air with an impermeable solid substrate. As a fundamental problem in fluid mechanics, the droplet spreading exemplifies the general problem of moving contact line, which covers a lot of common phenomena in our daily life and industrial applications. In the past decades, researchers developed a series of mathematical models for explicitly understanding the droplet dynamic during this process.

Besides the difficulties shared by most moving boundary problems, droplet

spreading with moving contact line presents additional complication as pointed out in the review by de Gennes[112]. Firstly, at the liquid-solid interface, there is an inherent contradiction in simultaneously assuming the no-slip boundary condition and expecting displacement between liquid and gas there, therefore a force singularity will arise at the moving contact line as revealed in the study of Dussan and Davis[113]. Secondly, the behavior of the contact line is experimentally evidenced to be function of the advancing speed. Reliable functions between the dynamic contact angle and the contact line motion are required to give a complete physical description of the problem.

The lubrication theory is a common approach for simplification in modelling fluid systems. This theory approximates the scale of one dimension as significantly smaller than the others, therefore the Navier-Stokes equations can be further simplified by omitting the first order small quantity. In 1978, Greenspan[114] developed a model for the movement of a small viscous droplet on a surface, which is based on the lubrication equations, and uses the dynamic contact angle to describe the forces acting on the fluid at the contact line. Greenspan's model relates the dynamic contact angle with the advancing speed of the contact line with a linear function, makes it possible to predict the behavior of contact angle in the presence of additional surface adhesion, and also explains the distortion of droplet shape due to surface contamination. In 1991, Ehrhard and Davis[115] further developed Greenspan's model by taking account of the effect of gravitational force and thermocapillary force. Their model generalized the relationship between the advancing contact angle and the speed of contact line based on the empirical correlations derived by former researchers (e.g. Tanner in 1979[116], Cazabat and Stuart in 1986[117], Chen and Wada in 1989[118], etc.). The numerical results revealed the thermocapillary flow induced by substrate heating, which counteracts with the flow associated with isothermal spreading, and retards the spreading process of thin droplets. Subsequently, Haley and Maksis[119] developed a lubrication model for droplet spreading, which includes the effect of liquid slip on solid substrates, and also relates the dynamic contact angle with the velocity of the contact line. They then applied a pseudo-spectral method to

solve the non-linear system of equations numerically, and investigated the effects of different physical parameters on the spreading rate. At roughly the same time, Hocking[120] compared the model with dynamic contact angle (chanting with advancing velocity) and the model with static contact angle (the contact angle at the rim of the drop remains equal to its static value even when the contact line is moving). The author concluded a preference to the model with static contact angle, and also described briefly the effect of gravity on the spreading rate. To examine the simulation results, Ehrhard[121] carried out experiments with completely wetting silicone oil and partial wetting paraffin oil. The results quantitatively agreed well with the simulation results by Ehrhard and Davis in 1991[115], and verified the reliability of the lubrication-type models in predicting the isothermal/non-isothermal droplet spreading.

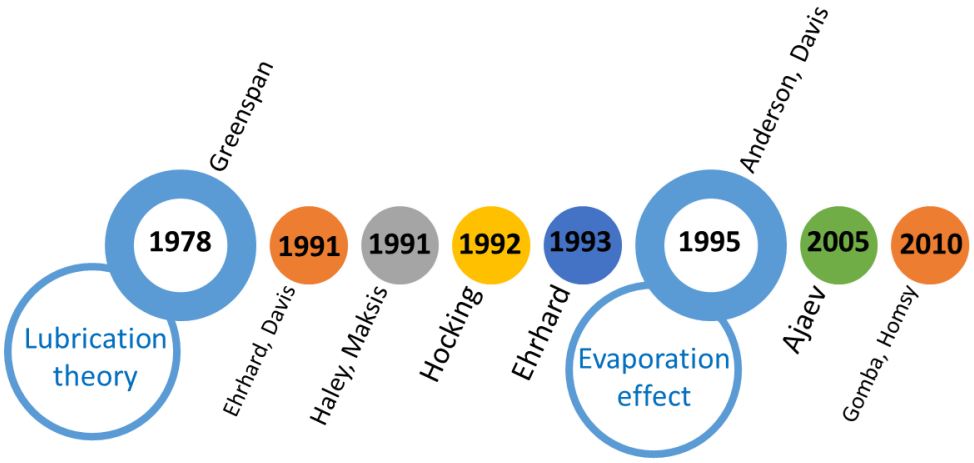

Figure 2.3 Development of lubrication-type models for droplet spreading

Figure 2.3 shows a brief history of the development of lubrication type models for droplet spreading. The basic lubrication models are developed to describe the spreading of nonvolatile droplets on solid substrate. Nevertheless, most droplets in the natural worlds are volatile. In such cases, the evaporative mass flux will decrease the droplet volume, affect the motion of triple contact line, and induce evaporative cooling at the droplet interface. In 1995, Anderson and Davis[122] took account of the effect of evaporation, and developed a one-side model to describe the dynamics of a two-dimensional volatile liquid droplet on a uniformly heated plate. They applied the expression of mass flux, ($K \cdot J = T_I - T_s$), based on a kinetic theory[123][124], which relates the

mass flux to the local interface temperature. They identified features of droplet profile as a result of competition between spreading and evaporation, and further discussed the effect of capillary number and evaporative number on the droplet dynamics. In 2005, Ajaev[125] proposed a different approach to contact line modeling based on the previous work of Moosman and Homsy[126]. Instead of applying the correlations between droplet contact angle and the contact line motion, Ajaev's model assumed a microscopic adsorbed film in the dry area on the heated surface, and that the adsorbed film is in thermodynamic equilibrium with both the vapor and solid phases. Due to van der Waals effect, the equilibrium can be achieved by non-zero film thickness, avoiding the singularity at the contact line. Gomba and Homsy[127] further developed the model which included the effect of a non-zero contact angle through a disjoining-conjoining pressure term. They predicted a capillary ridge near the leading edge for droplets with small contact angles, while for large contact angles, a fixed shape was predicted.

In recent years, the lubrication-type model has been further developed to simulate the spreading and evaporation phenomena of more complex droplets, such as droplets with nanoparticles, with soluble and insoluble surfactants, etc. Using a similar model with Ajaev, Matar et al.[128] simulated the dynamic spreading of an evaporating droplet containing nanoparticles. They accounted for the structural component of the disjoining force for film thickness exceeding the diameter of nanoparticles. The derived equations included the effect of particle concentration on the viscosity, and qualitatively simulated the experimental phenomenon of a "step" emerging from the contact line. They further developed the model to simulate more complex behaviors of droplets containing nanoparticles[129]. Depending on the value of system parameters, a variety of droplet behaviors are predicted, including spreading, evaporation-driven retraction, contact line pinning, and "terrace" formation. Karapetsas et al.[130] developed a lubrication type model for droplets with both insoluble and soluble surfactants. They accounted for the surfactant transport across the liquid-air interface, and the adsorption of surfactant on the solid surface. The simulation results indicated that the basal adsorption and sorption kinetics

play a crucial role in the spreading process, which well explains the superspreading and surfactant enhanced-spreading of liquid droplets on solid substrates. The model was further modified to simulate the dynamics of liquid lenses with surfactants over a fluid layer[131]. Maki et al.[132] applied the lubrication type model along with the assumption of precursor film to describe the spreading behaviors of droplets with colloidal suspensions. Karapetsas et al.[133] further developed the model for droplets laden with particles and insoluble surfactants. They investigated the presence of surfactant on the evaporation rate and the fluid dynamics with and without particles. The conclusions contributed to a better understanding of the deposition patterns by the interaction between particle suspensions and insoluble surfactants.

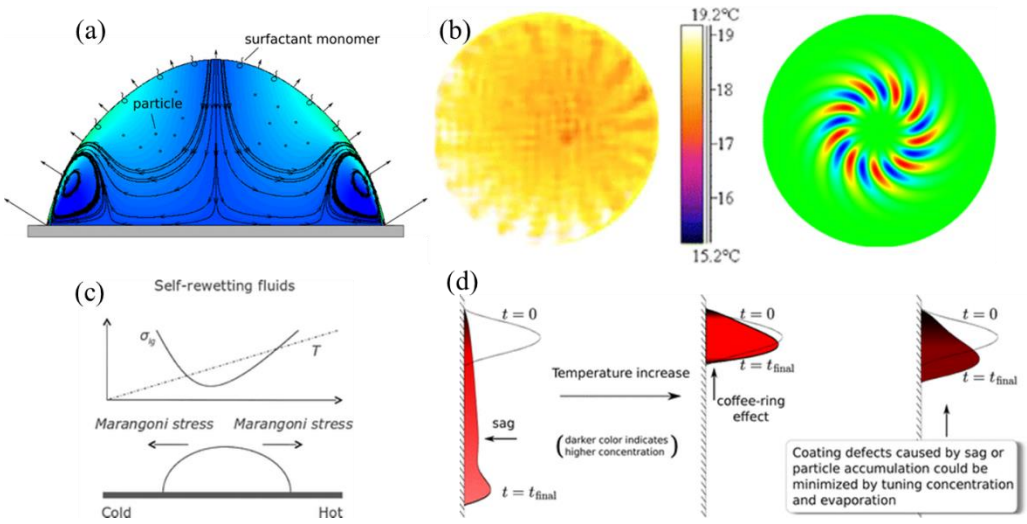

Figure 2.4 Examples of complex phenomena predicted by lubrication type models. (a) A droplet with particles and insoluble surfactants.[133] (b) Hydrothermal waves arising at the interface of volatile droplets.[16] (c) Motion of a droplet of self-rewetting fluid on a substrate with temperature gradient.[136] (d) Motion of a droplet with colloid suspensions attached to a vertical surface.[134]

Besides the development of lubrication-type models for droplets with complex components, researchers also developed models to simulate the observed interfacial phenomena during droplet evaporation, and the droplet motion under external forces. Some examples of those studies are shown in Figure 2.4. Karapetsas et al.[16] simulated the hydrothermal waves arising from temperature gradient as a result of natural

evaporation. They carried out a linear stability analysis of the flow in the quasi-steady-state approximation, and qualitatively predicted the formation of travelling hydrothermal waves reported in experimental observations[15]. Espín and Kumar[134] investigated the dynamics of evaporating droplets with colloidal suspensions on inclined substrates under the action of gravity. They developed a mathematical model based on the lubrication theory and the rapid-vertical-diffusion approximation. The results related the suspension rheology with preferential evaporation, and explained the droplet dynamics by the spatial evolution of viscosity and diffusivity along with colloidal concentration. Karapetsas et al.[135] further applied the model to simulate the droplet dynamics on an inclined, non-isothermal solid substrate, and analyzed the effects of thermocapillary and gravitational force on the contact line motion. They also investigated the dynamics of a droplet of self-rewetting fluid[136] whose surface tension depends non-monotonically on the local temperature.

2.4. Present work

Over the past decades, the phenomena of droplet evaporation have been investigated broadly and extensively. The research topics include the prediction of droplet lifetime, the capillary and convective micro flow within a droplet, the Marangoni phenomena induced by surface tension gradient, the deposition patterns of drying droplets and their relation with the interior flow, etc. The study of ionic solution droplets is a division of research on binary-component droplets, which focuses on the droplet behaviors and the crystallization deposits from drying droplets.

This thesis, on the other hand, focuses on the vapor absorption process into hygroscopic liquid desiccant droplets, especially, we focus on one type of hygroscopic ionic solution, *e.g.* LiBr-H_2O, LiCl-H_2O, etc. Up to now, research on the interaction between liquid desiccant and humid air mainly concentrates on the overall performance of different types of packed towers for practical uses. Nevertheless, the most fundamentals of the dehumidification process, *i.e.* the interaction between single liquid

desiccant droplet and humid air, have not yet been reported in existing literature. Therefore, in this thesis, we will investigate the dynamics as well as the heat and mass transfer process of single hygroscopic droplet during vapor absorption. The theoretical conclusions will be of great significance both for broadening our existing knowledge of phase change at the droplet scale, and for the design and optimization of practical dehumidification systems.

In the simulation part, a lubrication-type model is developed to simulate the droplet behaviors undergoing vapor absorption/desorption. As revealed by the literature review, in the past 40 years, the lubrication model has developed into an efficient and powerful tool to describe the droplet behaviors owning to the continuous efforts of researchers. Up to now, the lubrication-type model has been successfully applied to describe the capillary effect, the gravitational effect, the solutal and thermal Marangoni effects, as well as the particle agglomeration on the droplet dynamics. In this thesis, we will develop a lubrication-type model which combines the lubrication theory with the characteristics of hygroscopic ionic solution. The model allows for the free motion of the triple contact line by applying an assumption of precursor film in front, which will offset the vacancy of dynamic models for aqueous solution droplets, and explicitly indicate the mechanisms governing the droplet behaviors during vapor absorption and desorption.

Part II Experiments

Chapter 3 Experimental methods

3.1. Experimental devices

The behavior of desiccant droplets during vapor absorption is greatly affected by the condition of the surrounding air. In this study, experiments are conducted within an environmental chamber with accurately controlled conditions (800L, -20 °C ~ 100 °C, 20% ~ 98% *RH*, PR-3KT from ESPEC Corp.). The accuracy of environmental temperature is ± 0.5 °C, while that of relative humidity is ± 5% *RH*. Figure 3.1(a) shows the experimental setup used in this study. Six representative experimental conditions are chosen with ambient temperature of 25 °C, 45 °C, and relative humidity of 30% *RH*, 60% *RH*, and 90% *RH* (presented in Figure 3.2(a)).

During experiments, the evolution of the droplet profile is recorded with a high-definition CCD camera (Sentech STC-MC152USB with a RICOH lens and 25-mm spacing ring) at 4.8 frames per second, and an LED backlight is applied to enhance the image contrast. The recorded video of the droplet profile is then processed with MATLAB® and ImageJ® to extract the evolution of contact radius, R (mm), and contact angle, θ (deg), of the droplet with time, t (seconds). Figure 3.1(b) includes a typical snapshot of the droplet profile used to extract the droplet contact radius, contact angle, and height. Additionally, an IR camera, FLIR SC-4000 with a spectral range between 3.0 and 5.0 μm and a resolution of 18 mK, is setup vertically looking at the substrate from the top. Thermal evolution at the droplet liquid-gas interface is recorded at 2 frames per second. The influence of ambient condition on the transmissivity of the air (different ambient temperature and different *RH*) between the droplet surface and the IR camera lens is corrected depending on the experimental conditions using the ThermCam Researcher PRO 2.10 software from FLIR.

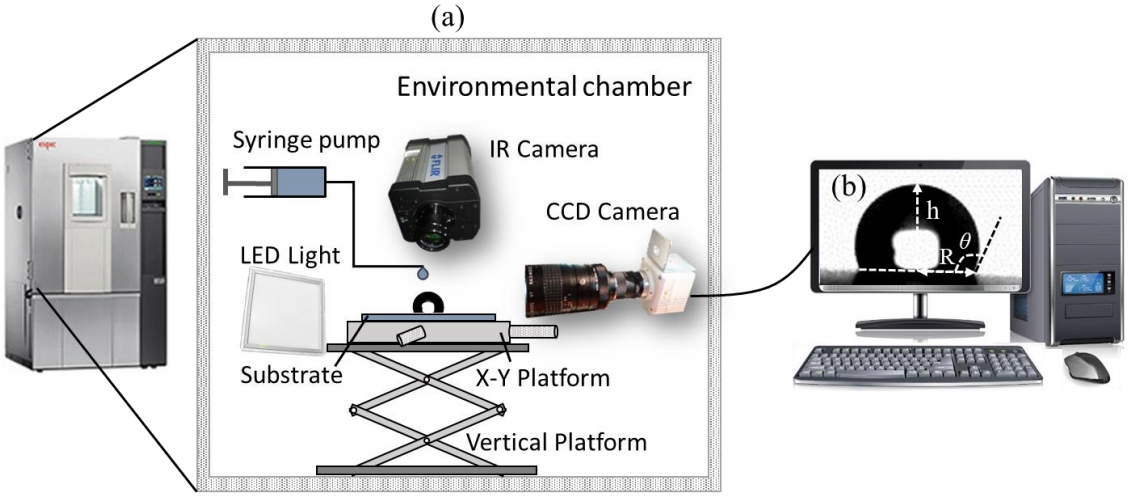

Figure 3.1 Overview of the experimental setup. (a) Experimental part: environmental chamber, CCD camera, IR camera, back light, stainless steel vertical platform, x-y platform, droplet dosing system; (b) Data acquisition system with Image J® and Matlab®.

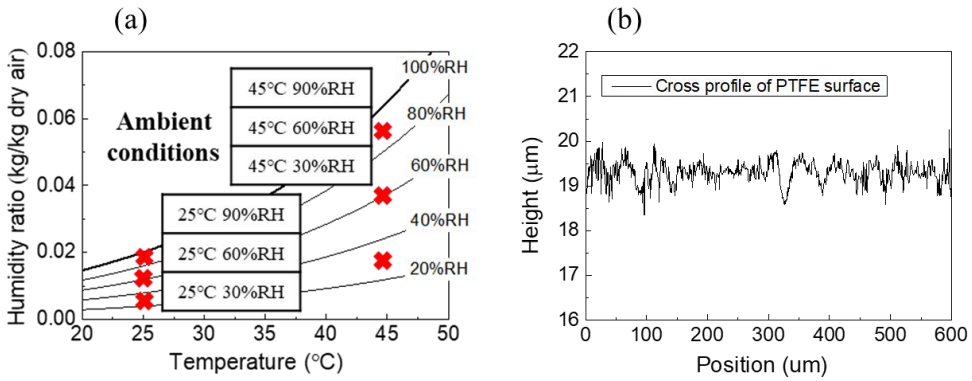

Figure 3.2 Environmental and surface conditions: (a) Experimental temperature and relative humidity shown on the psychrometric chart; (b) Cross profile of the smooth PTFE surface characterized by Olympus LEXT OLS4000.

3.2. Materials and procedures

54.0 wt.% lithium bromide (LiBr) solution and deionized water from Sigma-Aldrich are used as testing fluids for the experimental observations. Typically, a sessile droplet whose largest dimension is smaller than the capillary length will adopt spherical cap shape. For pure water in air, the capillary length is estimated as 2.6 ~ 2.7 mm (calculated according to the definition of capillary length, $\lambda = \sqrt{\gamma_{lg}/\rho g}$[68], where λ is the capillary length in meters, γ_{lg} is the liquid-air surface tension in N/m, ρ is the liquid density in

kg/m^3, g is the gravitational acceleration in m^2/s). On the other hand, for 54 wt.% LiBr-H_2O solution in air, the capillary length is *ca.* 2.42 mm. In our study, the contact radius of both water droplets and LiBr-H_2O droplets did not exceed the capillary length throughout the vapor absorption process, therefore, the gravitational effect on the droplet shape can be neglected and the assumption of treating the droplet as spherical cap is reasonable.

Table 3.1 includes the properties of 54.0 wt.% LiBr-H_2O solution and those of pure water. LiBr-H_2O solution has higher viscosity and greater liquid-gas surface tension, which contributes to the higher equilibrium contact angle of LiBr-H_2O droplets on the same substrates when compared to pure water droplets. Moreover, the boiling point of 54 wt.% LiBr-H_2O solution at 1 atmosphere is *ca.* 40 °C higher than that of pure water, which suggests the apparent lower vapor pressure at the solution surface.

Table 3.1 Properties of 54 wt.% LiBr solution and distilled water as specific heat capacity c_p (kJ/kg/K); density ρ (kg/m^3); liquid-gas surface tension γ_{lg} (mN/m); viscosity υ (mPa·s); thermal conductivity k (W/m/K); boiling temperature $T_{boiling}$ (°C). Properties shown were obtained at 20 °C and at 1 atm.[137]

Liquid type	c_p (kJ/kg/K)	ρ (kg/m^3)	γ_{lg} (mN/m)	υ (mPa·s)	k (W/m/K)	$T_{boiling}$ (°C)
54 wt. % LiBr solution	1.98	1600	91.54	4.751	0.4286	140
Distilled water	4.18	998	72.75	1.005	0.5984	100

Three type of substrates are chosen for the experiments: smooth hydrophobic polytetrafluoroethylene (PTFE), rough hydrophobic PTFE, and hydrophilic glass. Table 3.2 lists the main properties of the three substrates, where the surface roughness, S_q, is assessed with a 3D optical laser scanning microscope (Olympus LEXT OLS4000, Japan), and the droplet equilibrium contact angle for deionized water, θ_0, is measured using a custom-built contact angle analyzer at laboratory ambient conditions, *i.e.*, T_{amb} = 20 °C and 55% *RH*.

Before experiments, substrates are cleaned by immersing each sample in an ultrasonic bath with ethanol for 15 minutes. After that, the sample is taken out and rinsed

with large amount of deionized water. Then, substrates are further dried with filtered compressed air to remove any possible remaining dust or contaminants. After drying, the substrate is placed inside the chamber for sufficiently long time for the substrate to reach equilibrium temperature with the environment. Then, a droplet of 3.2 ± 0.3 microliters is deposited within the environmental chamber on the chosen substrate. We note here that dosing system and substrate are inside the chamber for sufficient time to ensure that both fluid and substrate are at T_{amb}. Before droplet deposition, CCD acquisition is started and the evolution of the droplet profile is then recorded in time.

Table 3.2 Properties of rough PTFE, smooth PTFE, and glass substrates as density ρ (kg/m^3); specific heat capacity c_p (J/kg/K); thermal conductivity k (W/m/K); thermal diffusivity α (m^2/s), $\alpha = k/\rho c_p$; surface roughness S_q (μm); and equilibrium contact angle for a 3 μL water droplet, $\theta_{0,W}$ (°), and for a 3 μL LiBr droplet, $\theta_{0,S}$ (°), at 20°C and 1 atm.

Material	ρ (kg/m^3)	c_p (kJ/kg/K)	k (W/m/K)	α (m^2/s)	S_q (μm)	Equilibrium $\theta_{0,W}$ (°)	Equilibrium $\theta_{0,S}$ (°)
Rough PTFE	2200	1.05	0.25	0.52	0.516	98° ± 3°	108° ± 3°
Smooth PTFE	2200	1.05	0.25	0.52	0.357	95° ± 3°	100 ± 3°
Glass	2400	0.84	0.75	2.15	0.012	70° ± 3°	75° ± 3°

By applying the basic experimental setup, experiments can be conducted by controlling variables. Two parts of experiments are designed. The first part of experiments aims to reveal the mechanisms of droplet growth and the effects of substrate wettability and environmental condition. We firstly focus on the behavior of LiBr-H_2O droplets for different conditions by controlling the temperature and relative humidity within the environmental chamber. Then we investigate the effects of surface wettability on the absorption rate and on the triple contact line (TCL) dynamics by comparing droplet behaviors on rough hydrophobic PTFE and hydrophilic glass substrates.

The second part of experiments aims to reveal the coupled thermal transport and mass diffusion process during vapor absorption into single droplet. IR thermography is applied to reveal the temperature distribution across the droplet interface. We firstly investigate the behaviors of LiBr-H_2O droplets for six representative environmental conditions. The

effects of absorptive heating are revealed along with the evolution of droplet interfacial temperature. We then conduct experiments with pure water droplets for same environmental and substrate conditions. A comprehensive comparison is given on the similarities and differences between droplet evaporation and vapor absorption.

3.3. Derivation of basic parameters

Figure 3.3 shows the typical profiles of sessile droplets on a solid substrate, where the R refers to the contact radius of droplet with the substrate, H refers to the height of the droplet, θ refers to the contact angle (the angle between the tangent line of droplet profile and the substrate near the triple contact line), and κ refers to the radius of curvature. The droplet profile is determined by the gravitational force ($\Delta P_{grav} = \rho g H$) and the capillary force ($\Delta P_{cap} = 2\gamma_{lg}/R$). When the capillary effect outweighs the gravitational effect, the droplet profile can be regarded as a spherical cap. For the droplet studied in this thesis, the contact radius falls below the capillary length, $\lambda = \sqrt{\gamma_{lg}/\rho g}$, therefore the capillary force dominates the formation of droplet profile. In the following analysis, the droplet profile is dealt as a spherical cap.

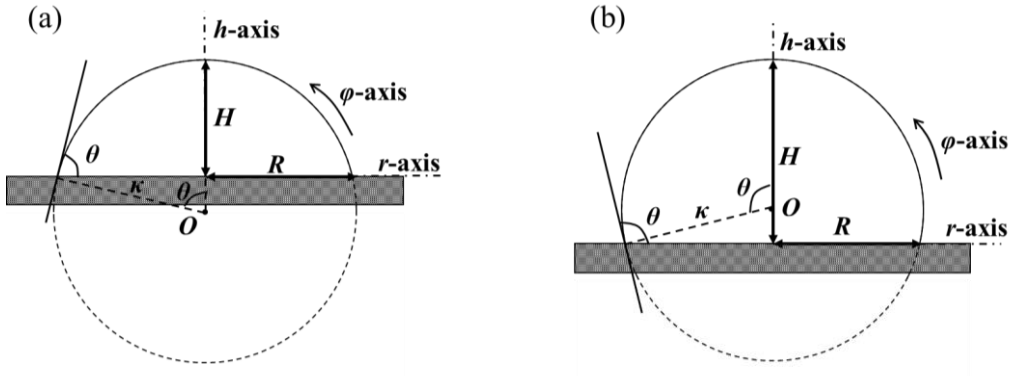

Figure 3.3 Typical profile of a droplet on (a) a hydrophilic substrate ($0 < \theta < 90°$), and on (b) a hydrophobic substrate ($90° < \theta < 180°$).

For a droplet with a shape of spherical cap, the droplet profile can be described with two basic geometrical parameters, the contact radius and the contact angle. The radius of curvature and the droplet height can be expressed as eq. (3.1) and eq. (3.2).

$$\kappa = \frac{R}{\sin\theta}, \tag{3.1}$$

$$H = R\left(\frac{1}{\sin\theta} - \frac{1}{\tan\theta}\right). \tag{3.2}$$

The surface area, *A*, and volume, *V*, of the droplet can then be derived as eq. (3.3) and (3.4).

$$A = \pi\left(R^2 + H^2\right) = \frac{2\pi R^2}{1+\cos\theta}. \tag{3.3}$$

$$V = \frac{1}{6}\pi H\left(3R^2 + H^2\right) = \frac{\pi R^3\left(1-\cos\theta\right)^2\left(2+\cos\theta\right)}{3\sin^3\theta}. \tag{3.4}$$

The height distribution along the droplet radius can be expressed as eq. (3.5).

$$h(r) = -\frac{R^2 - H^2}{2H} + \sqrt{\left(\frac{R^2 - H^2}{2H}\right)^2 - r^2} = \sqrt{\left(\frac{R}{\sin\theta}\right)^2 - r^2} - \frac{R}{\tan\theta}. \tag{3.5}$$

From the evolution of droplet volume and surface area, the rate of evaporation or vapor absorption, as well as the interfacial mass flux can be evaluated. In the case of LiBr-H_2O droplets, since the salt ions within the solution do not evaporate, we consider the variation of droplet mass is mainly due to the evaporation or absorption of water vapor. Consequently, the evolution of salt concentration along with time can be derived as eq. (3.6) according to the solute conservation equation.

$$x_{\mathrm{LiBr}}(\tau) = \frac{x_{\mathrm{LiBr},0}\rho_0 V_0}{\rho_0 V_0 + \rho_{\mathrm{w}}\left(V(\tau) - V_0\right)}. \tag{3.6}$$

The evolution of other thermophysical properties, such as the density, the thermal conductivity, the specific heat capacity, the viscosity, etc., of the LiBr-H_2O droplet can be then calculated according to the salt concentration and droplet temperature according to the property correlations of LiBr-H_2O solution in literature[137].

Chapter 4 Mechanisms of droplet growth and spreading

This chapter focuses on the vapor absorption mechanisms of LiBr-H_2O droplets on surfaces with different wettability at controlled ambient conditions[138]. Experiments are carried out with 54 wt. % aqueous lithium bromide-water (LiBr-H_2O) droplets on hydrophobic polytetrafluoroethylene (PTFE) and on hydrophilic glass substrates. The dynamics of triple contact line (TCL) and the evolution of droplet volume are compared, indicating the strong effect of surface wettability on the vapor absorption process into droplets. By looking into the solute diffusion process on the droplet side, we demonstrate the different kinetics of absorption and droplet growth, function of surface wettability. Moreover, several plausible explanations are provided to account for the apparent droplet spreading phenomenon observed on hydrophilic glass substrates when compared to hydrophobic PTFE ones.

4.1. Experimental results

4.1.1. On hydrophilic glass substrates

Representative evolution curves of contact angle, θ, and normalized contact radius, R/R_0, of LiBr-H_2O droplets for the six different ambient conditions are plotted in Figure 4.1. The initial contact angle for LiBr-H_2O droplets on a glass substrate is *ca.* 75° ± 3°, about 5° larger than that of pure water droplets due to the higher liquid-air surface tension (see Table 3.2). Depending on the ambient condition, droplets on hydrophilic glass substrates show different degree of spreading. At 30% *RH* (Figure 4.1(a)), θ decreases gradually from 75° to about 52°, while the contact radius increases to 1.24 times of its initial value. At 60% *RH* (Figure 4.1(b)) and at 90% *RH* (Figure 4.1(c)), qualitatively, the decrease in contact angle follows the same trend to that reported for 30% *RH*, where there

is a rapid initial decrease and then gradually flattens. Quantitatively, at high humidity of 90% *RH*, the contact angle decreases to about 40° while the contact radius increases to *ca.* 2 times due to greater drop spreading coupled with greater amount of water vapor absorbed. When looking into the effect of T_{amb}, at the initial stage of vapor absorption, the ambient temperature seems to influence the rate of droplet spreading where the droplet contact angle and contact radius vary more rapidly at 45°C than at 25°C.

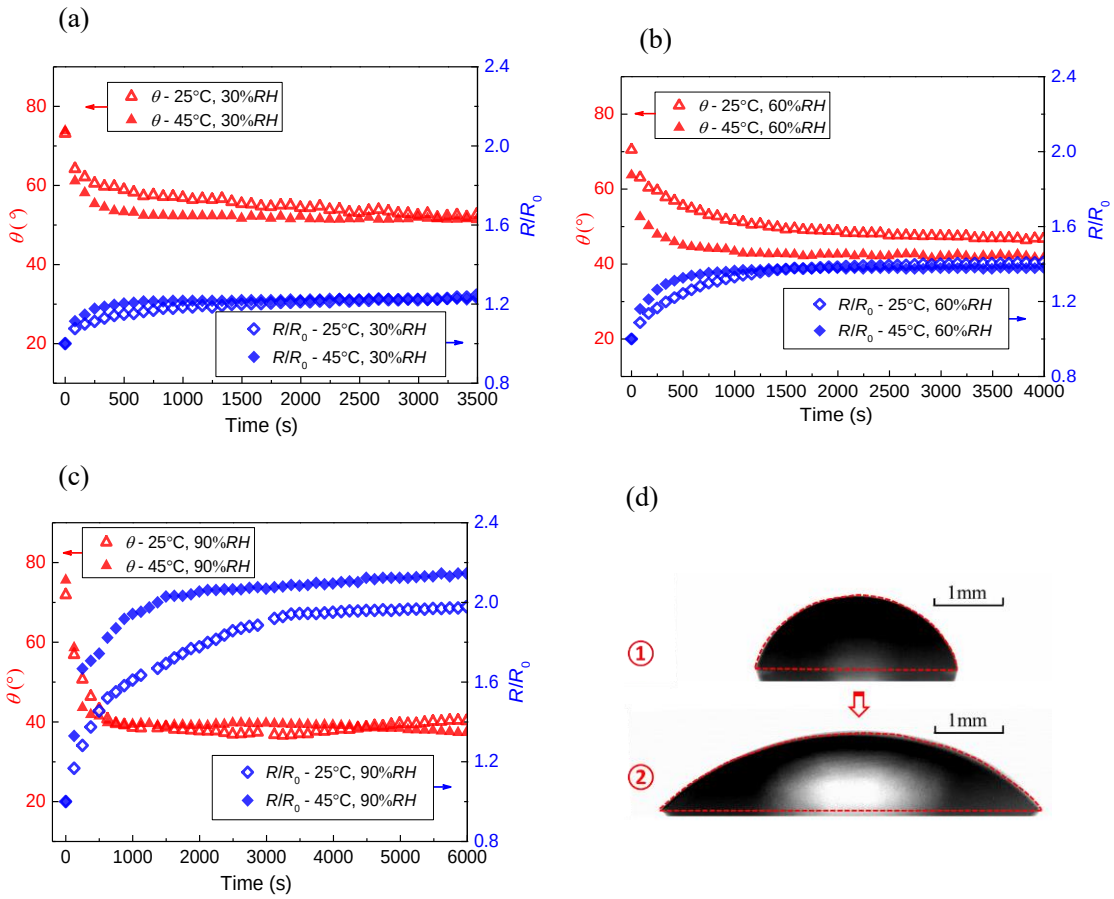

Figure 4.1 Evolution of (up-triangles) contact angle, θ (°), and (diamonds) normalized contact radius, R/R_0, of LiBr-H_2O droplets, versus time (s) for (a) 30% *RH*, (b) 60% *RH*, and (c) 90% *RH*, at (open symbols) T_{amb} = 25 °C and (close symbols) T_{amb} = 45 °C on hydrophilic glass substrates. (d) Initial (t = 0 s) and final (t = 6000 s) snapshots of a LiBr-H_2O droplet on a hydrophilic glass substrate at 45 °C and 90% *RH*.

To exemplify the droplet profile change during vapor absorption, Figure 4.1(d) shows snapshots of a LiBr-H_2O droplet on a hydrophilic glass substrate at 45 °C and 90% *RH* at the initial (t = 0 s) and at the final (t = 6000 s) stage of absorption. Due to water uptake,

an apparent expansion of droplet volume is observed. In addition, because of both droplet expansion and contact angle decrease, the triple contact line (TCL) advances greatly throughout the absorption process, *i.e.*, radius increases to approximately 1.2, 1.4 and 2.0 times its initial value at 30%, 60% and 90% *RH*, respectively.

4.1.2. On hydrophobic PTFE substrates

The evolutions of contact angle, θ, and normalized contact radius, R/R_0, on a hydrophobic PTFE substrate are shown in Figure 4.2. The initial contact angle of a LiBr-H_2O droplet on the hydrophobic PTFE substrate is *ca.* 108° ± 3° for all the experimental conditions, about 10° higher than that of pure water droplets on the same PTFE substrate studied. At 30% *RH* (Figure 4.2(a)) the contact angle of a LiBr-H_2O droplet decreases from 108° to 93° ± 4°, while the contact radius increases to *ca.* 1.2 times its initial value and reaches equilibrium after *ca.* 700 seconds. At 60% *RH* (Figure 4.2(b)) the droplet contact radius increases gradually to 1.3 times its initial value, while the droplet contact angle decreases from 108° to 93°. At 90% *RH* (Figure 4.2(c)) the droplet grows even larger as the final R/R_0 reaches *ca.* 1.6, while the contact angle decreases from 107° to 90°.

For the same ambient humidity, the increase in contact radius and the decrease in contact angle are more apparent at high ambient temperatures (T_{amb} = 45 °C) than at low ambient temperatures (T_{amb} = 25 °C). To illustrate the vapor absorption behavior, Figure 4.2(d) shows snapshots of a LiBr-H_2O droplet on a hydrophobic PTFE substrate at 45 °C and 90% *RH* at the initial (t = 0 s) and at the final stage of absorption (t = 6000 s). Comparing Figure 4.1 and Figure 4.2, it can be seen that the droplets behave differently depending on the surface wettability. The characteristic behavior of absorption for LiBr-H_2O droplets on a hydrophobic PTFE substrate can be characterized by the almost absence of TCL spreading with the increase of both droplet contact radius and droplet height solely due to the vapor absorption. Whereas for LiBr-H_2O droplets on a hydrophilic glass substrate, the coupling mechanisms of droplet spreading and water vapor absorption govern the spreading of the TCL and its dynamics.

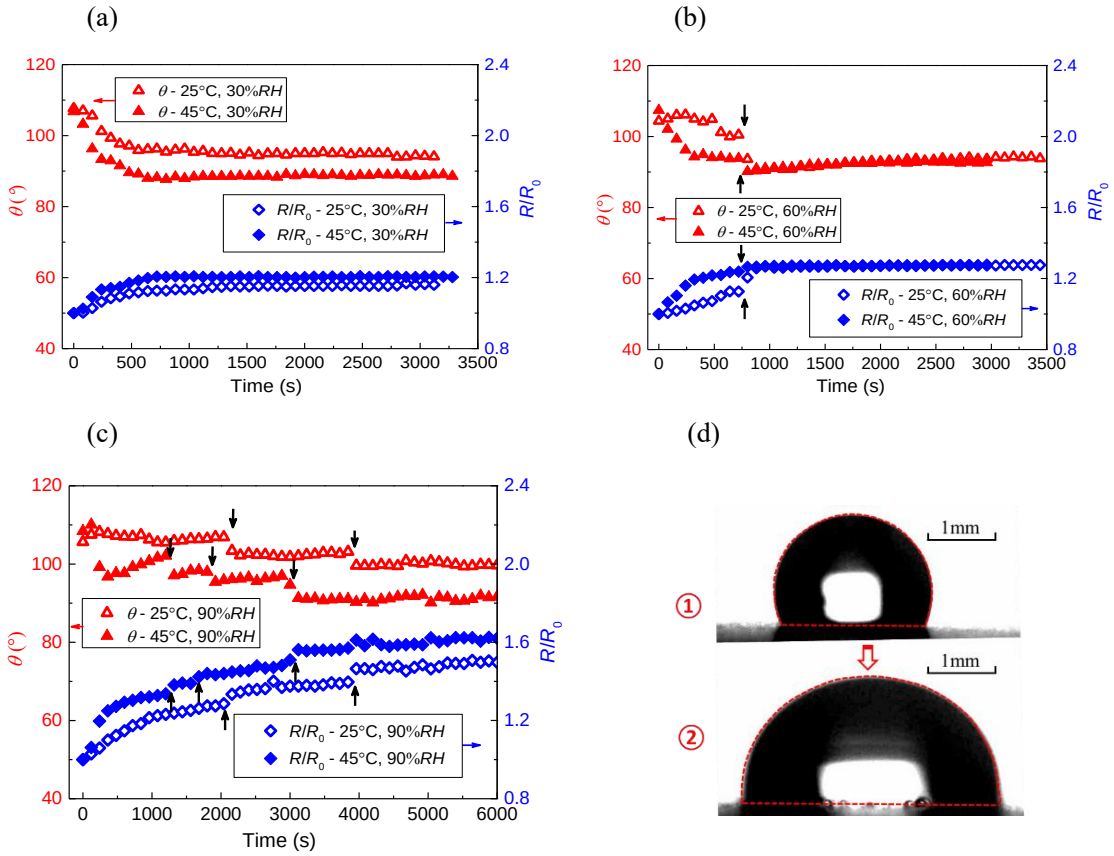

Figure 4.2 Evolution of (up-triangles) contact angle, θ, and (diamonds) normalized contact radius, R/R_0, of LiBr-H_2O droplets, versus time (s) for (a) 30% *RH*, (b) 60% *RH*, and (c) 90% *RH*, at (open symbols) T_{amb} = 25 °C and (close symbols) T_{amb} = 45 °C on a hydrophobic PTFE substrate. (d) Initial (t = 0 s) and final (t = 6000 s) snapshots of a LiBr-H_2O droplet on PTFE substrate at 45 °C and 90% *RH*.

Moreover, on a PTFE substrate we additionally report the sudden decrease in the contact angle accompanied with the increase in the contact radius, which is marked with arrows in Figure 4.2(b) and Figure 4.2(c). Such behavior converses to the stick-slip phenomena reported during evaporation of nanofluid droplets[21][92] or pure fluid droplets on structured surfaces[93]. Before stick-slip ensues, the droplet contact radius slowly increases, while the contact angle increases more apparently (Figure 4.2(c)). Then, when the contact angle reaches a certain angle, a sudden decrease in the contact angle and the associated increase in the contact radius ensues, and the TCL slips forward. In addition, the advancing stick-slip phenomenon reported here appears to be more frequent and marked at higher humidity conditions; especially at 90% *RH* (Figure 4.2(c)), due to the

more rapid droplet expansion. Advanced stick-slip phenomenon reported here is attributed to the greater surface roughness of PTFE substrate when compared to glass.

We note here that the dynamics of the TCL during vapor absorption into liquid desiccant droplets differ from those of droplet evaporation, condensation and/or from the simultaneous monotonic increase in contact angle and decrease in contact radius due to the water adsorption-absorption and/or condensation during organic solvent evaporation[139]-[141].

4.1.3. Evolution of droplet volume

During vapor absorption, the droplet volume increases in different trends depending on the ambient condition. Figure 4.3 presents evolution of the normalized droplet volume along with time on hydrophilic glass (Figure 4.3(a)) and on hydrophobic PTFE substrates (Figure 4.3(b)). At low ambient humidity of 30% *RH*, the droplet volume increases slightly, and reach equilibrium with the ambience after several hundred seconds. At 60% *RH*, droplets expand more apparently, and it also takes longer for the droplets to reach equilibrium with the ambience, *ca.*1000 ~ 2000 seconds. At high humidity of 90% *RH*, droplets keep expanding in a saturation trend throughout the two hours' observation. When comparing the final values of the droplet volume in Figure 4.3, it shows that the final expansion ratio of droplet volume, V_f/V_0, is only related to the relative humidity: V_f/V_0 (30% *RH*) ≈ 1.07, V_f/V_0 (60% *RH*) ≈ 1.5 and V_f/V_0 (90% *RH*) ≈ 2.7 ~ 3.3 regardless of surface wettability and ambient temperature. We note here that although surface wettability does not have an impact on the final droplet volume, we do on the other hand observe differences on the absorption kinetics, which will be discussed in the next Section (Section 4.2).

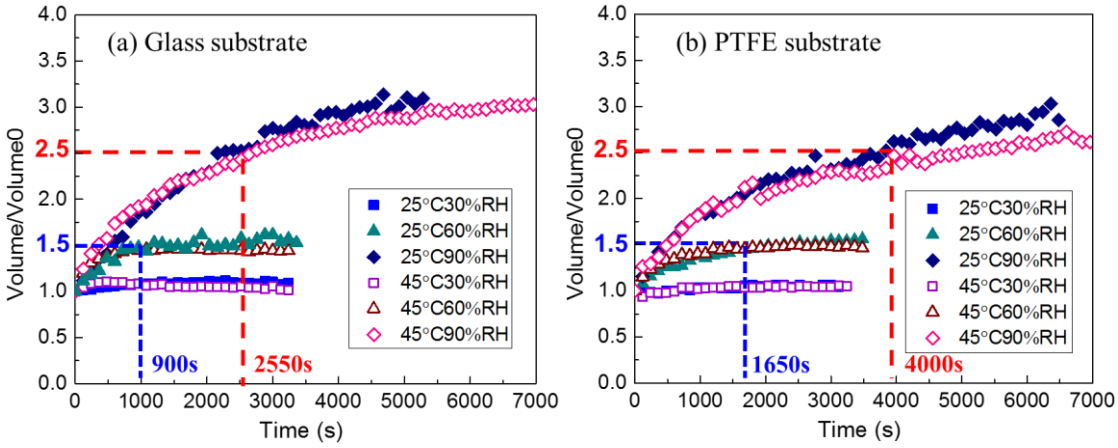

Figure 4.3 Evolution of normalized droplet volume, V/V_0, versus time, t (s), for LiBr-H_2O droplets on (a) glass substrate and (b) PTFE substrate at T_{amb} = (close symbols) 25 °C and (open symbols) 45 °C for (squares) 30%, (up-triangles) 60% and (diamonds) 90% *RH*.

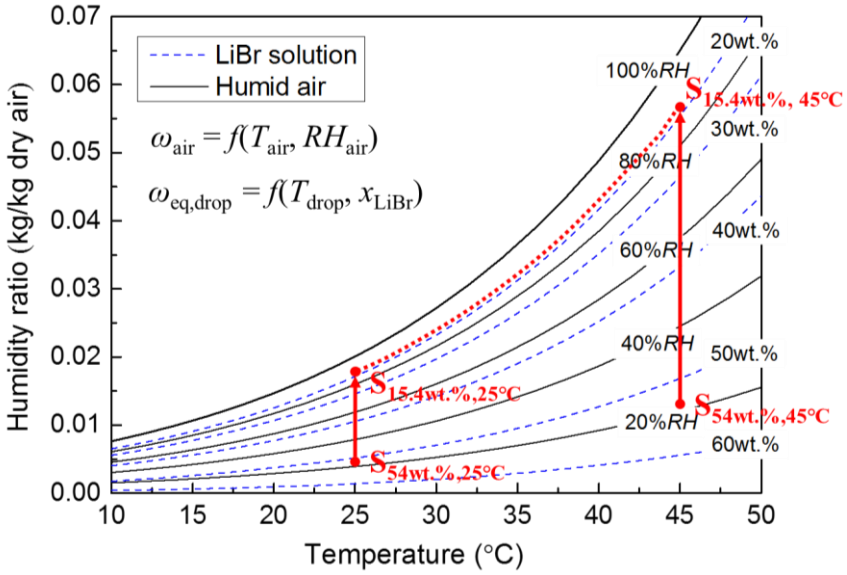

Figure 4.4 Psychrometric chart showing the state of humid air (solid line) at different relative humidity, and the state of equivalent humid air layer at the surface of LiBr-H_2O solution (blue dotted line) at different concentrations. Red solid arrows present the state variation of LiBr-H_2O solution during vapor absorption.

To demonstrate the amount of water absorbed during droplet expansion depending on T_{amb} and *RH*, Figure 4.4 includes the psychrometric chart representing the humidity ratio (kg water/ kg dry air) versus T_{amb} and *RH*. The properties of LiBr-H_2O solution and humid air in the chart are calculated with embedded functions in EES® (Engineering Equation Solver) software. Black solid lines in Figure 4.4 show the state (T_{amb} and

moisture content) of ambient air at different *RH*, while blue dash lines represent the state (T_{amb} and moisture content) of the equivalent humid air layer at the surface of LiBr-H_2O solution with different concentrations. It can be seen that the state curves of LiBr-H_2O solution and humid air are in parallel or overlap with each other, which indicates that the humid air at a certain relative humidity is in equilibrium with the solution for a certain salt concentration. When the ambient relative humidity keeps constant, the desiccant droplet will keep absorbing water vapor until it reaches equilibrium with the ambient.

The red points in Figure 4.4 represent the initial and final states ($S_{initial,25°C}$, $S_{final,25°C}$, $S_{initial,45°C}$, $S_{final,45°C}$) of the LiBr-H_2O droplets at 25 °C, 45 °C, and 90% *RH*. During vapor absorption, the liquid desiccant salts stay within the droplet in the form of ions, and therefore, the solution concentration of LiBr, *x*, should follow the solute conservation equation shown in Eq. (4.1):

$$\rho_{initial} V_{initial} x_{initial} = \rho_{final} V_{final} x_{final} . \tag{4.1}$$

For droplets at 25 °C and 45 °C, the expansion ratio of droplet volume is therefore derived as:

$$\begin{aligned} \left(\frac{V_{final}}{V_{initial}}\right)_{25°C} &= \left(\frac{x_{initial}}{x_{final}}\right)_{25°C} \left(\frac{\rho_{initial}}{\rho_{final}}\right)_{25°C}, \\ \left(\frac{V_{final}}{V_{initial}}\right)_{45°C} &= \left(\frac{x_{initial}}{x_{final}}\right)_{45°C} \left(\frac{\rho_{initial}}{\rho_{final}}\right)_{45°C}. \end{aligned} \tag{4.2}$$

Taking 90% *RH* as an example, the $\rho_{initial}/\rho_{final}$ is 1.430 at 25 °C, and 1.433 at 45 °C according to our calculation based on the correlation provided in Ref. [142]. And since the ratio of droplet concentration $x_{initial}/x_{final}$ is also the same for 25 °C and for 45 °C, the same final expansion ratio of droplet volume $V_{final}/V_{initial}$ is then demonstrated regardless of the ambient temperature and surface wettability.

4.2. Analysis and discussion

4.2.1. Effect of surface wettability

From the evolution of droplet volume, it is also worth noticing that the surface wettability has a strong effect on the kinetics of vapor absorption and on the dynamics of the TCL, which in turn dictates the mechanisms of droplet growth. As marked with red and blue dotted lines in Figure 4.3, for the same ambient condition of 45 °C and 90% *RH*, on a hydrophobic PTFE substrate it takes 4000 seconds for the LiBr-H_2O droplet to expand to 2.5 times of its initial volume, while on a hydrophilic glass substrate it takes *ca.* 2550 seconds. At 45 °C and 60% *RH*, on a hydrophobic PTFE substrate it takes 1650 seconds for the droplets to expand to 1.5 times of its initial volume, while on a hydrophilic glass substrate it takes about half of it, *i.e. ca*. 900 seconds. Clear differences on the absorption kinetics when comparing the different substrate wettability are then reported, which will be further discussed below.

Droplet growth due to vapor uptake into liquid desiccant droplets reported in this study is driven by the vapor pressure difference between the humid air and the droplet surface. The vapor absorption from the humid air into the LiBr-H_2O droplet can be divided into three steps: the water vapor diffusion on the air side, the vapor to water phase-change transition at the air-liquid interface, and the diffusion of the water molecules from the droplet interface toward the droplet bulk (or the solute (Li^+, Br^-) diffusion from the bulk of the droplet towards the droplet interface). Figure 4.5 shows one-dimensional evolution of ambient air and liquid desiccant solution during the vapor absorption process, where the thickness of the liquid layer for the diffusion of the solute equals the droplet characteristic length (h^*), and the air layer is assumed to be infinite since the chamber is large enough compared to the size of the droplets. At the very initial state, right after the droplet deposition (t = 0 seconds), we assume that there is no mass diffusion between the humid air and the aqueous solution, and an apparent vapor pressure difference between the ambient air and the liquid surface is present. Then, driven by the pressure difference, water vapor gradually diffuses from the air side to the liquid-air interface, and gets

absorbed. Due to vapor absorption, the concentration of solute (Li^+ and Br^- ions) near the liquid-air interface decreases. Then, Li^+ and Br^- ions diffuse from the high concentration side at the droplet bulk to the low concentration side at the liquid interface following the concentration gradient. As the absorption process continues and as a consequence of the increase in water concentration within the droplet, the vapor pressure difference between the liquid surface and the ambient air decreases, and at the same time, the concentration gradient of LiBr solute within the aqueous solution also decreases until equilibrium is attained.

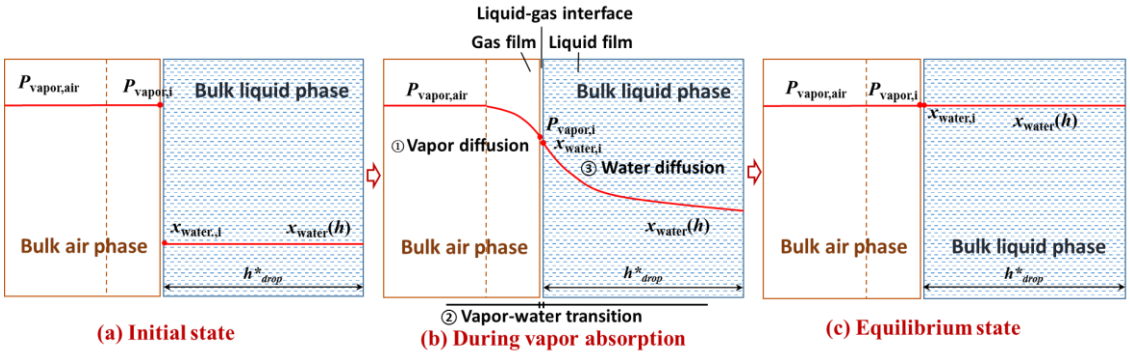

Figure 4.5 Schematic of water vapor concentration in the air side and the concentration of liquid water in the bulk of the droplet (a) at initial stage right after droplet deposition, $t = 0$ s, (b) during vapor absorption, and (c) at equilibrium, $t = \infty$.

Since vapor absorption is a surface area related problem, it is noteworthy providing a comparison between the spherical cap surface area of liquid desiccant droplets on hydrophilic *versus* hydrophobic substrates. For droplets on hydrophilic glass substrate, the interfacial area for mass transfer is *ca.* 9.02~10.65 mm^2, while for droplets on hydrophobic PTFE, the interfacial area is *ca.* 9.04~10.68 mm^2. Since there is no large difference in the effective droplet areas for vapor absorption, the absorption rate must be governed by the mass diffusion process on the air side and/or on the liquid side. Typically, the mass diffusion rate in the gas phase is $10^3 \sim 10^4$ times of that in the liquid phase ($D_{water/air}/D_{LiBr/LiBr-H_2O} \sim 10^{-5}/10^{-9} \sim 10^4$)[143]. Therefore, we can assume that the vapor absorption process is limited by the solute diffusion on the liquid side. The solute diffusion process within the LiBr-H_2O droplet can be evaluated by the characteristic time, τ, which is calculated according to Eq. (4.3),

$$\tau = L^2/D \tag{4.3}$$

where L is the characteristic length for mass diffusion, which we assume as the characteristic length of the droplet, h^*, and D is the mass diffusion rate (m^2/s).

According to eq. (4.3), the characteristic time for the solute diffusion on the liquid side can be calculated as ca. 10^3 seconds, where the characteristic length of the droplet, L, is estimated as 1 mm, and the water diffusion rate, D_s, is 10^{-9} m^2/s[144][145]. Calculation shows that the characteristic time for solute diffusion is in the same order of magnitude to that of the vapor absorption period reported in the experiments (500 ~ 8000 seconds). Hence, we report that the solute concentration gradient within the LiBr-H_2O droplet is the limiting mechanism governing vapor absorption into liquid desiccant droplets and it cannot be neglected.

More specifically, the characteristic length for solute diffusion within the droplet should be the shortest path for the diffusing molecules to "touch" the impermeable wall, *i.e.*, the solid surface, or to "meet" each other. On hydrophilic glass substrates where the droplet contact angle is less than 90°, the characteristic length is the droplet height $h^* = h_{drop}$ as marked in Figure 4.6(a), whereas on hydrophobic PTFE substrates where the droplet contact angle is larger than 90°, the characteristic length is assumed as the radius of curvature $h^* = \kappa_{drop}$ as marked in Figure 4.6(b).

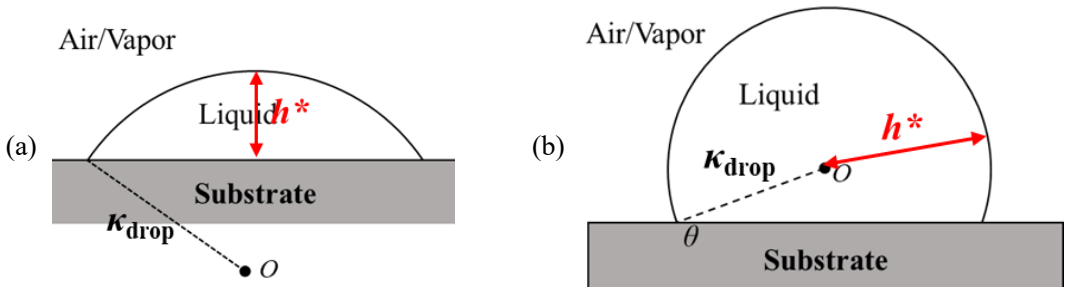

Figure 4.6 Characteristic droplet length, h^*, for solute diffusion within the LiBr-H_2O droplets (a) on hydrophilic glass substrate, and (b) on hydrophobic PTFE substrates.

Figure 4.7 shows the evolution of the characteristic lengths for droplets on a hydrophilic glass substrate and on a hydrophobic PTFE substrate along with vapor absorption at 45 °C and 60% *RH* (Figure 4.7(a)) and at 45 °C and 90% *RH* (Figure 4.7(b)).

It shows that, on glass substrates the characteristic length (droplet height) decreases slightly along with time at 60% *RH* due to the observed spreading, while at 90% *RH* the characteristic length increases slightly due to the absorbed water vapor. By comparison, on PTFE substrates the characteristic length (radius of curvature) increases much more apparently along with time. At 60% *RH* the characteristic length increases from about 1.18 mm to about 1.4 mm in 3500 seconds, while at 90% *RH*, the characteristic length increases from about 1.1 mm to about 1.7 mm in 7000 seconds.

The characteristic time τ for mass diffusion, defined in Equation 4.3, accounts for how long it takes for the water molecules to diffuse over the distance h^*, hence as h^* increases so does τ, and droplet saturation is reached later on the hydrophobic case. At 45 °C and 60% *RH*, for the same diffusion coefficient, $\tau_{\mathrm{PTFE}}/\tau_{\mathrm{glass}} \sim h^*_{PTFE}/h^*_{glass} \sim 1.96$. This estimation remarkably agrees with the experimental results where it takes 1650 seconds and 900 seconds for the droplets to reach equilibrium on PTFE substrate and on glass substrate respectively, *i.e.*, $\tau_{\mathrm{PTFE}} / \tau_{\mathrm{glass}} = 1650 / 900 \sim 1.83$.

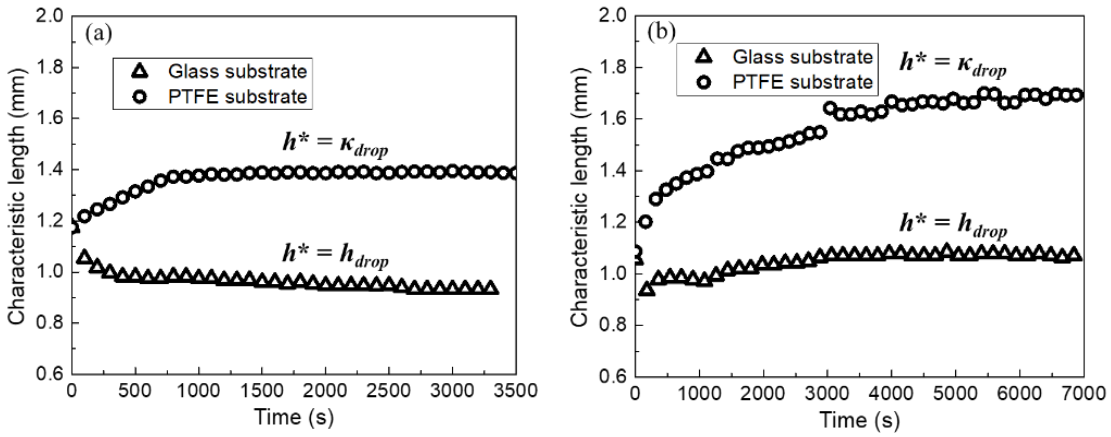

Figure 4.7 Evolution of characteristic lengths for solute diffusion within the LiBr-H_2O droplets, versus time (s), on (triangles) hydrophilic glass substrates and on (circles) hydrophobic PTFE at (a) 45 °C and 60% *RH*, and at (b) 45 °C and 90% *RH*.

The above analysis clearly demonstrates that surface wettability has a strong impact on the vapor absorption kinetics, on the dynamics of the TCL and on the mechanisms of droplet growth. In industrial applications, when the total contact time between liquid desiccant and humid air is limited, we propose that hydrophilic inner packing as the

optimum configuration to further enhance the dehumidification capacity of dehumidifiers.

4.2.2. Mechanisms of droplet spreading

As described in Section 4.1, on hydrophilic glass substrates LiBr-H_2O droplets show an apparent spreading trend with monotonously increasing contact radius and decreasing contact angle (Figure 4.1), while on hydrophobic PTFE substrates no apparent additional spreading is observed (Figure 4.2). In previous literature, droplet spreading phenomenon is reported in the droplet deposition process[146]. In those studies, the droplet spreading is due to competition between capillary driving forces and viscous dissipation, and takes place very fast following Tanner's law[116]: $R(t) \propto t^{1/10}$. The time scale of spreading is ~1 ms for low viscosity liquids such as water in air on boro-silicate glass substrates[146]. However, in our work LiBr-H_2O droplets spread along with a time scale *ca.* 10^2~10^3 s greater than for early regimes of spreading. Therefore, classical droplet spreading described by Tanner's law cannot be used to explain the spreading of the TCL observed during vapor absorption on a hydrophilic substrate.

Next, to elucidate the different spreading behavior depending on the substrate wettability reported in our study, we look into the different binary interactions at the TCL. Figure 4.8 presents schematic of the droplet profile at equilibrium contact angle, θ_0, and at slightly larger contact angle, $\theta_0+\delta\theta$, due to vapor absorption on (a) hydrophilic glass and (b) on hydrophobic PTFE substrates. At the equilibrium state, the profile of a droplet on a smooth ideal surface follows the balanced Young's equation, $\gamma_{SG} - \gamma_{SL} = \gamma_{LG}\cos\theta_0$, which accounts for the respective binary surface tensions: solid-gas, γ_{SG}, solid-liquid, γ_{SL}, and liquid-gas, γ_{LG}[147]. As conveyed above, after the deposition of a desiccant droplet on a substrate in the presence of a humid environment, the droplet volume will increase due to vapor absorption. Within a finite short time, δt, and assuming the droplet contact line as pinned, the contact angle will increase due to volume expansion to ($\theta_0+\delta\theta$). Moreover, since the solution near the droplet surface gets diluted due to water absorption, the liquid-gas surface tension γ_{LG} will increase by $\delta\gamma_{LG}$. Because of the variations in both the contact angle and the liquid-gas surface tension, the force balance at the TCL is altered, and as a

consequence an extra horizontal force, δF, arises which tends to depin the contact line. By neglecting the second order small quantity, δF can be derived as Eq. (4.4):

$$\delta F = \left(\gamma_{LG} + \delta\gamma_{LG}\right)\cos\left(\theta_0 + \delta\theta\right) - \gamma_{LG}\cos\theta_0 \approx -\gamma_{LG}\sin\theta_0\delta\theta - \left|\delta\gamma_{LG}\right|\cos\theta_0 \qquad (4.4)$$

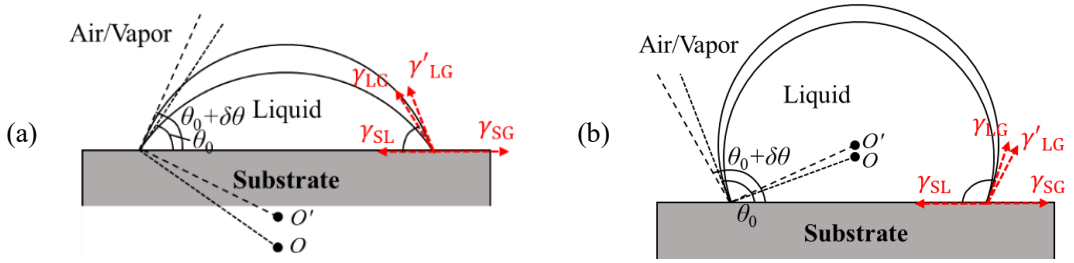

Figure 4.8 Schematic of droplet profiles at the equilibrium state and at a slightly different contact angle ($\theta_0 \rightarrow \theta_0+\delta\theta$) due to vapor absorption on (a) hydrophilic glass substrate and on (b) hydrophobic PTFE substrate.

On hydrophilic substrates, the droplet contact angle is smaller than 90°, and the value of $\cos\theta_0$ is positive. In this case, the absolute value of the depinning force can be expressed as $\left|\delta F\right|_{\theta<90^\circ} = \left|\gamma_{LG}\sin\theta_0\delta\theta\right| + \left|\delta\gamma_{LG}\cos\theta_0\right|$. While on hydrophobic substrates, the contact angle is larger than 90°, and the absolute value of the depinning force can be then expressed as $\left|\delta F\right|_{\theta>90^\circ} = \left|\gamma_{LG}\sin\theta_0\delta\theta\right| - \left|\delta\gamma_{LG}\cos\theta_0\right|$. Therefore, for the same change in the contact angle, the depinning force is larger on hydrophilic substrates than on hydrophobic ones: $\left|\delta F\right|_{\theta<90^\circ} > \left|\delta F\right|_{\theta>90^\circ}$. Then, for an identical intrinsic energy barrier, $\partial U/\partial r$, it is easier for the TCL to advance on hydrophilic glass substrates.

Figure 4.9 shows the evolution of liquid-air surface tension, γ_{LG}, along with vapor absorption for the six experimental conditions studied by assuming the solute distribution within the droplet as homogenous[148]. Depending on the experimental condition investigated, γ_{LG} of LiBr-H_2O droplet decreases as water vapor is absorbed. In addition, as for common fluids, at higher temperature, LiBr-H_2O droplets have smaller surface tension than at low temperatures. Moreover, as absorption takes place, the surface tension decreases with time more apparently at higher ambient humidity conditions as shown in Figure 10. In the extreme case of 45°C and 90% RH, the surface tension decreases from

ca. 88.04 mN/m to ca. 74.78 mN/m, which is still larger than that of pure water droplet at 45°C ($\gamma_{LG,water,45°C} \approx 69.14$mN/m[149], which can be considered as 0 wt.% LiBr-H_2O solution). The decrease in the droplet surface tension partly accounts for the contact angle decrease during vapor absorption. Nevertheless, the decrease in contact angle during vapor absorption is about 30°, which cannot be accounted for by the contact angle change caused purely by surface tension decrease. Therefore, additional explanations are expected.

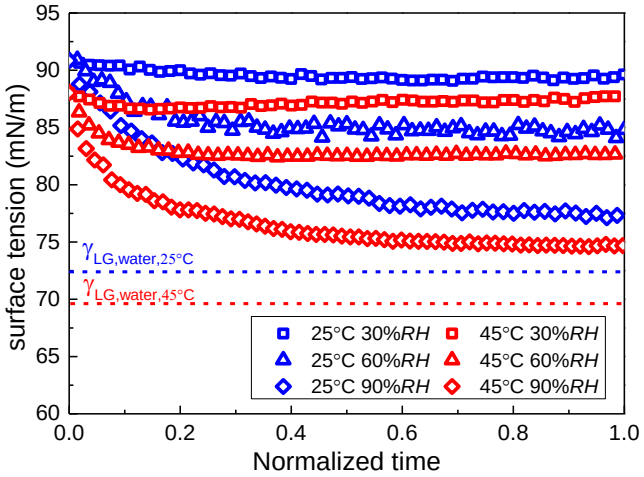

Figure 4.9 Evolution of surface tension of LiBr-H_2O droplets along with time during vapor absorption on a hydrophilic glass substrate.

Compared to hydrophobic PTFE substrates, the hydrophilic nature of glass substrates induces higher adhesion force to water molecules[150].Therefore, in humid environments, water molecules may accumulate near the glass surface due to adsorption[151]. In the presence of a LiBr-H_2O droplet, the surface near the contact line will absorb more water vapor and induce both density gradient and surface tension gradient along the droplet interface. In previous literature, droplet spreading has been reported due to surface tension gradient created by localized surfactant addition[152], as well as by temperature gradient[153]. Therefore, the density gradient and surface tension gradient induced by non-uniform absorption across the droplet surface can be another plausible reason for the droplet spreading observed in this study.

Furthermore, when looking into a moving contact line, a precursor film is usually considered to be ahead of the visible droplet bulk[154][155]. In previous studies, the existence of precursor film has been verified by advanced experimental techniques such as atomic force microscopy (AFM)[156], and epifluorescence inverted microscopy[157], amongst others[158]. Figure 4.10 shows the proposed schematic of the continuous transition from the macroscopic droplet profile to the microscopic precursor film at the triple contact line for a spreading droplet on a hydrophilic substrate. The length of the diffusive precursor film is proportional to the square root of time and can be expressed as Eq. (4.5)[157].

$$L_p = \sqrt{\frac{A}{3\pi\eta h_c}} t^{1/2} \tag{4.5}$$

where L_p is the length of the precursor film, A is the effective Hamaker constant, η is viscosity, h_c is the cutoff thickness, and t is time.

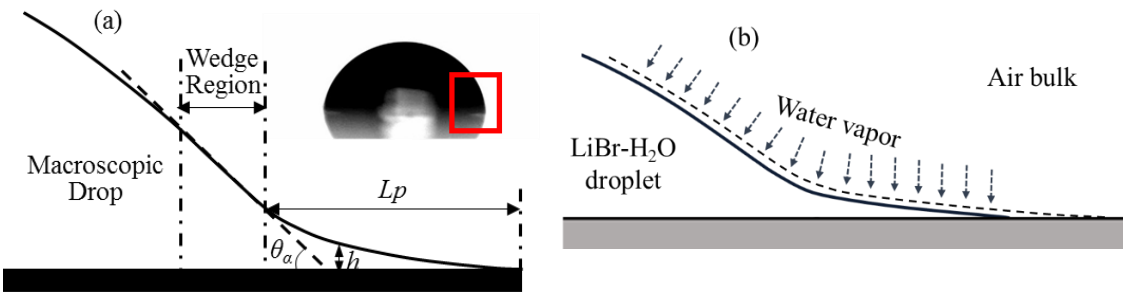

Figure 4.10 Schematic of (a) microscopic features in the vicinity of the advancing contact line along with microscopic droplet profile on a hydrophilic substrate, and (b) absorption near the triple contact line.

For droplets on a hydrophobic PTFE substrate, due to the larger droplet curvature, the cutoff thickness is larger than that of droplets on hydrophilic glass[159]. According to Eq. (4.5), the length of the precursor film is inversely proportional to the square root of the cutoff thickness, hence the length of precursor film will be longer on a hydrophilic glass substrate than on a PTFE hydrophobic one. During experiments, vapor absorption happens both at the macroscopic droplet interface and at the precursor film. As vapor absorption proceeds, the precursor film will gradually grow thicker, with the inner side

merging with the droplet bulk, and the outer side stretching forward. Since the precursor film typically extends more on hydrophilic substrates than that on hydrophobic ones, the precursor film develops more rapidly, and the triple contact line thus advances further, which is put forward as an additional mechanism for the greater droplet spreading observed on hydrophilic substrates.

4.3. Summary

This chapter investigates the effect of substrate wettability and ambient conditions on the vapor absorption process. Typically, on hydrophilic glass substrates, LiBr-H_2O droplets show an apparent spreading trend during vapor absorption. While on hydrophobic PTFE substrates, a less decrease in the contact angle along with an increase in the contact radius, *i.e.*, less spreading, is observed. Moreover, the final expansion ratio of droplet volume is only function of relative humidity regardless of environmental temperature and surface wettability.

Depending on the surface wettability, the kinetics of vapor absorption are found to differ. On hydrophilic glass substrates, LiBr-H_2O droplets reach equilibrium with the ambient much quicker when compared to hydrophobic PTFE substrates. This is attributed to the shorter characteristic length for solute diffusion, which is further demonstrated by evaluating the characteristic time for solute diffusion within the droplet. Besides, the apparent droplet spreading on hydrophilic glass substrates is explained based on a force balance analysis at the triple contact line, by the evolution of liquid-gas surface tension, and by the development of a precursor film during vapor absorption. Further explorations with the spreading phenomena are carried out by numerical simulations, which will be elucidated in consequent chapters.

Chapter 5 Coupled heat transport and mass diffusion

This chapter focuses on heat and mass transport coupling mechanisms during vapor absorption into lithium bromide desiccant (LiBr-H_2O) droplets for controlled environmental conditions[160]. The evolution of droplet profile and the temperature distribution at the droplet surface are investigated using optical imaging and infrared (IR) thermography. We reveal the temperature variation across the surface of hygroscopic droplets along with time, and analyze the interactions between the droplet and the substrate and surrounding air. We then discuss the effect of absorptive heating on the mass transfer process, and relate the variation of vapor absorption rate with the evolution of vapor pressure difference between the droplet liquid-air interface and the ambient. Furthermore, we compare and summarize the similarities and differences between the vapor absorption process into liquid desiccant droplets and the evaporation process of pure water droplets.

5.1. Experimental results

5.1.1. Evolution of droplet profile

Figure 5.1 shows typical profile evolution of LiBr-H_2O droplets at 45°C and humidity of 30%*RH*, 60%*RH*, 90%*RH*. Figure 5.2 represents the variation of the contact angle, θ (deg), and the non-dimensional contact radius, R/R_0, of LiBr-H_2O droplets versus non-dimensional time (normalized by the experimental duration), τ. On a smooth PTFE substrate, the initial contact angle of LiBr-H_2O droplet is *ca.* 101°±3°. As vapor absorbs into the droplet, an expansion in volume is recorded especially when the ambient humidity is high. The droplet expansion is demonstrated by the simultaneous increase in droplet height and contact radius, while the droplet contact angle remains almost constant

throughout the entire experimental duration.

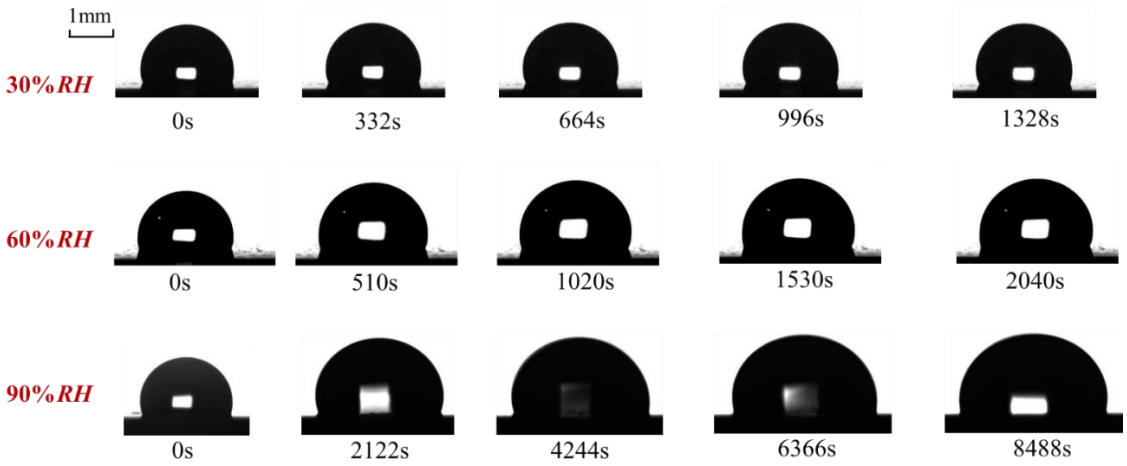

Figure 5.1 Profile evolution of LiBr-H_2O droplets during vapor absorption for ambient condition of 45°C and 30% *RH*, 60% *RH*, 90% *RH*, for τ = 0, 0.25, 0.5, 0.75 and 1.

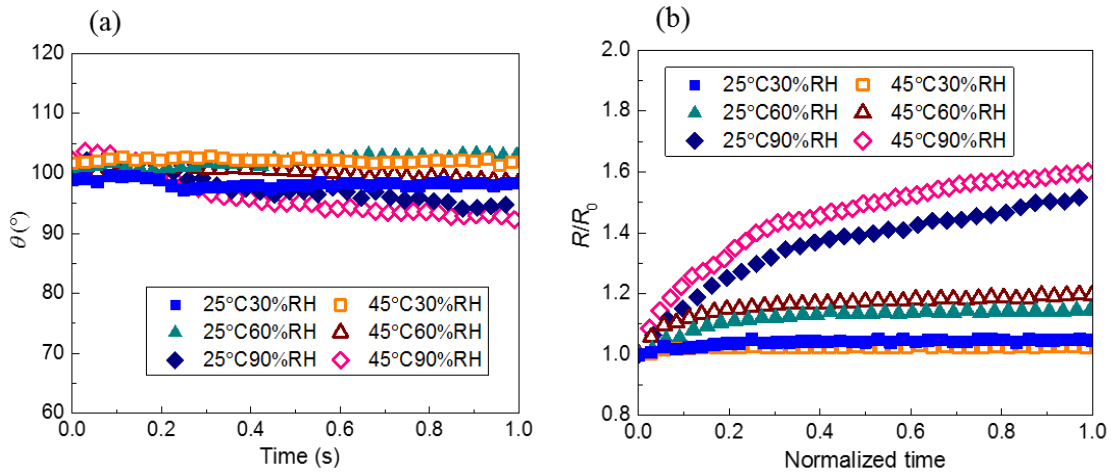

Figure 5.2 Evolution of (a) contact angle θ (deg), and (b) non-dimensional contact radius R/R_0, of LiBr-H_2O droplets, versus non-dimensional time, τ, for (closed symbols) T_{amb} = 25 °C and (open symbols) T_{amb} = 45 °C at (square) 30% *RH*, (up-triangles) 60% *RH*, and (diamonds) 90% *RH* on smooth PTFE.

At high humidity conditions of 90% *RH*, the contact angle decreases by *ca.* 5°, which is attributed to the decreasing liquid-air surface tension as the desiccant solution gets diluted due to water uptake. On the other hand, the contact radius increases depending on the ambient humidity. When the ambient humidity is low, *e.g.* 30% *RH*, the contact radius increases slightly to about 1.03~1.05 times of its initial value after 10 minutes. At ambient humidity of 60% *RH*, the contact radius increases more significantly to 1.14~1.20 times

of its initial value after 30 minutes. At higher ambient humidity of 90% *RH*, the contact radius of LiBr-H_2O droplet keeps increasing to about 1.6 times of its initial value.

For an easier comparison, Figure 5.3 and Figure 5.4 include the behavior of pure water droplets during evaporation on the same substrate for the same six experimental conditions. The initial contact angle of pure water droplet is 95°±5°, lower than that of LiBr-H_2O droplet, which is attributed to the lower liquid-air surface tension, 72.75 mN/m, compared to 54 wt.% LiBr-H_2O solution (91.54 mN/m). Pure water droplets firstly evaporate following the constant contact radius (CCR) mode, where R/R_0 remains almost constant and θ decreases along with time to account for the loss of volume for the first 20% of the droplet lifetime. Thereafter, as the contact angle decreases to approximately 86°±3°, the contact line starts receding and droplets evaporate in the constant contact angle (CCA) mode, where θ remains almost constant, and R/R_0 monotonically decreases. The CCA mode lasts for approximately 60% of the overall droplet lifetime. Lastly, as the droplet becomes smaller, towards the end of the evaporation process, droplet evaporation turns into a mixed mode where both θ and R/R_0 decrease, which takes approximately the remaining 20% droplet lifetime. The three distinctive regimes reported here, *i.e.*, CCR, then CCA and lastly the mixed mode, are in agreement with previous studies[28][161][162] on water droplets evaporating on smooth PTFE substrates.

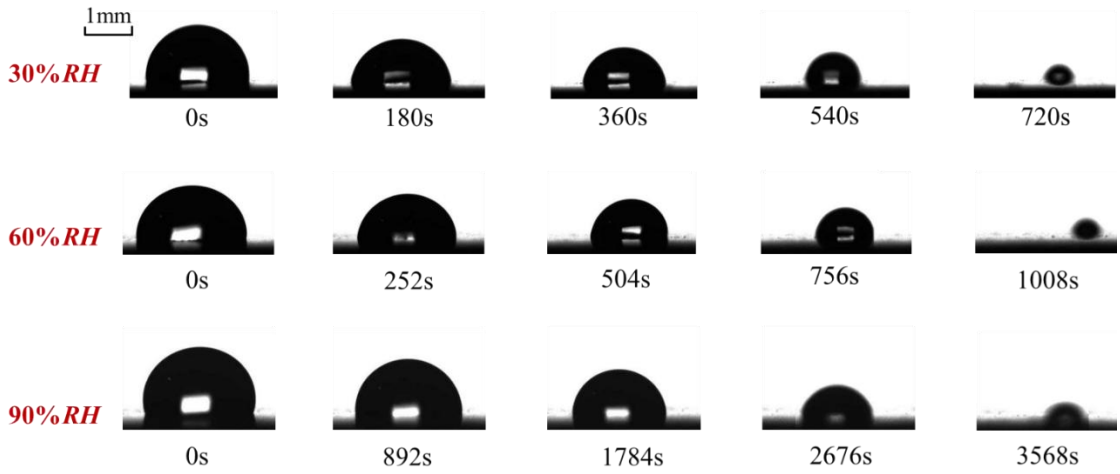

Figure 5.3 Profile evolution of pure water droplets during evaporation for ambient condition of 45°C and 30% *RH*, 60% *RH*, 90% *RH*, for τ = 0, 0.25, 0.5, 0.75 and 1.

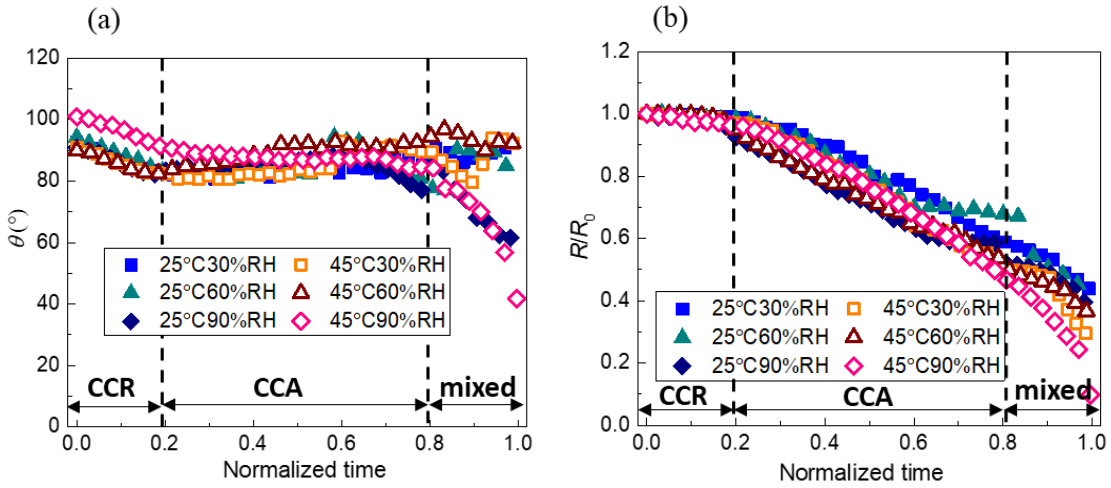

Figure 5.4 Evolution of (a) contact angle θ, and (b) non-dimensional contact radius R/R_0 of pure water droplets, versus non-dimensional time, τ (s) for (closed symbols) T_{amb} = 25 °C and (open symbols) T_{amb} = 45 °C at (square) 30% *RH*, (up-triangles) 60% *RH*, and (diamonds) 90% *RH* on smooth PTFE.

5.1.2. Evolution of droplet volume

Figure 5.5 presents the volume evolution of LiBr-H_2O droplets during vapor absorption and that of pure water droplets during evaporation. Moreover, the initial rates of vapor absorption and evaporation for the six experimental conditions are included in Table 5.1.

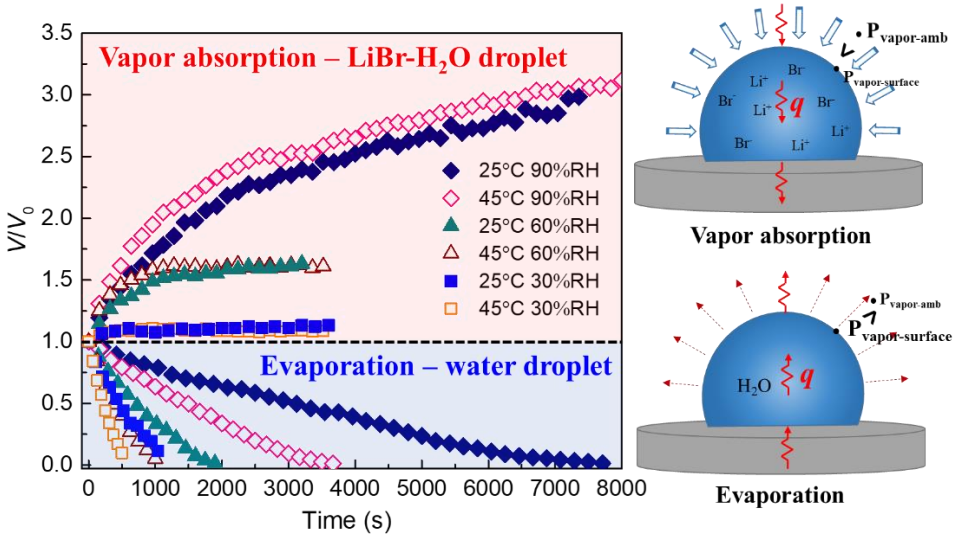

Figure 5.5 Evolution of non-dimensional droplet volume with respect to the original volume, V/V_0, along with time, t (s), during vapor absorption and evaporation for the six environmental conditions.

Table 5.1 Initial evaporation rate, -d*V*/d*t*, and initial vapor absorption rate, d*V*/d*t*, for the six experimental conditions. (At 30% *RH*, the vapor absorption is quite weak, thus calculations are only carried out with 60% *RH* and 90% *RH* conditions.)

Condition	25°C 30%*RH*	25°C 60%*RH*	25°C 90%*RH*	45°C 30%*RH*	45°C 60%*RH*	45°C 90%*RH*
Absorption rate *dV/dt* (nL/s)	-	3.44	5.00	-	5.96	6.97
Evaporation rate *-dV/dt* (nL/s)	4.25	3.02	0.83	9.42	5.40	1.27

5.2. Analysis and discussion

5.2.1. Heat transfer analysis

Within the droplet, both heat convection and heat conduction may occur, which can be evaluated by the Péclet number expressed as Eq. (5.1).

$$Pe=\rho c_p UR/k, \tag{5.1}$$

where R is the droplet contact radius, ρ is the density, c_p is the heat capacity, U is the radial flow velocity within the droplet, and k is the thermal conductivity of the liquid studied. For evaporation of water droplets with contact angles *ca.* 90°, the evaporative mass flux can be regarded as uniform across the droplet interface [28][163][164]. In this case, the radial flow velocity, U, is rather low in the order of 10^{-7} m/s. In the case of liquid-desiccant droplets where the water vapor diffuses towards the droplet interface, homogeneous absorption flux is expected for contact angles *ca*. 90°. Hence, the concentration gradient along the droplet surface is rather small, and the concentration-induced Marangoni effect can therefore be neglected. Moreover, the IR images measured at the liquid-gas interface also show the homogeneity of the temperature profile and the absence of thermal gradients (Figure 5.6(a) & Figure 5.6(b)). In view of the above, we can then safely state that the radial flow velocity, U, remains small and is not further enhanced by the presence of Marangoni flows. Then, the *Pe* number is estimated as << 1 [17], confirming that the convective heat transfer within the droplet is negligible[79][80][165].

The heat conduction process within the droplet can be further evaluated by the

characteristic time, τ^*, given by Eq. (5.2).

$$\tau^* = \rho c_p h^2 / k, \tag{5.2}$$

where h is the droplet height. Taking into account the thermal properties of the LiBr-H_2O droplets and water droplets reported in Table 3.1, τ^*_{LiBr} is calculated as 10.51 s, and τ^*_{Water} is *ca.* 9.91 s. Right after the deposition of a liquid desiccant droplet, a temperature profile within the droplet may develop during the first instants of the vapor absorption process. However, compared to the overall droplet lifetime (~10^3 seconds), the characteristic time for heat conduction is quite short, ~1% of the total lifetime. The timescale analysis indicates that the heat flux induced by evaporation or absorption can timely diffuse throughout the droplet volume so as to even out the temperature gradient within the droplet bulk, and we can consider the temperature distribution within the droplet as homogenous ($\nabla^2 T_{drop} = 0$) during most of the droplet lifetime.

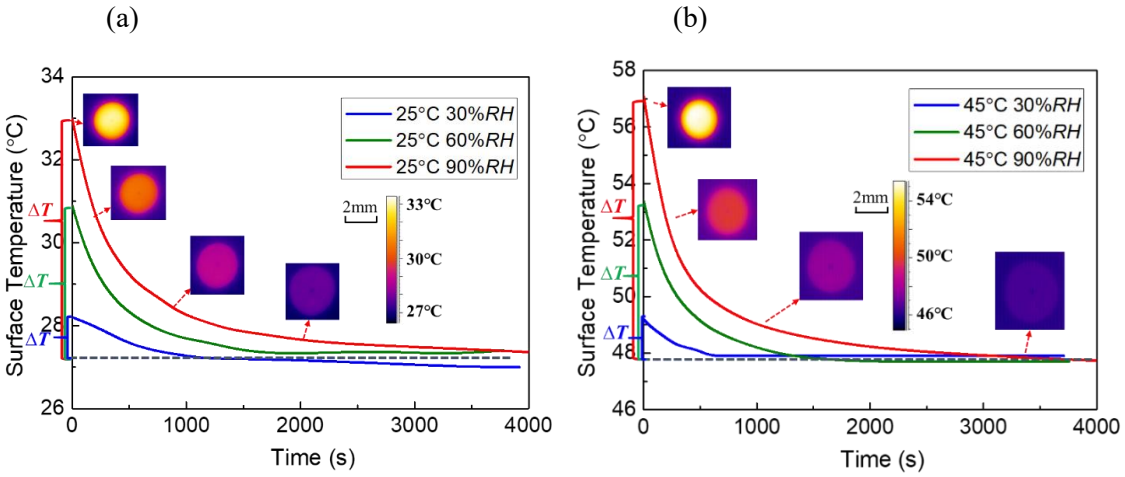

Figure 5.6 Evolution of average temperature at droplet surface and corresponding IR images during vapor absorption for ambient conditions of 30% *RH*, 60% *RH*, 90% *RH*, and (a) 25°C, (b) 45°C.

Even though the spatial temperature distribution across the droplet is homogenous, the average surface temperature of LiBr-H_2O droplets varies slowly along with time as a result of the balance between heat absorption and dissipation. To provide further evidences on the temperature evolution, Figure 5.6 shows the average temperature at the droplet surface in time along with characteristic IR thermography snapshots. It shows that

the temperature distribution along the droplet surface is nearly uniform throughout the vapor absorption process, which demonstrates experimentally the above timescale analysis of heat transfer within the droplet. The droplet surface experiences the highest temperature right after being deposited on the substrate. This indicates that vapor absorption starts as the droplet is generated from the needle and gets in contact with humid air. The released heat due to vapor-to-water phase change and absorption causes the observed temperature increase when respect to ambient conditions. After being deposited on the substrate, the absorbed heat is at the same time dissipated both through heat conduction towards the substrate, and through convective heat transfer into the ambient air. As a combined result of heat dissipation and decreasing absorption rate, the droplet surface gradually cools down towards equilibrium with the ambient as indicated by Figure 5.6. In the case of pure water, droplets experience the lowest surface temperature right after being deposited as they cool down due to evaporative cooling, then gradually warm up as they reach equilibrium with the ambient.

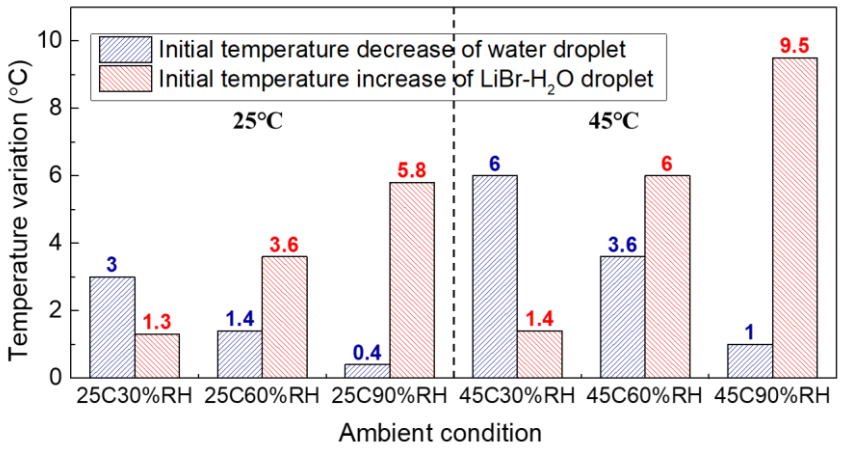

Figure 5.7 Initial temperature increase of LiBr-H_2O droplet caused by absorption heating (red columns), and temperature decrease of pure water droplet caused by evaporation cooling (blue columns) for the six experimental conditions.

Figure 5.7 summarizes the surface temperature increase of LiBr-H_2O droplets and decrease of pure water droplets right after droplet deposition for the six experimental conditions. The initial temperature change depends strongly on the ambient temperature

and relative humidity. In general, the initial temperature variation is more noticeable at high ambient temperature (45 °C) than at low temperature (25 °C) independently of the liquid or the relative humidity studied. For the same ambient temperature, the initial temperature rise of LiBr-H_2O droplets is more apparent at high relative humidity conditions, while the initial temperature decrease for pure water droplets becomes smaller at high relative humidity conditions. Typically, the increase in the surface temperature of a liquid desiccant droplet is function of the absorption rate, while the decrease in the surface temperature of a water droplet is proportional to the evaporation rate. Then, quantitative calculations of the average heat flux into the droplet surface can be carried out based on the surface area and on the vapor absorption rate, or the evaporation rate in the case of water droplets, by making use of Eq. (5.3). Vapor absorption and evaporation rates are calculated for the first instants right after droplet deposition.

$$\Phi_q = \frac{\dot{Q}}{S} = \frac{L_{vl}\rho\dfrac{dV}{dt}}{\pi\left(h^2 + R^2\right)}, \tag{5.3}$$

where Φ_q represents the average heat flux across the droplet surface, kW/m^2, $\dot{Q}$ is the rate of heat flow, kW, S repsrents the area of droplet surface, m^2, and L_{vl} is the latent heat released during vapor-liquid phase change, kJ/kg. The calculation results are summarized in Table 5.2.

Table 5.2 Average heat flux, Φ_q, at the interface of LiBr-H_2O droplets and pure water droplets induced by absorption heating and evaporation cooling. (Calculation results based on the vapor absorption rate and evaporation rate right after droplet deposition.)

Φ_q (W/m^2)	25°C 30%RH	25°C 60%RH	25°C 90%RH	45°C 30%RH	45°C 60%RH	45°C 90%RH
LiBr-H_2O droplet	5.07	10.66	11.66	4.72	15.12	17.71
Pure water droplet	11.32	8.12	2.16	28.48	14.43	3.33

The heat flux induced by absorption heating or evaporative cooling differs depending on the ambient condition. In the case of LiBr-H_2O droplets, the absorption heat flux follows the order of $\Phi_{q,45°C90\%RH} > \Phi_{q,45°C60\%RH} > \Phi_{q,25°C90\%RH} > \Phi_{q,25°C60\%RH} > \Phi_{q,25°C30\%RH}$

$\approx \Phi_{q,4530\%RH}$, which corresponds with the order of initial temperature rise in the six experimental conditions. Since vapor absorption is driven by the partial pressure difference between the ambient and the droplet surface, at low relative humidity conditions, *i.e.*, small gradient of concentration, the vapor absorption rate is rather low, hence similar values of average heat flux are reported for 30% *RH* conditions in Table 5.2. In the case of pure water droplets, the heat flux caused by evaporative cooling follows the order of $\Phi_{q,45°C30\%RH} > \Phi_{q,45°C60\%RH} > \Phi_{q,25°C30\%RH} > \Phi_{q,25°C60\%RH} > \Phi_{q,45°C90\%RH} > \Phi_{q,25°C90\%RH}$, which also corresponds with the order of initial temperature decrease at the surface of water droplets. For water droplets, evaporation is driven by the partial pressure difference from the droplet surface to the ambient; hence the high relative humidity conditions hinder droplet evaporation and the evaporative cooling effect. The quantitative calculations included above stress that the heat flux induced by absorption heating and evaporative cooling is the dominating factor for the initial temperature variation at the droplet surface during and right after droplet deposition. To accurately estimate the water vapor pressure at the droplet surface, the following mass transfer analysis takes into account the concentration variation within the droplet bulk and the temperature variation at the droplet surface captured by IR thermograph.

5.2.2. Mass transfer analysis

The mass transfer process includes the vapor diffusion on the air side, the vapor-water transition at the droplet interface, and the solute diffusion on the droplet side. Typically, the mass diffusion rate in the liquid phase is 10^3~10^4 times of that in the gas phase ($D_{\mathrm{water/air}}/D_{\mathrm{LiBr/LiBr-H_2O}} \sim 10^{-5}/10^{-9} \sim 10^4$)[143]. Therefore, the vapor absorption rate is limited by the mass diffusion process on the liquid side[138]. The solute diffusion rate, D_l, on the liquid phase is related to the liquid temperature, T, and dynamic viscosity, μ, according to the Stokes-Einstein equation[166]. For the cases of 45 °C and 25 °C, the ratio of solute diffusion rate within the droplet can be calculated as Eq. (5.4).

$$D_{\mathrm{l}} = \frac{k_B T}{6\pi\mu r}, \quad \frac{D_{T_1}}{D_{T_2}} = \frac{T_1}{T_2}\frac{\mu_{T_2}}{\mu_{T_1}}, \quad \frac{D_{\mathrm{l},45^\circ\mathrm{C}}}{D_{\mathrm{l},25^\circ\mathrm{C}}} = \frac{318.15}{298.15}\frac{0.004286}{0.002963} \approx 1.54, \tag{5.4}$$

where k_B represents the Boltzmann's constant, and r is the radius of the spherical particle, *i.e.*, the Li^+ and Br^- ions.

The above calculation presented in Eq. (5.4) shows that the solute diffusion rate at 45 °C is 50% greater than that at 25 °C. Hence, at higher temperature, the solute diffuses more effectively from the high concentration at the droplet bulk towards the interface. Then, droplets at higher temperature can maintain a relatively higher solute concentration at the droplet interface. In response to the higher salt concentration at the droplet interface, the vapor pressure is lower, and therefore the vapor absorption rate at 45 °C is higher when compared to 25 °C especially at the initial stage of vapor absorption. The greater absorption rates at high temperatures presented (in Table 5.1) in turn induce greater average heat flux and a further increase of the surface temperature (see Table 5.2 and Figure 5.7, respectively).

The vapor pressure at the droplet interface, $P_{\mathrm{vapor,surface}}$, can be evaluated according to the fitting correlations derived by Patek and Klomfar (Eqs. (5.5) and (5.6)) [137].

$$P_{vapor,surface} = P_{sat}\left(\Theta\right), \tag{5.5}$$

where P_{sat} is the saturation vapor pressure of pure water at "shifted temperature", Θ, due to the presence of dissolved salts. Θ is function of the mole fraction, x_{mole}, and temperature, T, of LiBr-H_2O solution, and can be calculated as Eq. (5.6).

$$\Theta = T - \sum_{i=1}^{8} a_i \left(x_{mole}\right)^{m_i} \left|0.4 - x_{mole}\right|^{n_i} \left(\frac{T}{T_c}\right)^{t_i}, \tag{5.6}$$

where T_{c} is the critical temperature of pure water, 647.096 K, a = {-2.41303×10^2, 1.91750×10^7, -1.75521×10^8, 3.25432×10^7, 3.92571×10^2, -2.12626×10^3, 1.85127×10^8, 1.91216×10^3}, m = {3, 4, 4, 8, 1, 1, 4, 6}, n = {0, 5, 6, 3, 0, 2, 6, 0}, t = {0, 0, 0, 0, 1, 1, 1, 1}, and the mole fraction, x_{mole}, is calculated by Eq. (5.7).

$$x_{mole} = \frac{x/M_{\mathrm{LiBr}}}{x/M_{\mathrm{LiBr}} + \left(1-x\right)/M_{\mathrm{H_2O}}}, \tag{5.7}$$

where x is the mass fraction of LiBr solute in LiBr-H_2O solution, and M represents the molar mass. Since the initial concentration of the LiBr-H_2O solution is known, any increase in the droplet volume is due to water absorbed, from experimental observations of droplet profile evolution in time, the mass fraction of LiBr can be estimated.

Then, combining Eq. (5.5), (5.6) and (5.7), the vapor pressure difference can be calculated. Because the vapor absorption rate is low and no apparent volume increase is observed at low relative humidity of 30% *RH*, in the following calculations we only consider 60% and 90% relative humidity conditions. Figure 5.8(a) shows the evolution of vapor pressure difference between the droplet interface and the ambient air during vapor absorption. From experimental observations of droplet profile, the vapor absorption rate is estimated in time, which is presented in Figure 5.8(b). Both Figure 5.8(a) and 5.8(b) clearly indicate that vapor pressure differences and absorption rates are greater right after droplet deposition, independently of the condition studied. As vapor absorption proceeds and the droplet gets diluted, the vapor pressure difference between the ambient and the droplet surface diminishes and so does the vapor absorption rate. Moreover, the order of initial vapor pressure difference, $\Delta P|_{45°C90\%RH} > \Delta P|_{45°C60\%RH} > \Delta P|_{25°C90\%RH} > \Delta P|_{25°C60\%RH}$, corresponds with the order of initial vapor absorption rate for the four experimental conditions, $dV/dt|_{45°C90\%RH} > dV/dt|_{45°C60\%RH} > dV/dt|_{25°C90\%RH} > dV/dt|_{25°C60\%RH}$.

According to Eqs. (5.5) and (5.6), the influence of $T_{surface}$ and x_{LiBr} on the vapor pressure at the droplet surface, $P_{vapor,surface}$, are opposite. On one hand, the increase in $T_{surface}$ induces the increase of $P_{vapor,surface}$, while on the other hand, the increase in x_{LiBr} causes the decrease of $P_{vapor,surface}$. Therefore, for constant ambient conditions, *i.e.*, constant P_{amb}, the driving force for vapor absorption, $\Delta P = P_{amb} - P_{vapor,surface}$, depends strongly on both $T_{surface}$ and x_{LiBr}. As the vapor absorption process proceeds, both $T_{surface}$ and x_{LiBr} decrease with time. The decreasing $T_{surface}$ tends to increase ΔP, whereas the decreasing x_{LiBr} tends to decrease ΔP. Results on the evolution of the vapor absorption driving force ΔP included in Figure 5.8(a) show a clear decreasing trend of ΔP along with vapor absorption time. The decreasing ΔP indicates that the influence of x_{LiBr} on ΔP

greatly outweighs the influence of $T_{surface}$. As the droplet gets further diluted, the driving force decreases along with time due to the decrease in x_{LiBr}, and the vapor absorption rate decreases accordingly as demonstrated in Figure 5.8(b).

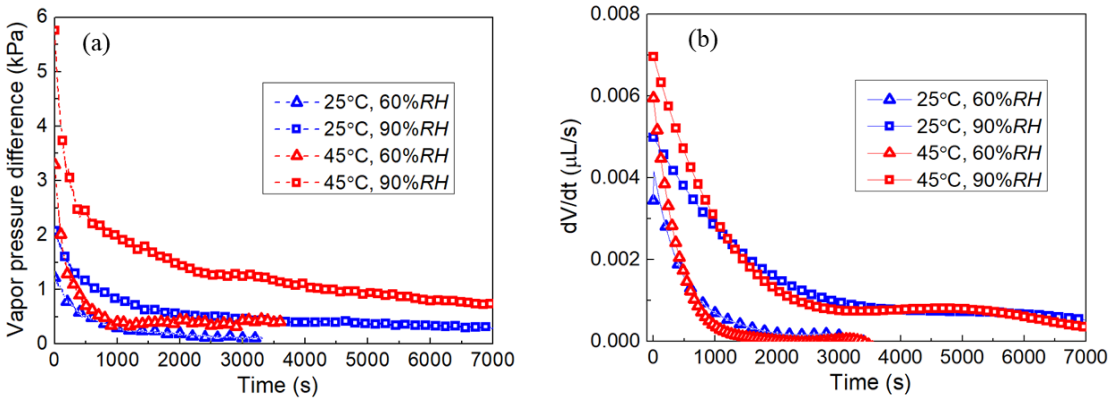

Figure 5.8 Evolution of (a) calculated vapor pressure difference between the droplet interface and ambient air, and (b) increasing rate of droplet volume, during vapor absorption on PTFE substrates for ambient conditions of 25°C, 45°C, and 60% *RH*, 90% *RH*.

5.2.3. Comparison with droplet evaporation

Based on the experimental results and analyses presented above, the main features during droplet evaporation and vapor absorption are summarized in Table 5.3.

Table 5.3 Summary of features during droplet evaporation and vapor absorption (TCL: triple contact line, *RH*: relative humidity, CCR: constant contact radius).

Comparison	Vapor absorption	Water evaporation
Droplet profile	Expands with advancing TCL	Shrinks with receding TCL
Rate of evaporation/ vapor absorption	Increases with temperature and increases with *RH*	Increases with temperature and decreases with *RH*
Heat transfer	Absorption heating, $T_{surface}$ increases initially, then decreases along with time	Evaporative cooling, $T_{surface}$ decreases initially, then increases along with time
Mass transfer	Solute diffusion dominates	Vapor diffusion dominates
Driving force	Decreases along with time Volume increases in a saturation trend	Constant if neglecting evaporative cooling effect Volume decreases linearly in the CCR mode

In the psychrometric chart in Figure 5.9, solid black lines present the iso-relative humidity curves of humid air at 20% *RH*, 40% *RH*, 60% *RH*, 80% *RH*, 100% *RH*, while

the dashed black lines present the iso-concentration curves of LiBr-H_2O solution at 20 wt.%, 30 wt.%, 40 wt.%, 50 wt.%, 60 wt.%. In the case of droplet evaporation, the equilibrium state of the liquid-air interface transits from W_0 to W_1 along the saturation line (100% *RH*), as marked with blue arrows in Figure 5.9. After droplet deposition, the droplet experiences the decrease in temperature due to evaporative cooling, and as the droplet attains equilibrium with the ambient, the temperature at the droplet surface increases. For the high humidity case 90% *RH* (Figure 5.9(a)) the temperature at the droplet surface increases from 45 °C to T_{amb}, *ca.* 46 °C, while for the low humidity case 30% *RH* (Figure 5.9(b)) the temperature increases from 40 °C to T_{amb}, *ca.* 45 °C. It is noteworthy to mention that at low ambient humidity conditions such as 30% *RH*, the effect of evaporative cooling is stronger due to the greater driving force, ΔP, hence the initial surface temperature is lower, and the temperature variation of the droplet surface is more apparent as presented in Figure 5.9(a).

(a) 45°C and 30% *RH* (b) 45°C and 90% *RH*

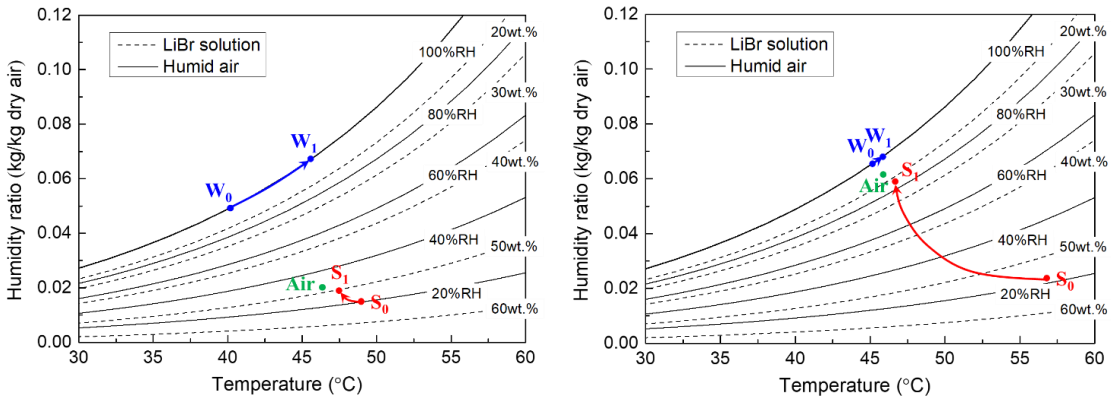

Figure 5.9 Psychrometric chart of humid air at different relative humidity (solid line), and equivalent humid air layer at the liquid-air interface with different concentrations (dash line). Marks inside the graph presents the state of ambient air (Green points, Air), the state variations of droplet during evaporation (blue arrows, $W_0 \rightarrow W_1$) and during vapor absorption (red arrows, $S_0 \rightarrow S_1$) for experimental conditions of 45°C, and (a) 30% *RH*, (b) 90% *RH*.

In the cases of liquid desiccant droplets, the state evolutions of LiBr-H_2O droplets during vapor absorption are marked in Figure 5.9 with red arrows from S_0 to S_1. Different from pure water droplet, the vapor pressure at the surface of LiBr-H_2O droplet is much

lower. In the case of 54 wt.% LiBr-H_2O droplet, the vapor pressure is theoretically in equilibrium with low humidity air of *ca.* 20% *RH*. As vapor absorption proceeds, LiBr-H_2O droplets get diluted with decreasing salt concentration due to water uptake. As a result, the state of LiBr-H_2O droplet moves across the iso-concentration curves shown in the psychrometric chart and toward equilibrium with the humid atmosphere. Moreover, the heat released due to vapor-water phase change also causes the temperature increase in the droplet surface at early stages shown as the initial state points of LiBr-H_2O droplets in Figure 5.9. At high ambient humidity such as 90% *RH*, the salt concentration of LiBr-H_2O droplet decreases more markedly due to the large amount of water uptake, which induces a stronger absorptive heating effect. Therefore, in high humidity cases, the state point moves across the iso-concentration curves with greater temperature decrease as depicted in Figure 5.9(b).

In the psychrometric chart in Figure 5.9, the solid lines present the states of humid air with different relative humidity (20% *RH*, 40% *RH*, 60% *RH*, 80% *RH*, 100% *RH*), while the dash lines present the states of LiBr-H_2O solution with different salt concentrations (20 wt.%, 30 wt.%, 40 wt.%, 50 wt.%, 60 wt.%). The state variations of pure water droplet during evaporation are marked with blue arrows. Along with droplet evaporation, the air state at the liquid-air interface transits from W_0 to W_1 along the saturation line (100% *RH*). Moreover, at low ambient humidity such as 30% *RH*, the effect of evaporation cooling is stronger, hence the initial surface temperature is lower, and the temperature variation of the droplet surface is more apparent as presented in Figure 5.9(a). The state evolution of LiBr-H_2O droplet during vapor absorption is marked with red arrows from S_0 to S_1. At high ambient humidity such as 90% *RH*, the effect of absorption heating is stronger, and the salt concentration decreases apparently due to the large amount of water uptake. Therefore, the state point moves a long distance with decreasing temperature across the iso-concentration lines as demonstrated in Figure 5.9(b).

5.3. Summary

The coupled heat and mass transfer process during vapor absorption into LiBr-H_2O droplet has been experimentally investigated under controlled environmental conditions. Due to the strong adhesion force of LiBr salt ions to water molecules, the vapor pressure at the droplet surface is greatly reduced, and water vapor diffuses from the air side to the liquid side, causing the growth of the droplet volume. Along with water vapor absorption, heat of absorption is released inducing a temperature increase at the droplet surface. IR thermography shows that desiccant droplets experience the highest surface temperature right after being deposited on the substrate, and then gradually cool down as a combined result of the decreasing vapor absorption rate and the heat dissipation into the substrate and into the ambient. Moreover, the initial temperature rise at the droplet surface is quantitatively in agreement with the absorption heat flux depending on the environmental conditions studied.

The variation of surface temperature, in turn influences the vapor pressure at the droplet surface, and affects the vapor diffusion on the air side. The vapor pressure difference between the ambient air and the droplet surface is evaluated taking account of the evolution of surface temperature as well as the evolution of salt concentration in the droplet bulk. Along with water uptake, the desiccant solution gets gradually diluted, and the vapor pressure difference between the ambient air and the droplet surface decreases along with time, therefore the rate of vapor absorption decreases. Furthermore, we compare and summarize the similarities and differences between the vapor absorption process into liquid desiccant droplets and the evaporation process of pure water droplets.

We conclude on the need for an accurate account of the coupling of heat and mass transfer mechanisms in order to provide a complete description of the vapor absorption process into liquid desiccant droplets, which is of great importance for the accurate design of the initial stage for dehumidification processes.

Part III Simulations

Chapter 6 Formulation of the lubrication model

In this chapter, we develop a lubrication-type model to describe the physical mechanisms governing the interactions between the hygroscopic liquid desiccant droplet, the vapor phase, and the solid substrate. We start from a description of the problem, then derive a mathematical model by applying necessary assumptions and simplifications. We assume the existence of a precursor film in front of the contact line to solve the contradiction between contact line motion and no-slip boundary condition, so that to remove the singularity near the triple contact line. The mass flux is derived according the equilibrium relation of chemical potential, which takes both the temperature difference and the vapor concentration difference into account. The scaled equations are further simplified using Kármán-Pohlhausen approximation. We arrive at a system of governing equations using the Galerkin method of weighted residuals, which is further solved by finite element method (FEM).

6.1. Main assumptions and limitations

We take lithium bromide aqueous solution (LiBr-H_2O) as an example for modelling. In a LiBr-H_2O droplet, the lithium bromide salt exists as Li^+ ions and Br^- ions, which have high adhesion force to water molecules. As a result, the water vapor pressure at the droplet liquid-air interface is apparently lowered compared to pure water droplet. Depending on the ambient condition, the LiBr-H_2O droplet will absorb water vapor (at high ambient humidity) or desorb water vapor (when the ambient humidity is extremely low). During the vapor absorption process, the mass of LiBr salt follows the solute conservation law, and the mass of water inside the droplet bulk changes along with time.

The mass transfer process can be divided into the vapor diffusion on the air side, the vapor-water phase change at the droplet interface, and the solute diffusion within the droplet bulk. Typically, the mass diffusion rate in the air phase is $10^3 \sim 10^4$ times of that in the liquid phase ($D_{\mathrm{water/air}}/D_{\mathrm{LiBr/LiBr-H_2O}} \sim 10^{-5}/10^{-9} \sim 10^4$)[143]. Therefore, we can

assume that the distribution of water vapor at the air side as homogeneous, and the vapor absorption process is limited by the solute diffusion within the droplet. Along with mass transport, the latent heat released due to vapor-water phase change causes apparent temperature increase at the droplet interface, and induces temperature gradient within the droplet. The concentration and temperature gradients will further induce surface tension gradient across the droplet interface, and affect the droplet kinetics along with time.

Experiments show that droplets on a hydrophilic substrate gradually spread along with volume expansion, and the contact angle decreases from *ca.* 70° to *ca.* 40° during the vapor absorption process with a time scale of ~10^3 s. On a hydrophobic substrate with contact angle close to 90°, the evolution of droplet profile is close to a constant contact angle mode. The simulation aims to reveal the spatial distribution and temporal evolution of temperature and salt concentration within the droplet, and explain the observed spreading phenomena of droplets on hydrophilic glass substrates.

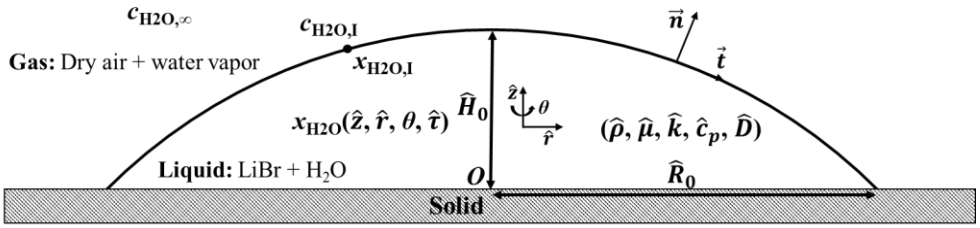

Figure 6.1 A sessile lithium bromide – water (LiBr-H_2O) droplet in contact with humid air (mixture of dry air and water vapor): $\hat{H}_0/\hat{R}_0$ is assumed as $\ll 1$, $x_{w,l}(\hat{z}, \hat{r}, \theta, \hat{\tau})$ refers to the mass fraction of water inside the droplet (1-$x_{LiBr,l}$), $x_{w,s}$ refers to the mass fraction of water at the droplet interface, $c_{H2O,I}$ refers to the water vapor concentration in the humid air layer near the droplet interface, $c_{H2O,\infty}$ refers to the water vapor concentration in the air bulk, and is assumed as constant, $\vec{n}$ and $\vec{t}$ denote the outward units vectors acting in normal and tangential directions to the interface respectively. The center of droplet basis in contact with the substrate, *O*, is defined as the origin of the coordinate.

In the model, the solution droplet is considered as Newtonian fluid and assumed as incompressible. The thermal properties of LiBr-H_2O solution are function of temperature and solute concentration, and vary both spatially and temporally as vapor absorption takes place. Compared to the influence of solute concentration, the influences of temperature

on solution properties are much weaker. For simplification, the specific heat capacity, $\hat{c}_p$, density, $\hat{\rho}$ [137], and thermal conductivity, $\hat{k}$ [167], of LiBr-H_2O solution are approximated as linearly function of solute concentration, χ_{LiBr}. Moreover, we neglect the influence of solution temperature since the influences of solute concentration on the fluid properties are much more apparent.

$$\hat{c}_p = \hat{c}_{p,\mathrm{H_2O}} + \hat{\eta}_{c_p}\chi_{\mathrm{LiBr}}, \tag{6.1}$$

$$\hat{\rho} = \hat{\rho}_{\mathrm{H_2O}} + \hat{\eta}_{\rho}\chi_{\mathrm{LiBr}}, \tag{6.2}$$

$$\hat{k} = \hat{k}_{\mathrm{H_2O}} + \hat{\eta}_{k}\chi_{\mathrm{LiBr}}, \tag{6.3}$$

where $\hat{c}_{p,\mathrm{H_2O}}$, $\hat{\rho}_{\mathrm{H_2O}}$, and $\hat{k}_{\mathrm{H_2O}}$ is respectively the heat capacity, density and thermal conductivity of pure water, $\hat{\eta}_{c_p}$, $\hat{\eta}_{\rho}$, and $\hat{\eta}_{k}$ is respectively the coefficient of heat capacity, density, and thermal conductivity depending on the mass concentration of LiBr solute, $\hat{\chi}_{\mathrm{LiBr}}$. The viscosity, $\hat{\mu}$, of LiBr-H_2O solution is approximated with the eq. (6.4), where $\hat{a}_1$, b_1, and b_2 are fitting coefficients.

$$\hat{\mu} = \frac{\hat{a}_1}{\chi_{\mathrm{LiBr}}^2 + b_1\chi_{\mathrm{LiBr}} + b_2}, \tag{6.4}$$

The surface tension of the LiBr-H_2O solution, $\hat{\sigma}$, is approximated with an empirical correlation of solute concentration and surface temperature[168].

$$\hat{\sigma} = \hat{\sigma}_{\mathrm{H_2O}} + \hat{\eta}_{\sigma}\chi_{\mathrm{LiBr}} + \hat{\zeta}_{\sigma}\left(\hat{T} - \hat{T}_{\mathrm{ref}}\right), \tag{6.5}$$

where $\hat{\eta}_{\sigma}$ is the surface tension coefficient of solute concentration, $\hat{\zeta}_{\sigma}$ is the surface tension coefficient of solution temperature, and $\hat{T}_{\mathrm{ref}}$ is the reference temperature, 20 °C. The values of the fitting coefficients are listed below.

Table 6.1 Dimensional fitting coefficients of solution properties.

$\hat{c}_{p,\mathrm{H_2O}}$	$\hat{\rho}_{\mathrm{H_2O}}$	$\hat{k}_{\mathrm{H_2O}}$	$\hat{\sigma}_{\mathrm{H_2O}}$	$\hat{\eta}_{c_p}$	$\hat{\eta}_{\rho}$
4.18	998.2	0.598	72.75	-3.94	1231.5

$\hat{\eta}_k$	$\hat{\eta}_\sigma$	$\hat{\zeta}_\sigma$	$\hat{a}_1$	b_1	b_2
-0.324	43.5	-0.205	316.4	-447.5	314.8

Initially, we assume that the droplet has maximal thickness $\hat{H}_0$ and radius $\hat{R}_0$. We consider the droplet to be very thin and therefore $\hat{R}_0$ greatly exceeds $\hat{H}_0$ so that the aspect ratio $\varepsilon = \hat{H}_0/\hat{R}_0 \ll 1$. This assumption permits the use of lubrication theory which is the key theory we apply to derive the evolution equations.

The droplet is in contact with the gas phase characterized by constant temperature and relative humidity. Compared with the liquid phase, the density, viscosity, and thermal conductivity of air are significantly smaller and can be neglected, namely, $\hat{\rho}_\mathrm{v} \ll \hat{\rho}_\mathrm{l}$, $\hat{\mu}_\mathrm{v} \ll \hat{\mu}_\mathrm{l}$, $\hat{k}_\mathrm{v} \ll \hat{k}_\mathrm{l}$. Moreover, since the vapor absorption is a liquid-phase-dominated process, we apply a one-side model which considers only the fluid flow and state evolution of the droplet side. By eliminating the gas phase, the one-side model is efficient and can be solved with modest resources in short time. The model assumes the gas phase as sufficiently large, and the temperature and relative humidity remain unchanged as vapor absorption takes place. The assumption is reasonable for a well-ventilated environment, which is also the case of the experimental chamber where good ventilation is provided to meet the requirement of constant temperature and humidity. Moreover, the one-side model means that the mass transfer onto the droplet interface is not caused by vapor diffusion on the air side, and rather controlled by the transfer of molecules across the liquid-vapor interface. This means that the one-side model will qualitatively simulate vapor absorption, while a quantitative comparison with absorptive mass fluxes in contrast with diffusion-limited experiments (weak air convection) is impossible. However, the one-side model is sufficient to reveal the fluid flow and the distribution of temperature and concentration inside the droplet, which helps to explain the droplet kinetics related with the evolution of interfacial parameters.

For the mass transport within the droplet, we consider only the Fick's law, while both the temperature-gradient-induced Soret effect and the concentration-gradient-induced Dufour effect are neglected. Along with vapor absorption, the effect of absorptive heating

will increase the temperature of droplet interface, and induce a temperature gradient within the droplet. In the modelling, we assume the thermal conductivity of the substrate as sufficiently high, therefore the substrate temperature remains unchanged despite the absorptive heating effect. For a less conductive substrate, the rate of vapor absorption can be slightly lowered due to the absorptive heating effect. However, the assumption will not have much influence on the simulation results as the vapor absorption process is mainly dominated by the concentration difference.

To remove the stress singularity that may arise at the moving contact line, a precursor film is assumed to exist around the periphery of the droplet. The precursor film is sufficiently thin that the adsorption of water molecules to the substrate is enhanced by van der Waals interactions. The existence of precursor film is also verified with experiments and the thickness is in the order of $10\sim10^2$ nm. The extremely small thickness also indicates that the precursor film gets saturated very easily right after getting contact with humid air, reaching an environmental equilibrium state.

6.2. Dimensional governing Equations

As marked in Figure 6.1, a cylindrical coordinate system, ($\hat{z}$, $\hat{r}$, θ), is applied to describe the problem and solve the velocity field, $\hat{\boldsymbol{u}}$ = ($\hat{u}$, $\hat{v}$, $\hat{\omega}$), where $\hat{u}$, $\hat{v}$, and $\hat{\omega}$ correspond to the horizontal, azimuthal and vertical components of the velocity field respectively. The center of droplet basis in contact with the substrate, *O*, is defined as the origin of the coordinate. The liquid-vapor interface is located at $\hat{z} = \hat{h}(\hat{r},\hat{t})$, while the liquid-solid and liquid-vapor interfaces are located at $\hat{z} = 0$.

The liquid phase is governed by the incompressible mass, momentum, energy and concentration equations,

$$\frac{\partial\hat{\rho}}{\partial\hat{t}} + \hat{\nabla}\cdot\left(\hat{\rho}\hat{\boldsymbol{u}}\right) = 0\,, \tag{6.6}$$

$$\hat{\rho}\left(\frac{\partial\hat{\boldsymbol{u}}}{\partial\hat{t}} + \hat{\boldsymbol{u}}\cdot\hat{\nabla}\hat{\boldsymbol{u}}\right) = \hat{\nabla}\cdot\hat{\mathbf{T}} + \hat{\rho}\hat{\boldsymbol{g}}_{\mathrm{G}}\,, \tag{6.7}$$

$$\hat{\rho}\hat{c}_p\left(\frac{\partial\hat{T}}{\partial\hat{t}}+\hat{\boldsymbol{u}}\cdot\hat{\nabla}\hat{T}\right)=\hat{\nabla}\cdot\left(\hat{k}\hat{\nabla}\hat{T}\right), \tag{6.8}$$

$$\frac{\partial\chi_{\mathrm{H_2O}}}{\partial\hat{t}}+\hat{\boldsymbol{u}}\cdot\hat{\nabla}\chi_{\mathrm{H_2O}}=\hat{\nabla}\cdot\left(\hat{D}_{\mathrm{H_2O}}\hat{\nabla}\chi_{\mathrm{H_2O}}\right), \tag{6.9}$$

where $\hat{D}_{\mathrm{H_2O}}$ denotes the mass diffusion coefficient of water molecules in aqueous solution, $\hat{\chi}_{\mathrm{H_2O}}$ denotes the mass fraction of water in LiBr-H_2O solution, $\hat{\mathbf{T}}$ refers to the total stress tensor in the liquid, defined as,

$$\hat{\mathbf{T}}=-\hat{p}\mathbf{I}+\hat{\mu}\left(\hat{\nabla}\hat{\boldsymbol{u}}+\hat{\nabla}\hat{\boldsymbol{u}}^T\right), \tag{6.10}$$

where I denotes the identity tensor.

Then we derive the boundary conditions to complete the formulation of the vapor absorption problem. As depicted in Figure 6.1, the ***n*** and ***t*** refer to the outward vectors which are normal and tangential to the interface respectively, and can be expressed as,

$$\boldsymbol{n}=\left(-\frac{\partial\hat{h}}{\partial\hat{\tau}},1\right)\left(1+\left(\frac{\partial\hat{h}}{\partial\hat{\tau}}\right)^2\right)^{-\frac{1}{2}}, \tag{6.11}$$

$$\boldsymbol{t}=\left(1,-\frac{\partial\hat{h}}{\partial\hat{\tau}}\right)\left(1+\left(\frac{\partial\hat{h}}{\partial\hat{\tau}}\right)^2\right)^{-\frac{1}{2}}. \tag{6.12}$$

Along the droplet interface, the boundary condition of absorptive mass flux can be expressed by the relationship between the velocity of the liquid solution, $\hat{\boldsymbol{u}}$, and the velocity of the interface, $\hat{\boldsymbol{u}}_s$ = ($\hat{u}_s$,$\hat{\omega}_s$), shown as eq. (6.13).

$$\left(\hat{\boldsymbol{u}}-\hat{\boldsymbol{u}}_{\mathrm{s}}\right)\cdot\boldsymbol{n}=\frac{\hat{J}}{\hat{\rho}}, \tag{6.13}$$

where $\hat{J}$ denotes the absorptive mass flux of water vapor, $\hat{\rho}$ denotes the density of solution near the droplet interface. The tangential components of the two velocities are the same: $\hat{\boldsymbol{u}}_r=\hat{\boldsymbol{u}}-\left(\hat{\boldsymbol{u}}\cdot\boldsymbol{n}\right)\boldsymbol{n}=\hat{\boldsymbol{u}}_{\mathrm{s}}-\left(\hat{\boldsymbol{u}}_{\mathrm{s}}\cdot\boldsymbol{n}\right)\boldsymbol{n}$. The absorptive mass flux of water vapor is assumed to be normal to the interface. The liquid-vapor jump conditions can then be given by the jump mass balance and jump energy balance taking account of the latent heat

release at the liquid-vapor interface.

$$\hat{J}=\hat{\rho}\left(\hat{\boldsymbol{u}}-\hat{\boldsymbol{u}}_{\mathrm{s}}\right)\cdot\boldsymbol{n}=\hat{\rho}_{\mathrm{g}}\left(\hat{\boldsymbol{u}}_{\mathrm{g}}-\hat{\boldsymbol{u}}_{\mathrm{s}}\right)\cdot\boldsymbol{n}, \tag{6.14}$$

$$\hat{J}\hat{L}_{\mathrm{H_2O}}+\hat{k}\hat{\nabla}\hat{T}\cdot\boldsymbol{n}=\hat{k}_{\mathrm{g}}\hat{\nabla}\hat{T}_{\mathrm{g}}\cdot\boldsymbol{n}, \tag{6.15}$$

where subscript *g* denotes the gas phase, and $\hat{\rho}_{\mathrm{g}}$, $\hat{\boldsymbol{u}}_{\mathrm{g}}$, $\hat{k}_{\mathrm{g}}$, $\hat{T}_{\mathrm{g}}$ refer to the density, velocity, thermal conductivity, and temperature of the gas phase respectively.

To balance the jump in normal stress with the surface tension, mean curvature and van der Waals interactions, a normal stress boundary balance is defined at the interface,

$$\boldsymbol{n}\cdot\left(\hat{\mathbf{T}}-\hat{\mathbf{T}}_{\mathrm{g}}\right)\cdot\boldsymbol{n}=2\hat{\kappa}\hat{\sigma}+\hat{\Pi}, \tag{6.16}$$

where $\hat{\mathbf{T}}$ denotes the total stress tensor of liquid phase given in Eq. (5), and $\hat{\mathbf{T}}_{\mathrm{g}}$ denotes the total stress tensor of gas phase. $2\hat{\kappa}=-\hat{\nabla}_{s}\cdot\boldsymbol{n}$ is twice the mean curvature of the free surface and $\hat{\nabla}_{s}=\left(\mathbf{I}-\boldsymbol{nn}\right)\cdot\hat{\nabla}$ is the surface gradient operator. Surface tension of the liquid, $\hat{\sigma}$, is given by the empirical correlation function[137] of liquid temperature and salt concentration. $\hat{\Pi}$ denotes the disjoining pressure accounting for intermolecular interactions near the contact line,

$$\hat{\Pi}=\frac{\hat{\mathcal{A}}}{6\pi\hat{h}^{3}}, \tag{6.17}$$

with $\hat{\mathcal{A}}$ being the dimensional Hamaker constant. Here, we consider a small drop where surface tension dominates. By ignoring the effect of motion of water molecules towards the droplet interface, and by ignoring the stress from the gas phase (since the gas viscosity is negligible compared with the liquid phase), the normal stress boundary balance eq. (6.16) is derived as,

$$-\hat{p}+\boldsymbol{n}\cdot\hat{\boldsymbol{\tau}}\cdot\boldsymbol{n}=2\hat{\kappa}\hat{\sigma}+\hat{\Pi}-\hat{p}_{\mathrm{g}}, \tag{6.18}$$

where $\hat{p}$ is the pressure of the liquid phase, $\hat{p}_{\mathrm{g}}$ is the total pressure of the gas phase, and $\hat{\boldsymbol{\tau}}$ is the shear stress tensor of the liquid phase.

The tangential stress boundary condition indicates the balance between the shear

stress jump and the surface tension gradient,

$$\boldsymbol{n}\cdot\left(\hat{\mathbf{T}}-\hat{\mathbf{T}}_{\mathrm{g}}\right)\cdot\boldsymbol{t}=\hat{\nabla}_{s}\hat{\sigma}\cdot\boldsymbol{t}\,. \tag{6.19}$$

By ignoring the shear stress from the gas phase due to apparently lower gas viscosity, eq. (6.19) becomes,

$$\boldsymbol{n}\cdot\hat{\mathbf{T}}\cdot\boldsymbol{t}=\hat{\nabla}_{s}\hat{\sigma}\cdot\boldsymbol{t}\,. \tag{6.20}$$

The concentration balance of water vapor over the interface is defined as,

$$\begin{aligned}&\chi_{\mathrm{LiBr}}\hat{\rho}\left(\hat{\boldsymbol{u}}-\hat{\boldsymbol{u}}_{\mathrm{s}}\right)\cdot\boldsymbol{n}-\hat{D}_{\mathrm{LiBr}}\left(\boldsymbol{n}\cdot\hat{\nabla}\chi_{\mathrm{LiBr}}\right)_{\hat{z}=\hat{h}}=0\text{, or rather,}\\&\left(1-\chi_{\mathrm{H_2O}}\right)\hat{\rho}\left(\hat{\boldsymbol{u}}-\hat{\boldsymbol{u}}_{\mathrm{s}}\right)\cdot\boldsymbol{n}+\hat{D}_{\mathrm{H_2O}}\left(\boldsymbol{n}\cdot\hat{\nabla}\chi_{\mathrm{H_2O}}\right)_{\hat{z}=\hat{h}}=0\,.\end{aligned} \tag{6.21}$$

Combining with the jump mass balance, eq. (6.14), the concentration balance boundary condition becomes,

$$\hat{D}_{\mathrm{H_2O}}\left(\boldsymbol{n}\cdot\hat{\nabla}\chi_{\mathrm{H_2O}}\right)_{\hat{z}=\hat{h}}=\hat{J}\left(\chi_{\mathrm{H_2O}}-1\right). \tag{6.22}$$

The motion of free surface can be described with the kinematic boundary condition, expressed as eq. (6.23),

$$\frac{\partial\hat{h}}{\partial\hat{t}}+\hat{u}_{s}\frac{\partial\hat{h}}{\partial\hat{r}}+\frac{\hat{v}_{s}}{\hat{r}}\frac{\partial\hat{h}}{\partial\theta}=\hat{w}_{s}\,. \tag{6.23}$$

Along the liquid-solid interface ($\hat{z}=0$), no-slip and zero vertical concentration flux boundary conditions are applied,

$$\hat{u}=0\,,\qquad\hat{w}=0\,,\qquad\frac{\partial\chi_{\mathrm{H_2O}}}{\partial\hat{z}}=0\,,\qquad\hat{T}=\hat{T}_{\mathrm{w}}\,. \tag{6.24}$$

Finally, we need to complete the model by giving a proper expression for the absorptive mass flux of water vapor along the droplet interface. The Hertz–Knudsen equation is commonly used for predicting the mass flux induced by evaporation or condensation towards a liquid-vapor interface. The equation relates the mass flux with the difference between the actual vapor pressure at the droplet interface and the equilibrium vapor pressure when the mass transfer between the liquid and gas phase reaches a balance. Specifically, the Hertz–Knudsen equation[169] can be expressed as eq. (6.25).

$$\hat{J}=\sqrt{\frac{\hat{m}}{2\pi\hat{k}_B}}\left(\alpha_{\mathrm{e}}\frac{\hat{p}_{v,\mathrm{e}}}{\sqrt{\hat{T}_{\mathrm{S}}^{\mathrm{L}}}}-\alpha_{\mathrm{c}}\frac{\hat{p}_{v,\mathrm{S}}}{\sqrt{\hat{T}_{\mathrm{S}}^{\mathrm{V}}}}\right)=\sqrt{\frac{\hat{M}_{\mathrm{H_2O}}}{2\pi\hat{R}_g}}\left(\alpha_{\mathrm{e}}\frac{\hat{p}_{v,\mathrm{e}}}{\sqrt{\hat{T}_{\mathrm{S}}^{\mathrm{L}}}}-\alpha_{\mathrm{c}}\frac{\hat{p}_{v,\mathrm{S}}}{\sqrt{\hat{T}_{\mathrm{S}}^{\mathrm{V}}}}\right), \tag{6.25}$$

where $\hat{m}$ denotes the mass of a water molecule, $\hat{m}=\frac{\hat{M}_{\mathrm{H_2O}}}{N_A}$, among which $\hat{M}_{\mathrm{H_2O}}$ is the molar mass of water, and N_A is the Avogadro constant, 6.022×10^{23}. $\hat{k}_B$ denotes the Boltzmann constant, 1.38064852×10^{-23} $\mathrm{m^2/(kg\cdot s^2\cdot K)}$, $\hat{R}_g$ denotes the gas constant, 8.314 J/(mol·K). $\hat{T}_{\mathrm{S}}$ is the temperature of liquid-air interface, $\hat{p}_{v,\mathrm{S}}$ is the interfacial vapor pressure at the droplet surface, $\hat{p}_{v,e}$ is the equilibrium vapor pressure with the gas phase, α_{e} and α_{c} are mass accommodation coefficient of evaporation and condensation respectively. In this model, the temperature at the liquid-air interface is assumed to be continuous, $\hat{T}_{\mathrm{S}}^{\mathrm{L}}=\hat{T}_{\mathrm{S}}^{\mathrm{V}}=\hat{T}_{\mathrm{S}}$, and we assume that the system is always near equilibrium, $\alpha_{\mathrm{e}}=\alpha_{\mathrm{c}}=1$, and $\hat{T}_{\mathrm{S}}\approx\hat{T}_{\mathrm{g}}$. Moreover, we consider the LiBr-H_2O solution as an ideal solution, and the water vapor pressure at the liquid-air interface follows the Raoults's law, $\hat{p}_{\mathrm{v,S}}=\chi_{\mathrm{H_2O}}\hat{p}_{\mathrm{v,sat}}$, where $\hat{p}_{v,\mathrm{sat}}$ is the saturation vapor pressure above pure water. Eq. (6.25) then becomes,

$$\hat{J}=\chi_{\mathrm{H_2O}}\hat{p}_{\mathrm{v,sat}}\sqrt{\frac{\hat{M}_{\mathrm{H_2O}}}{2\pi\hat{R}_g\hat{T}_{\mathrm{g}}}}\left(\frac{\hat{p}_{v,\mathrm{e}}}{\hat{p}_{v,\mathrm{S}}}-1\right). \tag{6.26}$$

At the thermodynamic equilibrium state, the chemical potential of gas phase and liquid phase across the liquid-air interface reaches balance, and the following relation can be derived.

$$\ln\left(\frac{\hat{p}_{\mathrm{v,e}}}{\hat{p}_{\mathrm{v,S}}}\right)=\frac{\hat{M}_{\mathrm{H_2O}}}{\hat{\rho}_{\mathrm{H_2O}}\hat{R}_g\hat{T}_{\mathrm{g}}}\left(\hat{p}-\hat{p}_{\mathrm{g}}\right)+\frac{\hat{M}_{\mathrm{H_2O}}\hat{L}_{\mathrm{H_2O}}}{\hat{R}_g\hat{T}_g^2}\left(\hat{T}_{\mathrm{S}}-\hat{T}_{\mathrm{g}}\right)+\ln\left(\frac{\chi_{\mathrm{H_2O}}}{\chi_{\mathrm{H_2O,g}}}\right). \tag{6.27}$$

As $\hat{p}_{\mathrm{v,S}}$ gets close to $\hat{p}_{\mathrm{v,e}}$, $\ln\left(\frac{\hat{p}_{\mathrm{v,e}}}{\hat{p}_{\mathrm{v,S}}}\right)\approx\frac{\hat{p}_{\mathrm{v,e}}}{\hat{p}_{\mathrm{v,S}}}-1$. Therefore, the absorptive mass flux can be derived as,

$$\hat{J}=\chi_{\mathrm{H_2O}}\hat{p}_{\mathrm{v,sat}}\sqrt{\frac{\hat{M}_{\mathrm{H_2O}}}{2\pi\hat{R}_g\hat{T}_{\mathrm{g}}}}\left(\frac{\hat{M}_{\mathrm{H_2O}}}{\hat{\rho}_{\mathrm{H_2O}}\hat{R}_g\hat{T}_{\mathrm{g}}}\left(\hat{p}-\hat{p}_{\mathrm{g}}\right)+\frac{\hat{M}_{\mathrm{H_2O}}\hat{L}_{\mathrm{H_2O}}}{\hat{R}_g\hat{T}_g^2}\left(\hat{T}_{\mathrm{S}}-\hat{T}_{\mathrm{g}}\right)+\ln\left(\frac{\chi_{\mathrm{H_2O}}}{\chi_{\mathrm{H_2O,g}}}\right)\right). \quad (6.28)$$

6.3. Scaling and resulting dimensionless equations

6.4.1. Governing equations

In this vapor absorption problem, the droplet, the substrate and surrounding atmosphere are initially at an equilibrium temperature, the driving force for vapor absorption is the concentration difference of water vapor between the gas phase and the liquid-air interface. As vapor absorption takes place, a concentration gradient will be induced across the droplet interface due to the asymmetric shape of hydrophilic droplet. The concentration difference across the droplet surface will induce a gradient of surface tension and subsequently the Marangoni flow. In the modelling, we apply the solutal capillary velocity, eq. (6.29), as the characteristic velocity of the system.

$$\hat{u}^*=\frac{\varepsilon\hat{\eta}_\sigma\Delta\chi_{\mathrm{H_2O}}}{\hat{\mu}}, \quad (6.29)$$

where $\hat{u}^*$ denotes the characteristic velocity of the system, and $\hat{\eta}_\sigma=\left|\frac{\partial\hat{\sigma}}{\partial\chi_{\mathrm{H_2O}}}\right|$, is the concentration coefficient of surface tension of LiBr-H_2O solution.

The thermophysical properties of the liquid are characterized by the corresponding properties of pure water. The important properties of pure water and 54 wt. % LiBr-H_2O solution (initial solute concentration) are listed in Table 3.1.

The following scaling quantities are applied to formulate the governing equations and boundary conditions for the vapor absorption model. The crowning with a “cap” (^) over a symbol denotes a dimensional quantity while the absence denotes a dimensionless quantity.

$$\hat{r}=\hat{R}_0 r, \qquad \hat{z}=\hat{H}_0 z, \qquad \left(\hat{u},\hat{v},\hat{w}\right)=\left(\hat{u}^*u,\hat{u}^*v,\frac{\hat{H}_0}{\hat{R}_0}\hat{u}^*w\right), \quad (6.30)$$

$$\hat{\rho}=\hat{\rho}_{\mathrm{H_2O}}\rho,\quad \hat{\mu}=\hat{\mu}_{\mathrm{H_2O}}\mu,\quad \hat{\sigma}=\hat{\sigma}_{\mathrm{H_2O}}\sigma,\quad \hat{c}_p=\hat{c}_{p,\mathrm{H_2O}}c_p,$$

$$\hat{k}=\hat{k}_{\mathrm{H_2O}}k,$$

$$\hat{p}=\hat{p}_g+\frac{\hat{\mu}_{\mathrm{H_2O}}\hat{u}^*\hat{R}_0}{\hat{H}_0^2}p,\qquad \hat{t}=\frac{\hat{R}_0}{\hat{u}^*}t,\qquad \hat{J}=\frac{\hat{\rho}_{\mathrm{H_2O}}\hat{D}_{\mathrm{H_2O}}\Delta\chi_{\mathrm{H_2O}}}{\hat{H}_0}J,$$

$$\hat{T}=\hat{T}_{\mathrm{ref}}+T\Delta\hat{T},\qquad \Delta\hat{T}=\frac{\hat{\rho}_{\mathrm{H_2O}}\hat{D}_{\mathrm{H_2O}}\hat{L}_{\mathrm{H_2O}}\Delta\chi_{\mathrm{H_2O}}}{\hat{k}_{\mathrm{H_2O}}}.$$

Here, $\Delta\chi_{\mathrm{H_2O}}$ is the largest possible concentration difference within the droplet, defined as the difference between the water concentration of pure water, $\chi_{\mathrm{H_2O}}=100$ wt.%, and the water concentration of LiBr-H_2O solution we investigated, $\chi_{\mathrm{H_2O}}=1-\chi_{\mathrm{LiBr}}$. $\hat{T}_{\mathrm{ref}}$ is the reference temperature of the system, and here we define it as 20 °C.

The dimensionless solution properties of LiBr-H_2O solution, normalized by the thermal properties of pure water at 20 °C and at 1 atm are thus derived as,

$$c_p=1+\eta_{c_p}\chi_{\mathrm{LiBr}},\ \eta_{c_p}=\frac{\hat{\eta}_{c_p}}{\hat{c}_{p,\mathrm{H_2O}}},\tag{6.1'}$$

$$\rho=1+\eta_\rho\chi_{\mathrm{LiBr}},\ \eta_\rho=\frac{\hat{\eta}_\rho}{\hat{\rho}_{\mathrm{H_2O}}},\tag{6.2'}$$

$$k=1+\eta_k\chi_{\mathrm{LiBr}},\ \eta_k=\frac{\hat{\eta}_k}{\hat{k}_{\mathrm{H_2O}}},\tag{6.3'}$$

$$\mu=\frac{a_1}{\chi_{\mathrm{LiBr}}^2+b_1\chi_{\mathrm{LiBr}}+b_2},\ a_1=\frac{\hat{a}_1}{\hat{\mu}_{\mathrm{H_2O}}},\tag{6.4'}$$

$$\sigma=1+\eta_\sigma\chi_{\mathrm{LiBr}}+\zeta_\sigma T,\ \eta_\sigma=\frac{\hat{\eta}_\sigma}{\hat{\sigma}_{\mathrm{H_2O}}},\ \zeta_\sigma=\frac{\hat{\zeta}_\sigma\Delta\hat{T}}{\hat{\sigma}_{\mathrm{H_2O}}}.\tag{6.5'}$$

Table 6.2 Dimensionless fitting coefficients of solution properties.

η_{c_p}	η_ρ	η_k	η_σ	ζ_σ	a_1	b_1	b_2
-0.943	1.234	-0.542	0.598	-0.0069	314.8	-447.5	314.8

During the scaling process, the lubrication theory is applied with an assumption that

the drop aspect ratio $\varepsilon = \hat{H}_0/\hat{R}_0 \ll 1$. Moreover, the relations between the stress components and the velocity gradients are applied to further simplify the momentum equations.

$$\hat{\tau}_{rz} = \hat{\tau}_{zr} = \hat{\mu}\left(\frac{\partial \hat{w}}{\partial \hat{r}} + \frac{\partial \hat{u}}{\partial \hat{z}}\right), \qquad \hat{\tau}_{\theta z} = \hat{\tau}_{z\theta} = \hat{\mu}\left(\frac{\partial \hat{v}}{\partial \hat{z}} + \frac{1}{\hat{r}}\frac{\partial \hat{w}}{\partial \theta}\right). \tag{6.31}$$

By scaling and applying the assumption, $\varepsilon = \hat{H}_0/\hat{R}_0 \ll 1$, the stress components are further derived as,

$$\tau_{rz} = \tau_{zr} = \mu\left(\frac{\partial u}{\partial z}\right), \qquad \tau_{\theta z} = \tau_{z\theta} = \mu\left(\frac{\partial v}{\partial z}\right), \tag{6.32}$$

where $\tau_{rz} = \tau_{zr}$ is the stress component in the *r* direction on a unit area perpendicular to the *z* direction, and $\tau_{\theta z} = \tau_{z\theta}$ is the stress component in the θ direction on the same unit area perpendicular to the *z* direction.

We apply the Boussinesq approximation (buoyancy) for the continuity equation, while consider body force by gravity in the momentum equation. Moreover, we neglect the spatiotemporal variation of heat capacity of the liquid. By scaling, the resulting dimensionless equations are derived as eqs. (6.27-6.32), which are governing equations respectively for mass, (*r*, θ, *z*)-momentum, energy, and the general form of the scaled concentration equation.

$$\frac{1}{r}\frac{\partial (ru)}{\partial r} + \frac{1}{r}\frac{\partial v}{\partial \theta} + \frac{\partial w}{\partial z} = 0, \tag{6.33}$$

$$\varepsilon \,\mathrm{Re}\,\rho\left(\frac{\partial u}{\partial t} + u\frac{\partial u}{\partial r} + \frac{v}{r}\frac{\partial u}{\partial \theta} - \frac{v^2}{r} + w\frac{\partial u}{\partial z}\right) = -\frac{\partial p}{\partial r} + \frac{\partial}{\partial z}\left(\mu\frac{\partial u}{\partial z}\right), \tag{6.34}$$

$$\varepsilon \,\mathrm{Re}\,\rho\left(\frac{\partial v}{\partial t} + u\frac{\partial v}{\partial r} + \frac{v}{r}\frac{\partial v}{\partial \theta} + \frac{uv}{r} + w\frac{\partial v}{\partial z}\right) = -\frac{1}{r}\frac{\partial p}{\partial \theta} + \frac{\partial}{\partial z}\left(\mu\frac{\partial v}{\partial z}\right), \tag{6.35}$$

$$\frac{\partial p}{\partial z} = -\mathrm{St}\,\rho g_{\mathrm{G}}, \tag{6.36}$$

$$\varepsilon \,\mathrm{Re}\,\mathrm{Pr}\,\rho c_p\left(\frac{\partial T}{\partial t} + u\frac{\partial T}{\partial r} + \frac{v}{r}\frac{\partial T}{\partial \theta} + w\frac{\partial T}{\partial z}\right) = \frac{\partial}{\partial z}\left(k\frac{\partial T}{\partial z}\right), \tag{6.37}$$

$$\frac{\partial \chi_{\mathrm{H_2O}}}{\partial t}+u\frac{\partial \chi_{\mathrm{H_2O}}}{\partial r}+\frac{v}{r}\frac{\partial \chi_{\mathrm{H_2O}}}{\partial \theta}+w\frac{\partial \chi_{\mathrm{H_2O}}}{\partial z}= \\ \frac{1}{\mathrm{Pe}}\left(\frac{1}{r}\frac{\partial}{\partial r}\left(r\frac{\partial \chi_{\mathrm{H_2O}}}{\partial r}\right)+\frac{1}{r}\frac{\partial}{\partial \theta}\left(\frac{1}{r}\frac{\partial \chi_{\mathrm{H_2O}}}{\partial \theta}\right)+\frac{1}{\varepsilon^2}\frac{\partial^2 \chi_{\mathrm{H_2O}}}{\partial z^2}\right). \tag{6.38}$$

During the scaling process, the dimensionless groups arising include the Reynolds number, defined as, $\mathrm{Re}=\frac{\hat{\rho}_{\mathrm{H_2O}}\hat{u}^*\hat{H}_0}{\hat{\mu}_{\mathrm{H_2O}}}$, the Stokes number, defined as, $\mathrm{St}=\frac{\hat{\rho}_{\mathrm{H_2O}}\hat{g}_{\mathrm{G}}\hat{H}_0^3}{\hat{\mu}_{\mathrm{H_2O}}\hat{u}^*R_0}$, the Prandtl number, defined as, $\mathrm{Pr}=\frac{\hat{\mu}_{\mathrm{H_2O}}\hat{c}_{p,\mathrm{H_2O}}}{\hat{k}_{\mathrm{H_2O}}}$, and the Péclet number, defined as, $\mathrm{Pe}=\frac{\hat{u}^*\hat{R}_0\hat{\rho}_{\mathrm{H_2O}}}{\hat{D}_{\mathrm{H_2O}}}$.

From eq. (6.36), we can derive that,

$$p=-\mathrm{St}\ \rho g_{\mathrm{G}} z+p_0(r,\theta), \tag{6.39}$$

where p_0 is the pressure component of liquid phase in the r and θ direction. Substituting in eq. (6.34) and (6.35), the r-momentum and θ-momentum equations becomes,

$$\varepsilon\,\mathrm{Re}\,\rho\left(\frac{\partial u}{\partial t}+u\frac{\partial u}{\partial r}+\frac{v}{r}\frac{\partial u}{\partial \theta}-\frac{v^2}{r}+w\frac{\partial u}{\partial z}\right)=-\frac{\partial p_0}{\partial r}+\frac{\partial}{\partial z}\left(\mu\frac{\partial u}{\partial z}\right), \tag{6.40}$$

$$\varepsilon\,\mathrm{Re}\,\rho\left(\frac{\partial v}{\partial t}+u\frac{\partial v}{\partial r}+\frac{v}{r}\frac{\partial v}{\partial \theta}+\frac{uv}{r}+w\frac{\partial v}{\partial z}\right)=-\frac{1}{r}\frac{\partial p_0}{\partial \theta}+\frac{\partial}{\partial z}\left(\mu\frac{\partial v}{\partial z}\right). \tag{6.41}$$

The 3D dimensionless concentration equation (eq. (6.38)) can be further simplified by applying either the rapid vertical diffusion approximation or the limit of weak diffusion, and the derivations are given in section 6.4.2.

6.4.2. Simplification of the concentration equation

The Péclet number, Pe, is a measurement of advective transport rate to the diffusive transport rate. The rapid vertical diffusion approximation assumes that the solute diffusion within the droplet happens rapidly in the vertical z direction with a dimensionless time scale of $O(\varepsilon^2\mathrm{Pe})$. For the rapid diffusion approximation, the concentration distribution of water inside the LiBr-H_2O droplet can be expressed by a mean concentration independent

of z plus a rapidly diffusing component shown as eq. (6.42).

$$\chi_{\mathrm{H_2O}}(r,\theta,z,t)=\chi_{\mathrm{H_2O},0}(r,\theta,t)+\varepsilon^2\mathrm{Pe}\chi_{\mathrm{H_2O},1}(r,\theta,z,t), \tag{6.42}$$

where $\chi_{\mathrm{H_2O},0}(r,\theta,t)$ represents the averaged mass fraction of water within the LiBr-H_2O droplet independent of z, while $\chi_{\mathrm{H_2O},1}(r,\theta,z,t)$ represents a small perturbation accounting for z dependence, assuming that $\varepsilon^2\mathrm{Pe} \ll 1$. Substituting eq. (6.42) in to eq. (6.38), the concentration equation for rapid diffusion approximation is obtained,

$$\begin{aligned}&\frac{\partial\chi_{\mathrm{H_2O},0}}{\partial t}+u\frac{\partial\chi_{\mathrm{H_2O},0}}{\partial r}+\frac{v}{r}\frac{\partial\chi_{\mathrm{H_2O},0}}{\partial\theta}=\\&\frac{1}{\mathrm{Pe}}\left(\frac{1}{r}\frac{\partial}{\partial r}\left(r\frac{\partial\chi_{\mathrm{H_2O},0}}{\partial r}\right)+\frac{1}{r}\frac{\partial}{\partial\theta}\left(\frac{1}{r}\frac{\partial\chi_{\mathrm{H_2O},0}}{\partial\theta}\right)\right)+\frac{\partial^2\chi_{\mathrm{H_2O},1}}{\partial z^2}\end{aligned}. \tag{6.43}$$

For the weak diffusion approximation, $\mathrm{Pe} \approx O(\varepsilon^{-2})$, firstly we simplify the concentration equation by substituting $\mathrm{Pe} \approx \varepsilon^{-2}\mathrm{Pe}'$ into eq. (6.38), where Pe′ is a modified form of Pe, and is in the order of $O(1)$, By eliminating the terms multiplied by ε^2, the following concentration equation for weak diffusion is derived,

$$\frac{\partial\chi_{\mathrm{H_2O}}}{\partial t}+u\frac{\partial\chi_{\mathrm{H_2O}}}{\partial r}+\frac{v}{r}\frac{\partial\chi_{\mathrm{H_2O}}}{\partial\theta}+w\frac{\partial\chi_{\mathrm{H_2O}}}{\partial z}=\frac{1}{\mathrm{Pe}'}\left(\frac{\partial^2\chi_{\mathrm{H_2O}}}{\partial z^2}\right). \tag{6.44}$$

Then we apply an approximate Galerkin equation for $\chi_{\mathrm{H_2O}}$, and assume that $\chi_{\mathrm{H_2O}}$ can be expressed in the following form,

$$\chi_{\mathrm{H_2O}}(r,\theta,z,t)=\chi_{\mathrm{H_2O},0}(r,\theta,t)+\chi_{\mathrm{H_2O},2}(r,\theta,t)\left(\frac{z^2}{h^2}-\frac{1}{3}\right), \tag{6.45}$$

where the first term in the RHS represents the averaged mass fraction of water independent of z, and the second term containing $\chi_{\mathrm{H_2O},2}$ represents a zero-mean quadratic fluctuating component. Substituting eq. (6.45) in to eq. (6.44), the final form of the concentration equation for weak diffusion approximation is obtained,

$$\begin{aligned}&\frac{\partial\chi_{\mathrm{H_2O},0}}{\partial t}+u\frac{\partial\chi_{\mathrm{H_2O},0}}{\partial r}+\frac{v}{r}\frac{\partial\chi_{\mathrm{H_2O},0}}{\partial\theta}+\left(\frac{\partial\chi_{\mathrm{H_2O},2}}{\partial t}+u\frac{\partial\chi_{\mathrm{H_2O},2}}{\partial r}+\frac{v}{r}\frac{\partial\chi_{\mathrm{H_2O},2}}{\partial\theta}\right)\left(\frac{z^2}{h^2}-\frac{1}{3}\right)\\&=\frac{1}{\mathrm{Pe}'}\frac{\partial^2\chi_{\mathrm{H_2O}}}{\partial z^2}\end{aligned}. \tag{6.46}$$

6.4.3. Boundary conditions in z

In the modeling, we focus on the liquid side, and two interfacial boundaries are taken into account: the liquid-solid interface, $z = 0$, and the liquid-vapor interface, $z = h(r, t)$.

At the liquid-vapor interface, the outward unit vector normal to the interface, $\boldsymbol{n}$, and the outward unit vectors tangential to the interface in r direction, $\boldsymbol{t}_r$, and in θ direction, $\boldsymbol{t}_\theta$, are defined and scaled as,

$$\boldsymbol{n} = \frac{-\hat{r}\frac{\partial \hat{h}}{\partial \hat{r}}\boldsymbol{e}_r - \frac{\partial \hat{h}}{\partial \theta}\boldsymbol{e}_\theta + \hat{r}\boldsymbol{e}_z}{\sqrt{\hat{r}^2\left(\frac{\partial \hat{h}}{\partial \hat{r}}\right)^2 + \left(\frac{\partial \hat{h}}{\partial \theta}\right)^2 + \hat{r}^2}} = \frac{-\varepsilon r\frac{\partial h}{\partial r}\boldsymbol{e}_r - \varepsilon\frac{\partial h}{\partial \theta}\boldsymbol{e}_\theta + r\boldsymbol{e}_z}{\sqrt{\varepsilon^2 r^2\left(\frac{\partial h}{\partial r}\right)^2 + \varepsilon^2\left(\frac{\partial h}{\partial \theta}\right)^2 + r^2}}, \tag{6.47}$$

$$\boldsymbol{t}_r = \frac{\boldsymbol{e}_r + \frac{\partial \hat{h}}{\partial \hat{r}}\boldsymbol{e}_z}{\sqrt{1+\left(\frac{\partial \hat{h}}{\partial \hat{r}}\right)^2}} = \frac{\boldsymbol{e}_r + \varepsilon\frac{\partial h}{\partial r}\boldsymbol{e}_z}{\sqrt{1+\varepsilon^2\left(\frac{\partial h}{\partial r}\right)^2}}, \tag{6.48}$$

$$\boldsymbol{t}_\theta = \frac{\hat{r}\boldsymbol{e}_\theta + \frac{\partial \hat{h}}{\partial \theta}\boldsymbol{e}_z}{\sqrt{\hat{r}^2+\left(\frac{\partial \hat{h}}{\partial \theta}\right)^2}} = \frac{r\boldsymbol{e}_\theta + \varepsilon\frac{\partial h}{\partial \theta}\boldsymbol{e}_z}{\sqrt{r^2+\varepsilon^2\left(\frac{\partial h}{\partial \theta}\right)^2}}, \tag{6.49}$$

where $\boldsymbol{e}_r$, $\boldsymbol{e}_\theta$, and $\boldsymbol{e}_z$ are the unit vector in the r, θ, and z direction respectively. Substituting eqs. (6.47-49) into eq. (6.14) and scaling yield the dimensionless absorptive mass flux boundary condition.

$$\frac{EJ}{\rho} = -(u-u_s)\frac{\partial h}{\partial r} - (v-v_s)\frac{1}{r}\frac{\partial h}{\partial \theta} + (w-w_s), \tag{6.50}$$

where E is the dimensionless evaporation/absorption number, $E = \frac{\hat{D}_{H_2O}\hat{R}_0\Delta\chi_{H_2O}}{\hat{H}_0^2\hat{u}^*}$.

Moreover, by assuming that $k_v \ll k$, and applying $\varepsilon \ll 1$, the dimensionless jump energy balance can be obtained,

$$J + k\frac{\partial T}{\partial z} = 0. \tag{6.51}$$

From eq. (6.23), the dimensionless kinematic boundary condition at the liquid-air interface is derived as,

$$\frac{\partial h}{\partial t}+u_s\frac{\partial h}{\partial r}+\frac{v_s}{r}\frac{\partial h}{\partial \theta}=w_s. \tag{6.52}$$

Substituting eq. (6.52) into eq. (6.50) yields the dimensionless form of the kinematic boundary condition,

$$\frac{\partial h}{\partial t}+u\frac{\partial h}{\partial r}+\frac{v}{r}\frac{\partial h}{\partial \theta}-w+\frac{EJ}{\rho}=0. \tag{6.53}$$

Next, we consider the normal stress boundary balance with a dimensional form of eq. (6.18). For the assumption of infinitesimal aspect ratio, $\varepsilon \ll 1$, the droplet liquid-vapor interface is close to flat, therefore,

$$\boldsymbol{n}\cdot\boldsymbol{\tau}\cdot\boldsymbol{n}=0. \tag{6.54}$$

Additionally, by applying the expression of $2\hat{\kappa}$, eq. (6.55), the expression of liquid pressure, *p*, eq. (6.39), and scaling, the dimensionless normal stress boundary balance is derived as eq. (6.56).

$$2\hat{\kappa}=-\hat{\nabla}_s\cdot\boldsymbol{n}=\frac{\hat{H}_0}{\hat{R}_0^2}\left(\frac{1}{r}\frac{\partial}{\partial r}\left(r\frac{\partial h}{\partial r}\right)+\frac{1}{r^2}\frac{\partial^2 h}{\partial \theta^2}\right), \tag{6.55}$$

$$p_0=-\frac{\varepsilon^2\sigma}{\mathrm{Ma}}\left(\frac{1}{r}\frac{\partial}{\partial r}\left(r\frac{\partial h}{\partial r}\right)+\frac{1}{r^2}\frac{\partial^2 h}{\partial \theta^2}\right)-\frac{\mathcal{A}}{h^3}+\mathrm{St}\rho g_G h, \tag{6.56}$$

where Ma is the dimensionless solutal Marangoni number, $\mathrm{Ma}=\dfrac{\hat{\mu}_{\mathrm{H_2O}}\hat{u}^*}{\varepsilon\hat{\sigma}_{\mathrm{H_2O}}}=\dfrac{\hat{\eta}_\sigma\Delta\chi_{\mathrm{H_2O}}}{\hat{\sigma}_{\mathrm{H_2O}}}$, $\mathcal{A}$ is the dimensionless Hamaker constant, expressed as $\mathcal{A}=\dfrac{\hat{\mathcal{A}}}{6\pi\hat{\mu}_{\mathrm{H_2O}}\hat{u}^*\hat{R}_0\hat{H}_0}$.

The dimensionless form of tangential stress boundary balance yields,

$$\tau_{zr}=\frac{1}{\mathrm{Ma}}\frac{\partial\sigma}{\partial r},\qquad \tau_{z\theta}=\frac{1}{\mathrm{Ma}}\frac{\partial\sigma}{\partial\theta}. \tag{6.57}$$

Now, we derive the dimensionless form of the concentration balance of water vapor over the interface (eq. (6.22) gives the dimensional form). Firstly, the concentration gradient within the droplet can be expressed as eq. (6.58).

$$\hat{\nabla}\chi_{\mathrm{H_2O}}=\frac{\partial\chi_{\mathrm{H_2O}}}{\partial\hat{r}}\boldsymbol{e}_r+\frac{1}{\hat{r}}\frac{\partial\chi_{\mathrm{H_2O}}}{\partial\theta}\boldsymbol{e}_\theta+\frac{\partial\chi_{\mathrm{H_2O}}}{\partial\hat{z}}\boldsymbol{e}_z. \tag{6.58}$$

By substituting the expressions of $\hat{\nabla}\chi_{\mathrm{H_2O}}$ and $\boldsymbol{n}$ into eq. (6.22), applying the

assumption of $\varepsilon^2 \ll 1$, and scaling, the dimensionless form of the concentration balance boundary condition is obtained,

$$\frac{1}{\mathrm{Pe}}\left(-\frac{\partial h}{\partial r}\frac{\partial \chi_{\mathrm{H_2O}}}{\partial r}-\frac{1}{r^2}\frac{\partial h}{\partial \theta}\frac{\partial \chi_{\mathrm{H_2O}}}{\partial \theta}+\frac{1}{\varepsilon^2}\frac{\partial \chi_{\mathrm{H_2O}}}{\partial z}\right)_{z=h}=EJ\left(\chi_{\mathrm{H_2O}}-1\right). \tag{6.59}$$

For rapid vertical diffusion approximation, the dimensionless concentration balance boundary condition is derived as,

$$\frac{1}{\mathrm{Pe}}\left(-\frac{\partial h}{\partial r}\frac{\partial \chi_{\mathrm{H_2O},0}}{\partial r}-\frac{1}{r^2}\frac{\partial h}{\partial \theta}\frac{\partial \chi_{\mathrm{H_2O},0}}{\partial \theta}\right)_{z=h}+\left(\frac{\partial \chi_{\mathrm{H_2O},1}}{\partial z}\right)_{z=h}=EJ\left(\chi_{\mathrm{H_2O},0}-1\right). \tag{6.60}$$

For weak vertical diffusion approximation, the dimensionless concentration balance boundary condition is derived as,

$$\frac{1}{\mathrm{Pe}'}\left(\frac{\partial \chi_{\mathrm{H_2O}}}{\partial z}\right)_{z=h}=\frac{2}{\mathrm{Pe}'h}\chi_{\mathrm{H_2O},2}=\frac{EJ\left(\chi_{\mathrm{H_2O},0}-1\right)}{1-\dfrac{EJ\mathrm{Pe}'h}{3}}. \tag{6.61}$$

By scaling from eq. (6.28), the dimensional form of the mass flux of water vapor at the droplet interface is obtained,

$$\mathrm{Kn}\cdot J=\chi_{\mathrm{H_2O}}\left(\delta\left(p_0-\mathrm{St}\rho g_G h\right)+\vartheta\left(T_{\mathrm{S}}-T_g\right)+\ln\left(\frac{\chi_{\mathrm{H_2O}}}{\chi_{\mathrm{H_2O,g}}}\right)\right), \tag{6.62}$$

where $\delta=\dfrac{\hat{M}_{\mathrm{H_2O}}\hat{\mu}_{\mathrm{H_2O}}\hat{u}^*\hat{R}_0}{\hat{\rho}_{\mathrm{H_2O}}\hat{R}_g\hat{T}_{\mathrm{g}}\hat{H}_0^2}$, $\vartheta=\dfrac{\hat{M}_{\mathrm{H_2O}}\hat{L}_{\mathrm{H_2O}}\Delta\hat{T}}{\hat{R}_g\hat{T}_{\mathrm{g}}^2}$, and Kn is the dimensionless Knudsen number, defined as, $\mathrm{Kn}=\dfrac{\hat{\rho}_{\mathrm{H_2O}}\hat{D}_{\mathrm{H_2O}}\Delta\chi_{\mathrm{H_2O}}}{\hat{H}_0\hat{p}_{\mathrm{v,sat}}}\sqrt{\dfrac{2\pi\hat{R}_g\hat{T}_{\mathrm{g}}}{\hat{M}_{\mathrm{H_2O}}}}$.

Along the liquid-solid interface, $\hat{z}=0$, the dimensionless forms of the no-slip and zero vertical concentration flux boundary conditions are derived as,

$$u=0,\qquad w=0,\qquad \frac{\partial \chi_{\mathrm{H_2O}}}{\partial z}=\frac{\partial \chi_{\mathrm{H_2O},1}}{\partial z}=0,\qquad T=T_{\mathrm{w}}. \tag{6.63}$$

In summary, in the scaling process, the solutal capillary velocity and the thermophysical properties of pure water are considered to scale the governing equations and boundary conditions. The dimensionless numbers arising during the scaling process include,

$$\varepsilon=\frac{\hat{H}_0}{\hat{R}_0},\qquad \mathrm{Re}=\frac{\hat{\rho}_{\mathrm{H_2O}}\hat{u}^*\hat{H}_0}{\hat{\mu}_{\mathrm{H_2O}}},\qquad \mathrm{Pe}=\frac{\hat{u}^*\hat{R}_0\hat{\rho}_{\mathrm{H_2O}}}{\hat{D}_{\mathrm{H_2O}}},$$

$$\delta=\frac{\hat{\mu}_{\mathrm{H_2O}}\hat{u}^*\hat{R}_0\hat{M}_{\mathrm{H_2O}}}{\hat{H}_0^2\hat{\rho}_{\mathrm{H_2O}}\hat{R}_g\hat{T}_g},\quad \mathrm{St}=\frac{\hat{\rho}_{\mathrm{H_2O}}\hat{g}\hat{H}_0^3}{\hat{\mu}_{\mathrm{H_2O}}\hat{u}^*\hat{R}_0},\qquad \mathrm{Pr}=\frac{\hat{\mu}_{\mathrm{H_2O}}\hat{c}_{p,\mathrm{H_2O}}}{\hat{k}_{\mathrm{H_2O}}},$$

$$E=\frac{\hat{D}_{\mathrm{H_2O}}\hat{R}_0\Delta\chi_{\mathrm{H_2O}}}{\hat{H}_0^2\hat{u}^*},\quad \vartheta=\frac{\hat{M}_{\mathrm{H_2O}}\hat{L}_{\mathrm{H_2O}}\Delta\hat{T}}{\hat{R}_g\hat{T}_{\mathrm{g}}^2},\qquad \mathrm{Ma}=\frac{\hat{\eta}_\sigma\Delta\chi_{\mathrm{H_2O}}}{\hat{\sigma}_{\mathrm{H_2O}}},\tag{6.66}$$

$$\mathcal{A}=\frac{\hat{\mathcal{A}}}{6\pi\hat{\mu}_{\mathrm{H_2O}}\hat{u}^*\hat{R}_0\hat{H}_0},\qquad \mathrm{Kn}=\frac{\hat{\rho}_{\mathrm{H_2O}}\hat{D}_{\mathrm{H_2O}}\Delta\chi_{\mathrm{H_2O}}}{\hat{H}_0\hat{p}_{\mathrm{v,sat}}}\left(\frac{2\pi\hat{R}_g\hat{T}_g}{\hat{M}_{\mathrm{H_2O}}}\right)^{1/2}.$$

The basic parameters used for calculating dimensionless numbers are summarized in Table 6.3, and the calculation results of the dimensionless numbers are listed in Table 6.4.

Table 6.3 Basic parameters used for dimensionless number calculation.

$\hat{H}_0$ (m)	$\hat{R}_0$ (m)	$\hat{\rho}_{\mathrm{H_2O}}$ (kg/m^3)	$\hat{\mu}_{\mathrm{H_2O}}$ (Pa·s)	$\Delta\chi_{\mathrm{H_2O}}$	$\hat{\eta}_\sigma$ (N/m)
3.0×10^{-4}	1.5×10^{-3}	9.98×10^{2}	1.005×10^{-3}	0.54	4.44×10^{-2}
$\hat{D}_{\mathrm{H_2O}}$ (m^2/s)	$\hat{c}_{p,\mathrm{H_2O}}$ (J/kg/K)	$\hat{k}_{\mathrm{H_2O}}$ (W/m/K)	$\hat{\sigma}_{\mathrm{H_2O}}$ (N/m)	$\hat{M}_{\mathrm{H_2O}}$ (kg/mol)	$\hat{R}_g$ (J/mol/K)
1.2×10^{-9}	4.180×10^{3}	0.5984	7.275×10^{-2}	1.8×10^{-2}	8.314
$\hat{T}_g$ (K)	$\hat{p}_{\mathrm{v,sat}}$ (Pa)	$\hat{u}^*$ (m/s)	$\hat{\mathcal{A}}$ (J)[170]	$\hat{L}_{\mathrm{H_2O}}$ (J/kg)	ΔT (K)
293.15	2.3×10^{3}	4.77	3.69×10^{-20}	2.257×10^{6}	2.441

Table 6.4 Summary of the dimensionless numbers. ε: aspect ratio; Re: Renolds number; Pe: Péclet number; St: Stokes number; Pr: Prandtl number; E: Evaporation/absorption number; Ma: Marangoni number; A: Dimensionless Hamaker number; δ: Dimensionless number accounting for the effect of van der waals force on the film thickness; Kn: Knudsen number.

ε	Re	Pe	St	Pr	E
0.2	1.42×10^{3}	5.96×10^{9}	0.0368	7.02	2.26×10^{-6}
Ma	A	δ	Kn	ϑ	Ma
0.33	9.06×10^{-13}	5.92×10^{-7}	8.64×10^{-4}	0.139	0.33

6.4.4. Precursor film

In the model, a precursor layer is assumed to exist in front of the triple contact line,

which removes the stress singularity that may arise at the corner of moving contact line. We assume that there is no mean curvature in the precursor region, and the thin film is in an isothermal equilibrium with the wall, the interfacial temperature of precursor film thus equals to the temperature of the solid wall, $\hat{T}_S = \hat{T}_W$. Applying all the assumptions to eq. (6.62) and combining the normal stress boundary condition, we arrive at,

$$\frac{\mathcal{A}\delta}{h_\infty^3} = \mathcal{G}\left(T_W - T_g\right) + \ln\left(\frac{\chi_{H_2O,precursor}}{\chi_{H_2O,g}}\right), \tag{6.64}$$

where $\mathcal{A}$ is the dimensionless Hamaker constant, $\mathcal{A} = \dfrac{\hat{A}}{6\pi\hat{\mu}_{H_2O}\hat{u}^*\hat{R}_0\hat{H}_0}$, and $\chi_{H_2O,g}$ is the water concentration of LiBr-H_2O solution in equilibrium with the vapor phase.

Assuming the LiBr-H_2O mixture as ideal solution and applying the Raoult's law at the liquid-air interface, we have $\chi_{H_2O,g}\hat{p}_{v,sat} = \hat{p}_{v,sat}RH$, $\chi_{H_2O,g} = RH$, where RH is the relative humidity of the air bulk, indicating the degree of saturation of humid air.

The height of the precursor film, h_∞, can be therefore calculated as,

$$h_\infty = \sqrt[3]{\mathcal{A}\delta \Big/ \left(\mathcal{G}\left(T_W - T_g\right) + \ln\left(\frac{\chi_{H_2O,precursor}}{RH}\right)\right)}, \tag{6.65}$$

In the simulation, we assume that the initial water vapor concentration within the precursor film is the same with the droplet bulk, $\chi_{H_2O,precursor} = \chi_{H_2O,bulk}$. The assumption ensues the continuity of mass flux from the droplet bulk to the precursor layer across the contact line. After getting contact with the humid air, the absorption of water vapor happens both across the droplet surface and at the precursor film. Since the precursor film is very thin, the precursor layer gets saturated and reaches an equilibrium with the gas phase very quickly.

6.4. Kármán-Pohlhausen approximation

The Kármán-Pohlhausen integral method is a typical approach for solving the boundary layer problems. The method integrates the governing equations in the z

direction from $z = 0$ to $z = h$. Instead of accurately satisfying the governing equations at every mesh points, the Kármán-Pohlhausen approximation satisfies the governing equations on the average across the z direction. By doing this, the multiple variable differentials are removed while the inertia and advection terms in the momentum and energy balance equations still remain.

Firstly, we define the integration forms of u, v, and T over z axis as,

$$f = \int_0^h u dz\,, \qquad g = \int_0^h v dz\,, \qquad \Theta = \int_0^h T dz\,. \tag{6.67}$$

By integrating over z, and applying the dimensionless form of kinematic boundary condition, the integral forms of continuity equation, eq. (6.33), r-momentum equation, eq. (6.40), θ-momentum equation, eq. (6.41), and energy equation, eq. (6.37), are derived as,

$$\frac{\partial h}{\partial t} = -\frac{EJ}{\rho} - \frac{1}{r}\frac{\partial (rf)}{\partial r} - \frac{1}{r}\frac{\partial g}{\partial \theta}\,, \tag{6.68}$$

$$\begin{aligned} &\varepsilon \,\mathrm{Re}\,\rho\left(\frac{\partial f}{\partial t} + \frac{1}{r}\frac{\partial}{\partial r}\left(r\int_0^h u^2 dz\right) + \frac{1}{r}\frac{\partial}{\partial \theta}\left(\int_0^h uv dz\right) - \frac{1}{r}\int_0^h v^2 dz + u\big|_h \frac{EJ}{\rho}\right) \\ &= -h\frac{\partial p_0}{\partial r} + \left[\mu\frac{\partial u}{\partial z}\right]_0^h \end{aligned}\,, \tag{6.69}$$

$$\begin{aligned} &\varepsilon \,\mathrm{Re}\,\rho\left(\frac{\partial g}{\partial t} + \frac{1}{r}\frac{\partial}{\partial r}\left(r\int_0^h uv dz\right) + \frac{1}{r}\frac{\partial}{\partial \theta}\left(\int_0^h v^2 dz\right) + \frac{1}{r}\int_0^h uv dz + v\big|_h \frac{EJ}{\rho}\right) \\ &= -\frac{h}{r}\frac{\partial p_0}{\partial \theta} + \left[\mu\frac{\partial v}{\partial z}\right]_0^h \end{aligned}\,, \tag{6.70}$$

$$\varepsilon \,\mathrm{Re}\,\mathrm{Pr}\,\rho c_p\left(\frac{\partial \Theta}{\partial t} + \frac{1}{r}\frac{\partial}{\partial r}\left(r\int_0^h uT dz\right) + \frac{1}{r}\frac{\partial}{\partial \theta}\left(\int_0^h vT dz\right) + T\big|_h \frac{EJ}{\rho}\right) = \left[k\frac{\partial T}{\partial z}\right]_0^h. \tag{6.71}$$

By applying the dimensionless concentration balance boundary condition, eq. (6.60) and eq. (6.61), and integrating, the concentration equation is derived as eq. (6.72) and eq. (6.73) for rapid diffusion approximation and for weak diffusion approximation, respectively.

$$\begin{aligned} h\frac{\partial \chi_{\mathrm{H_2O},0}}{\partial t} + f\frac{\partial \chi_{\mathrm{H_2O},0}}{\partial r} + \frac{g}{r}\frac{\partial \chi_{\mathrm{H_2O},0}}{\partial \theta} = &\frac{1}{r\mathrm{Pe}}\left(\frac{\partial}{\partial r}\left(hr\frac{\partial \chi_{\mathrm{H_2O},0}}{\partial r}\right) + \frac{\partial}{\partial \theta}\left(\frac{h}{r}\frac{\partial \chi_{\mathrm{H_2O},0}}{\partial \theta}\right)\right), \\ &+ EJ\left(\chi_{\mathrm{H_2O},0} - 1\right) \end{aligned} \tag{6.72}$$

$$h\frac{\partial \chi_{\mathrm{H_2O},0}}{\partial t}+f\frac{\partial \chi_{\mathrm{H_2O},0}}{\partial r}+\frac{g}{r}\frac{\partial \chi_{\mathrm{H_2O},0}}{\partial \theta}=\frac{EJ\left(\chi_{\mathrm{H_2O},0}-1\right)}{1-\dfrac{EJ\mathrm{Pe}'h}{3}}. \tag{6.73}$$

Finally, we need to derive specific expressions for $u\big|_h$, $\left[\frac{\partial u}{\partial z}\right]_0^h$, $\int_0^h u^2dz$, $v\big|_h$, $\left[\frac{\partial v}{\partial z}\right]_0^h$, $\int_0^h v^2dz$, $\int_0^h uvdz$, $T\big|_h$, $\left[\frac{\partial T}{\partial z}\right]_0^h$, and $\int_0^h uTdz$ in the governing equations. We assume that the variables, *u, v, T*, all follows the form of $c_3+c_2z+c_1z^2$. By applying the boundary conditions at $z = 0$ and $z = h$, the expressions of *u*, *v*, and *T* arise as,

$$u=\left(\frac{3f}{h^2}-\frac{1}{2\mu\mathrm{Ma}}\frac{\partial\sigma}{\partial r}\right)z+\left(\frac{3}{4\mu h\mathrm{Ma}}\frac{\partial\sigma}{\partial r}-\frac{3f}{2h^3}\right)z^2, \tag{6.74}$$

$$v=\left(\frac{3g}{h^2}-\frac{1}{2\mu r\mathrm{Ma}}\frac{\partial\sigma}{\partial \theta}\right)z+\left(\frac{3}{4\mu rh\mathrm{Ma}}\frac{\partial\sigma}{\partial \theta}-\frac{3g}{2h^3}\right)z^2, \tag{6.75}$$

$$T=T_{\mathrm{w}}+\left(\frac{3\Theta}{h^2}-\frac{3T_{\mathrm{w}}}{h}+\frac{J}{2k}\right)z+\left(\frac{3T_{\mathrm{w}}}{2h^2}-\frac{3\Theta}{2h^3}-\frac{3J}{4kh}\right)z^2, \tag{6.76}$$

where $\frac{\partial\sigma}{\partial r}=\eta_\sigma\frac{\partial\chi_{\mathrm{H_2O}}\big|_h}{\partial r}+\zeta_\sigma\frac{\partial T\big|_h}{\partial r}$, $\frac{\partial\sigma}{\partial\theta}=\eta_\sigma\frac{\partial\chi_{\mathrm{H_2O}}\big|_h}{\partial\theta}+\zeta_\sigma\frac{\partial T\big|_h}{\partial\theta}$. By substituting eqs. (6.72-76) into eqs. (6.68-73), the integral forms of the governing equations are obtained, with seven independent variables, h, p_0, u, v, T, $\chi_{\mathrm{H_2O}}$, and J.

6.5. Initial and boundary conditions in r

As a first step toward understanding the droplet dynamics during vapor absorption, we start from a one dimensional model, which focuses on only the *r* direction, disregarding the parameter variations in the azimuthal θ direction. The one-dimension model is sufficient for analyzing the inner flow within the droplet, and subsequently the droplet kinetics induced by Marangoni effect, etc. For modelling, the governing equations derived in the above analysis are further constraint in the *r* direction, and all the terms

derived in θ direction are set as zero. In the one dimensional model, the droplet height is dealt as a dependent variable of r, which can be solved according to the kinematic boundary condition and the continuity equation. Therefore, we only need to construct a one-dimension mesh along the r-direction, and the governing equations are solved along with the initial conditions and the boundary conditions in the r direction.

In the region of droplet bulk, $0 \le r \le 1$, the initial conditions of h, f, Θ, and χ_{H_2O} are as follows,

$$h(r,0) = h_\infty + 1 - r^2, \quad f(r,0) = 0, \quad \Theta(r,0) = h(r,0)T_g, \quad \chi_{H_2O}(r,0) = 0.40 \sim 1.00. \tag{6.77}$$

In the region of precursor layer, $r > 1$, the initial conditions are,

$$h(r,0) = h_\infty, \quad f(r,0) = 0, \quad \Theta(r,0) = h_\infty T_W, \quad \chi_{H_2O}(r,0) = \chi_{H_2O}(0 \sim 1, 0). \tag{6.78}$$

The initial concentration of water in the aqueous solution is set as 40~100 wt. % (x_{LiBr} = 0~60 wt.%). At room temperature, 20~30 °C, the crystallization concentration of LiBr in LiBr-H_2O solution, $\chi_{LiBr} = 1 - \chi_{H_2O}$, is *ca.* 65 wt.%.

The parameters at the droplet center, $r = 0$, satisfy the symmetric boundary conditions, shown as,

$$\frac{\partial h}{\partial r}(0,t) = 0, \quad f(0,t) = 0, \quad \frac{\partial \Theta}{\partial r}(0,t) = 0, \quad \frac{\partial \chi_{H_2O}}{\partial r}(0,t) = 0. \tag{6.79}$$

At the periphery of the solution domain, $r = r_\infty$, where r_∞ is the length of the domain, the boundary conditions are defined as,

$$h(r_\infty,t) = h_\infty, \quad \frac{\partial h}{\partial r}(r_\infty,t) = 0, \quad f(r_\infty,t) = 0, \quad \Theta(r_\infty,t) = h_\infty T_W, \quad \frac{\partial \chi_{H_2O}}{\partial r}(r_\infty,t) = 0. \tag{6.80}$$

6.6. Galerkin method and solution algorithm

After the above derivations, now we have four governing equations for the 1-D model: continuity equation, eq. (6.68), r-momentum equation, eq. (6.69), energy equation, eq.

(6.71), and advection diffusion equation, eq. (6.72) or eq. (6.73). At the liquid-air interface, the normal stress balance, eq. (6.56), and the absorptive mass flux, eq. (6.62), are derived. The six independent equations with six independent variables, h, p_0, u, T, χ_{H_2O}, and J, can be then solved using finite element method (FEM).

Along the r direction, we construct a uniform one-dimension mesh, and discretize the system of partial differential equations into an algebraic problem of solving the parameters at each node. The solutions to the system of equations are then obtained using the Newton-Raphson method. At each fixed point of time, the solutions are iterated progressively into more accurate values until satisfying the convergence precision. In the time domain, the solution at each moment is evolved based on the solution of the last moment by forward Euler method.

For the discretization process, we apply the Galerkin method of weighted residuals. By applying the weighted residual to the integral forms of the governing equations and simplifying, we arrive at the final Galerkin weak forms of the governing equations for one-dimensional model.

$$R=\int\left(\frac{\partial h}{\partial t}\phi_i+\frac{EJ}{\rho}\phi_i-f\frac{\partial\phi_i}{\partial r}\right)rdr+\left(rf\phi_i\right)_{r=0}^{r=r_\infty}, \tag{6.82}$$

$$\begin{aligned}R=&\int\left\{\varepsilon\,\mathrm{Re}\,\rho\left[\frac{\partial f}{\partial t}\phi_i+u\big|_h\frac{EJ}{\rho}\phi_i-\left(\int_0^h u^2dz\right)\frac{\partial\phi_i}{\partial r}\right]+h\frac{\partial p_0}{\partial r}\phi_i-\left(\mu\frac{\partial u}{\partial z}\right)_0^h\phi_i\right\}rdr\\&+\left[\varepsilon\,\mathrm{Re}\,\rho\left(r\int_0^h u^2dz\right)\phi_i\right]_{r=0}^{r=r_\infty}\end{aligned}, \tag{6.83}$$

$$\begin{aligned}R=&\int\left[\varepsilon\,\mathrm{Re}\,\mathrm{Pr}\,\rho c_p\left(\frac{\partial\Theta}{\partial t}\phi_i+T\big|_h\frac{EJ}{\rho}\phi_i-\left(\int_0^h uTdz\right)\frac{\partial\phi_i}{\partial r}\right)-\left(k\frac{\partial T}{\partial z}\right)_0^h\phi_i\right]rdr\\&+\left[\varepsilon\,\mathrm{Re}\,\mathrm{Pr}\,\rho c_p\left(r\int_0^h uTdz\right)\phi_i\right]_{r=0}^{r=r_\infty}\end{aligned}, \tag{6.84}$$

$$\begin{aligned}R=&\int\left[h\frac{\partial\chi_{H_2O,0}}{\partial t}\phi_i+f\frac{\partial\chi_{H_2O,0}}{\partial r}\phi_i-EJ\left(\chi_{H_2O,0}-1\right)\phi_i+\frac{h}{\mathrm{Pe}}\frac{\partial\chi_{H_2O,0}}{\partial r}\frac{\partial\phi_i}{\partial r}\right]rdr\\&-\frac{1}{\mathrm{Pe}}\left(rh\frac{\partial\chi_{H_2O,0}}{\partial r}\phi_i\right)_{r=0}^{r=r_\infty}\end{aligned}, \tag{6.85}$$

$$R=\int\left(h\frac{\partial\chi_{\mathrm{H_2O},0}}{\partial t}\phi_i+f\frac{\partial\chi_{\mathrm{H_2O},0}}{\partial r}\phi_i-\frac{EJ\left(\chi_{\mathrm{H_2O},0}-1\right)}{1-\dfrac{EJ\mathrm{Pe'}h}{3}}\phi_i\right)rdr\,, \tag{6.86}$$

$$R=\int\left[\left(p_0-\mathrm{St}\rho g_{\mathrm{G}}h+\frac{\mathcal{A}}{h^3}\right)\frac{\mathrm{Ma}}{\varepsilon^2\sigma}\phi_i-\frac{\partial h}{\partial r}\frac{\partial\phi_i}{\partial r}\right]rdr+\left(r\frac{\partial h}{\partial r}\phi_i\right)_{r=0}^{r=r_\infty}, \tag{6.87}$$

$$R=\int\left(\mathrm{Kn}\cdot J-\chi_{\mathrm{H_2O}}\left(\delta\left(p_0-\mathrm{St}\rho g_{\mathrm{G}}h\right)+\vartheta\left(T_{\mathrm{S}}-T_g\right)+\ln\left(\frac{\chi_{\mathrm{H_2O}}}{\mathrm{RH}}\right)\right)\right)\phi_i rdr\,. \tag{6.88}$$

6.7. Summary

In this chapter, we develop a lubrication-type model to describe the physical mechanisms governing the heat transport, mass diffusion, and fluid dynamics during vapor absorption into hygroscopic aqueous solution droplets. We consider a thin axisymmetric droplet on a hydrophilic substrate which is initially in a thermal equilibrium state. A precursor film is assumed to exist in front of the contact line, which permits the free motion of the contact line and also releases the singularity near the contact line. We take the solutal capillary velocity as the characteristic velocity of the system, and apply a weak diffusion approximation to derive the concentration distribution within the droplet. The absorptive mass flux is approximated combining the Hertz-Knusen equation and the thermodynamic equilibrium relationships across the aqueous solution-air interface. For the discretization process, we apply the Galerkin method of weighted residuals, and arrive at six independent equations with six independent variables, h, p_0, u, T, $\chi_{\mathrm{H_2O}}$, and J. The equation system is then solved using finite element method (FEM), and the temporal variation of the parameters is derived with forward Euler method.

Chapter 7 Simulation results

This chapter presents the simulation results by the developed model in Chapter 6. For validation, we firstly compare the simulation results of an evaporating water droplet using present model and those using a single component model developed previously by Karapetsas et al.[16] The simulation results are then analyzed for two representative conditions, one is low relative humidity where vapor desorption happens, and the other is high relative humidity where vapor absorption happens. We reveal the evolution of droplet profile along with vapor absorption and desorption, then provide explanations to the droplet dynamics by elucidating the evolution of interfacial parameters along with time. Finally, we present the results of parametric analyses, and discuss the influences of important dimensionless numbers on the droplet dynamics and on the rate of vapor absorption.

7.1. Validation of present model

To check the reliability of the developed model, we compared the simulation results of pure water droplet by the present model and by a single component model developed by Karapetsas et al. [16] The single component model simulates the evaporation of pure water droplet on a heated substrate with constant temperature, and the evaporative mass flux is induced by the temperature difference between the liquid-air interface and the surrounding gas phase.

For comparison, we set the solute concentration in the absorptive model as 0%, *i.e.* 100% water concentration, and set the relative humidity (vapor concentration) of the gas phase as 100% so as to eliminate the effect of concentration difference. The substrate temperature is set as 1.0, and the temperature of gas phase is set as 0 for both two models. Other basic parameters for simulation are listed in Table 7.1.

Table 7.1Basic parameters used for comparison.

ε	Re	Pr	Ma	E
0.2	1.0	10	0.1, 1.0	1.0×10^{-4}
Kn	δ	A	Length of domain	Number of elements
1.0×10^{-5}	1.0×10^{-5}	1.0×10^{-4}	2.0	200

Figure 7.1 indicates the movement of the triple contact line and the evolution of droplet height along with time for two cases with different Marangoni numbers, Ma = 0.1 and Ma = 1.0. It shows that both models well predict the spreading-and-receding phenomena of pure water droplet undergoing evaporation. Moreover, at low Marangoni number (Ma = 0.1), the triple contact line advances more apparently, *i.e.* more apparent droplet spreading. The parameter curves by the two models overlap with each other, indicating the validity of present model in predicting the evolution of droplet profile and the dynamics of triple contact line.

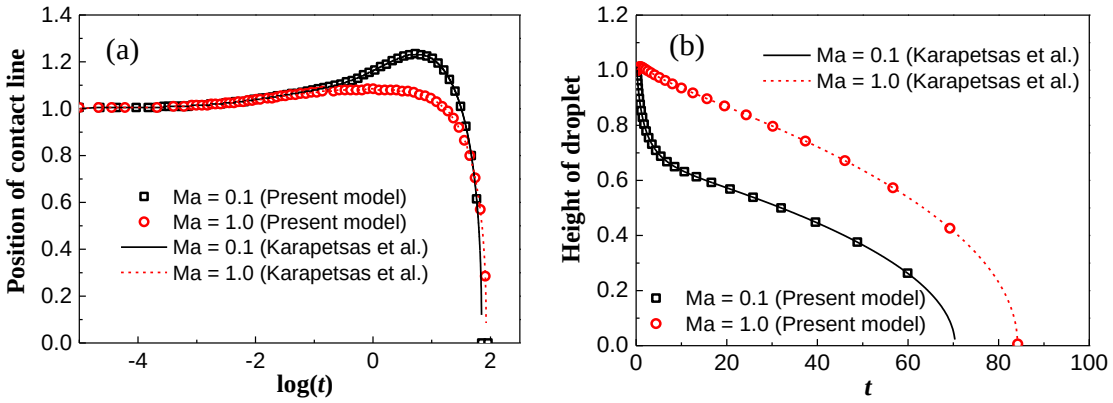

Figure 7.1 (a) Movement of triple contact line, and (b) Evolution of droplet height, along with time *t*, predicted by present model and by a single component model by Karapetsas et al.[16]

7.2. Case study

For a hygroscopic aqueous solution droplet, the direction of vapor diffusion depends on the relation between the solute concentration and the ambient relative humidity. In this model, we assume the aqueous solution as an ideal liquid mixture, and the humid air as an ideal mixture of inert gas and water vapor. Therefore, the water vapor pressure at the liquid-air interface can be approximated with the Raoult's law, and the partial pressure of

water vapor in the gas phase can be approximated by the mixing law of ideal gases. When the relative humidity is lower than the water concentration at the droplet surface, water vapor diffuses from the droplet side to the gas side following the concentration gradient of water vapor, *i.e.* vapor desorption. When the relative humidity is high, water vapor diffuses from the gas side with high vapor concentration towards the droplet surface with low water vapor concentration, and gets absorbed into the droplet bulk. In this section, we present and discuss the simulation results of a LiBr-H_2O droplet with 60 wt.% water concentration for three representative ambient conditions, *i.e.* desorption case (30% *RH*), equilibrium case (60% *RH*), and absorption case (90% *RH*), respectively.

Here, we assume the substrate temperature as the same with the environmental temperature, and only consider the difference of water vapor concentration. The base parameters for simulation are listed in Table 7.2.

Table 7.2 Basic parameters for simulation of the vapor absorption and desorption process

ε	T_g	T_w	Re	Pr	Ma	E	Kn
0.2	1.0	1.0	0	10	0.01	1.0×10^{-6}	1.0×10^{-3}
δ	A	ϑ	Pe	St	g_G	Length of domain	Number of elements
1.0×10^{-5}	1.0×10^{-4}	0.1	100	0.0368	1.0	8.0	800

7.2.1. Desorption cases: Low humidity

As shown in Figure 7.2(a), the mass of the droplet slowly decreases along with the desorption of water vapor at low humidity conditions with a timescale of ~10^3 s. As water vapor desorption goes on, a thin liquid film (thin, but much thicker than the precursor film) develops in front of the base of the droplet. The film extends, becomes thicker, and gradually develops into a ripple-like shape, indicated by the evolution of droplet profile from 1s to 700 s in Figure 7.2(b). At the same time, the main part of the droplet gradually shrinks, and coalesces with the ripple-like peripheral part. Finally, the inner part of the droplet fully coalesces into the peripheral ripple, and the ripple gradually flattens into a completely extended film across the calculation domain.

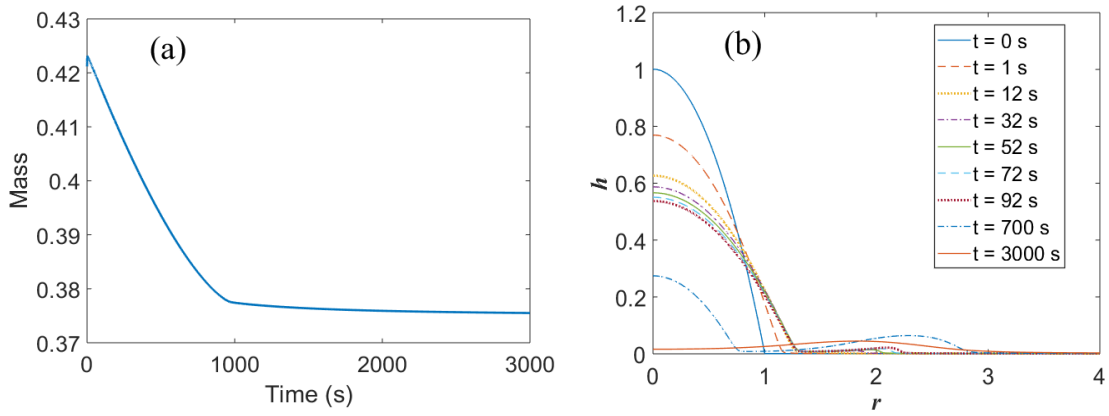

Figure 7.2 (a) Variation of droplet mass, and (b) Evolution of droplet profile in the *r* direction, along with time *t*. (χ_{H_2O} = 60%, RH = 30%.)

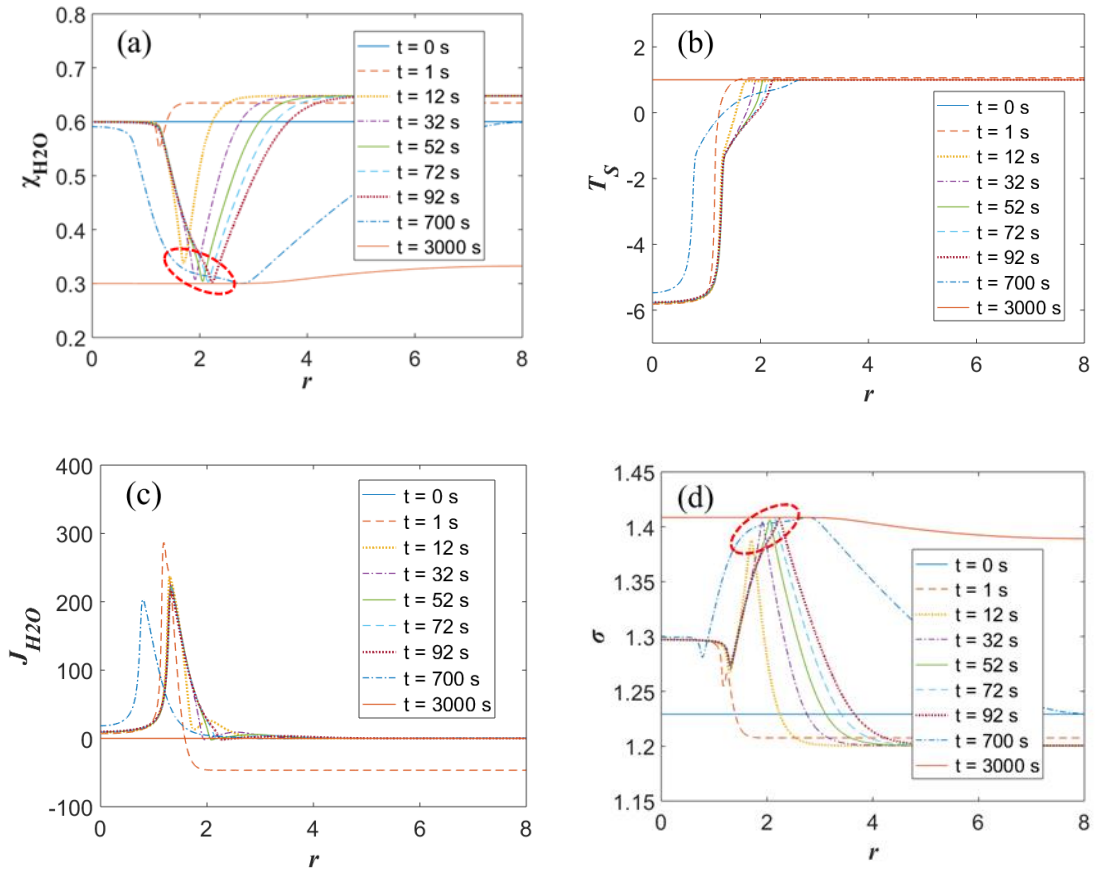

Figure 7.3 Distribution of (a) water concentration, (b) temperature, (c) mass flux, and (d) surface tension across the droplet surface at different instants of time. Condition: χ_{H_2O} = 60%, RH = 30%, dimensionless parameters are those listed in Table 7.2.

Figure 7.3 reveals the distributions of water concentration, interfacial temperature,

mass flux, and surface tension along *r* direction at different instants of time. As indicated by Figure 7.3(c), positive mass flux from the droplet surface towards the gas phase is induced by the concentration difference of water vapor. The liquid-gas transition takes away large amount of heat, causing the cooling down of the droplet surface as indicated by Figure 7.3(b). In the model, we assume the thermal conductivity of the substrate as very high, therefore, the interfacial temperature near the triple contact line is apparently higher than that near the droplet center due to much shorter length of heat transfer. Due to the more efficient heat supply from the substrate, the mass flux near the triple contact line is apparently higher than that near the droplet center (Figure 7.3(c)).

In the simulation, the Péclet number is set as 100, and the weak-diffusion assumption is applied. This means that the solute diffusion is rather slow in the simulated aqueous solution. Consequently, during the initial period of the process, the water concentration is the lowest in the area with the highest mass flux, shown by curves t = 1 s and t = 12 s in Figure 7.3(a) and (c). The surface tension of the aqueous solution is determined both by the solution temperature and by the water concentration. Compared to the influence of solution temperature, the influence of water concentration, or rather, solute concentration, is more apparent. As a joint result, the curves of surface tension show more similarity with the curves of water concentration, and in the area near droplet center, the surface tension curve is slightly lifted up due to apparently lower interfacial temperature.

The droplet dynamics is directly related with the interior flow. Figure 7.4 indicates the decomposed average flow velocity, *i.e*. capillary velocity, u_{ca}, solutocapillary velocity, u_{cg}, and thermocapillary velocity, u_{tg}, according to the derived equations (7.1)-(7.3).

$$u_{\mathrm{ca}} = -\frac{h^2}{3\mu}\frac{\partial p_0}{\partial r}, \tag{7.1}$$

$$u_{\mathrm{cg}} = -\frac{h}{2\mu \mathrm{Ma}}\eta_\sigma \frac{\partial \chi_{\mathrm{H_2O}}}{\partial r}, \tag{7.2}$$

$$u_{\mathrm{tg}} = \frac{h}{2\mu \mathrm{Ma}}\zeta_\sigma \frac{\partial T_{\mathrm{s}}}{\partial r}. \tag{7.3}$$

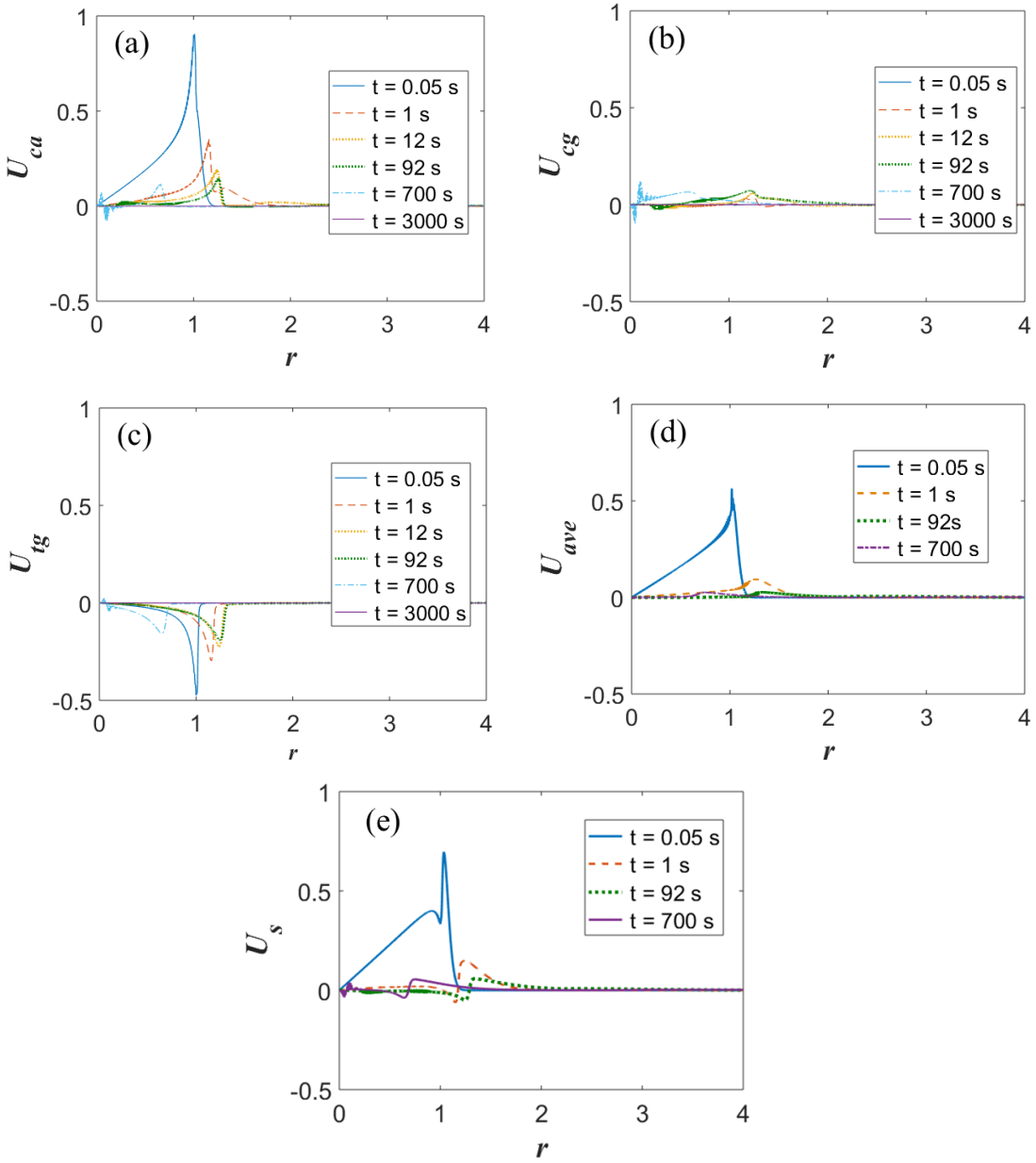

Figure 7.4 Decomposed velocities in the *r* direction: (a) capillary velocity, (b) solutocapillary velocity, (c) thermocapillary velocity. (d) overall average flow velocity, (e) flow velocity at the droplet surface. Condition: χ_{H_2O} = 60%, RH = 30%.

Overall, the capillary effect driven by capillary pressure induces positive flow in the *r* direction. The solutocapillary effect due to surface tension gradient also induced positive flow in the *r* direction due to much higher solute concentration near the contact line. The thermocapillary effect induced by temperature gradient tends to drive the flow towards the cold area near the droplet center.

Compared to that of pure water droplet, the mass flux during vapor desorption of hygroscopic droplet is greatly influenced by the solute concentration. During the evaporation of pure water droplet, the droplet firstly spreads due to capillary effect. At the same time, the depletion of water and the surface tension gradient due to temperature difference tend to drag back the contact line. When the spreading tendency reaches balance with the receding tendency, the droplet stops spreading, and subsequently recedes. When it comes to hygroscopic droplets, the liquid near triple contact line cannot be totally dried out due to the existence of hygroscopic salt. Instead, the solute concentration in this area will increase and suppress further water evaporation. The increased solute concentration also induces high surface tension in the area near contact line, and causes the positive solutal capillary flow shown in Figure 7.4(b). The joint result of capillary and solutal capillary effect outweighs the thermal capillary effect. Consequently, the hygroscopic droplet spreads continuously along with vapor desorption, and finally evolves into a flat film across the calculation domain, fully balanced with the environment.

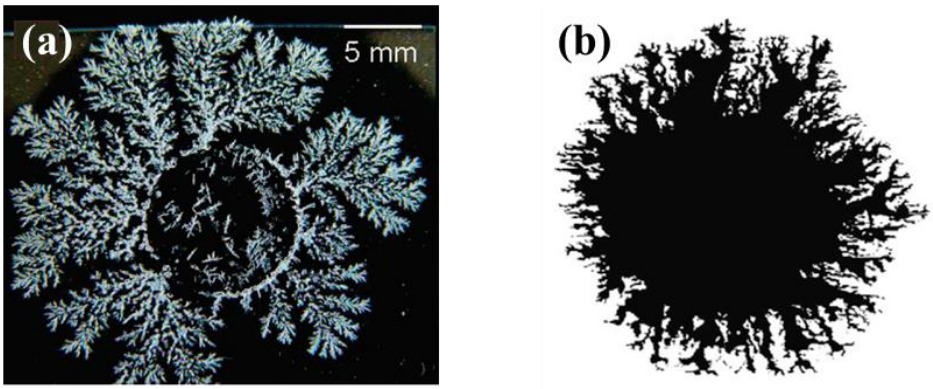

Figure 7.5 Patterns formed from the evaporation of (a) saturation Na_2SO_4 solution droplets, and (b) droplets with nanosuspensions of Ethylene glycol.

We also notice that similar evaporation-spreading phenomena are reported in existing literature. In 2008, Shahidzadeh-Bonn et al.[104] investigated the salt crystallization during the evaporation of saturated Na_2SO_4 droplets on hydrophilic glass substrates. They reported the formation of dendritic anhydrous crystal around the contact line shown in Figure 7.5(a). However, for NaCl droplets, the deposition pattern is constraint by the

contact line, and no external structure is observed. Subsequently, in 2014, Hadj-Achour and Brutin[171] reported similar fractal pattern from evaporating nano-suspension droplets shown in Figure 7.5(b). More importantly, such external structures only appear for droplets with Ethylene glycol suspensions, while the depositions from droplets with Triethylene glycol monomethyl ether and with Tetradecane are close to a circular form.

We further checked the properties of the five experimental solutions, namely, Na_2SO_4, NaCl, Ethylene glycol, Triethylene glycol monomethyl ether, and Tetradecane. We find that both Na_2SO_4 and Ethylene glycol have high affinity to water molecules, and have been applied as desiccants and drying agents for dehumidification and dehydration uses. The other three substances are just normal without special affinity to water molecules. Therefore, we can reasonably infer that the hygroscopic properties of Na_2SO_4 and Ethylene glycol aqueous solution lead to the formation of thin film in front of the triple contact line as indicated by our above analysis. Along with water evaporation, crystals and fractal patterns form in the saturation solution film. As the droplet dries out, the deposition remains at the substrate surface, and forms the structure observed by the experiments.

7.2.2. Absorption cases: High humidity

When the air humidity is high, water vapor diffuses from the gas side with high vapor concentration towards the droplet surface with low vapor concentration. The water vapor gets absorbed into the droplet, causing the growth of the droplet. Figure 7.6(a) shows the evolution of droplet mass along with time during vapor absorption. In 170 s of the virtual time, the droplet mass increases from 0.42 to 0.50, and the saturation trend of the variation curve well corresponds with the experimental results. Figure 7.6(b) shows the evolution of droplet profile along with vapor absorption. Upon contacting the substrate, the droplet starts to spread with decreasing droplet height, as indicated by curves t = 0 s, t = 1 s, t = 12 s. After that, the triple contact line starts to recede with increasing droplet height. The process proceeds until the program diverges after ~170 s. The reason will be discussed in the following analyses.

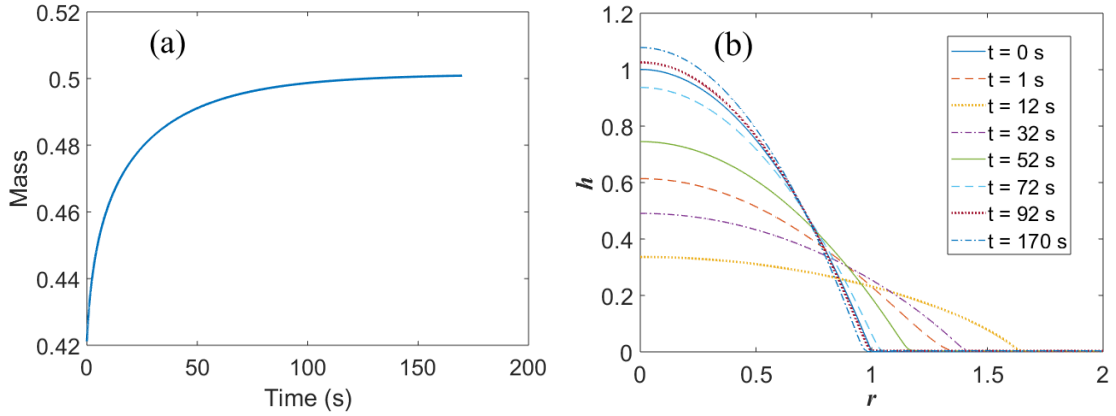

Figure 7.6 (a) Variation of droplet mass, and (b) Evolution of droplet profile in the *r* direction, along with time *t*. (χ_{H_2O} = 60%, RH = 90%.)

Figure 7.7 shows the distribution of water concentration, temperature, mass flux, and surface tension across the droplet surface at different instants of time. In the model, we assume the initial water concentration in the precursor film as the same with the main body of the droplet. Therefore, a non-zero mass flux will exist in the precursor film during the initial period. Since the precursor film is very thin, the process will soon terminate after the precursor film absorbs sufficient water and reaches equilibrium with the environment.

Overall, the mass flux is a joint result of the Laplace pressure by surface curvature, the van der Waals force due to molecule interactions, the temperature difference between the droplet surface and ambient, and the relation between water vapor concentration at the liquid-air interface and the vapor concentration in the gas phase. At the initial moment, the temperatures of the droplet, the substrate, and the gas phase are in equilibrium, and the distribution of water concentration within the droplet is uniform. Due to the spatial variation of profile curvature and droplet height, non-uniform mass fluxes are induced across the droplet profile. At the droplet center, the curvature of the profile is zero, and droplet height is the largest (negligible van der Waals effect), corresponding to the smallest mass flux. In the region near contact line and the precursor film, due to the extremely small thickness of liquid film, the van der Waals force is considerable, which enhances the adsorption of water vapor, and corresponds to the highest absorptive mass

flux.

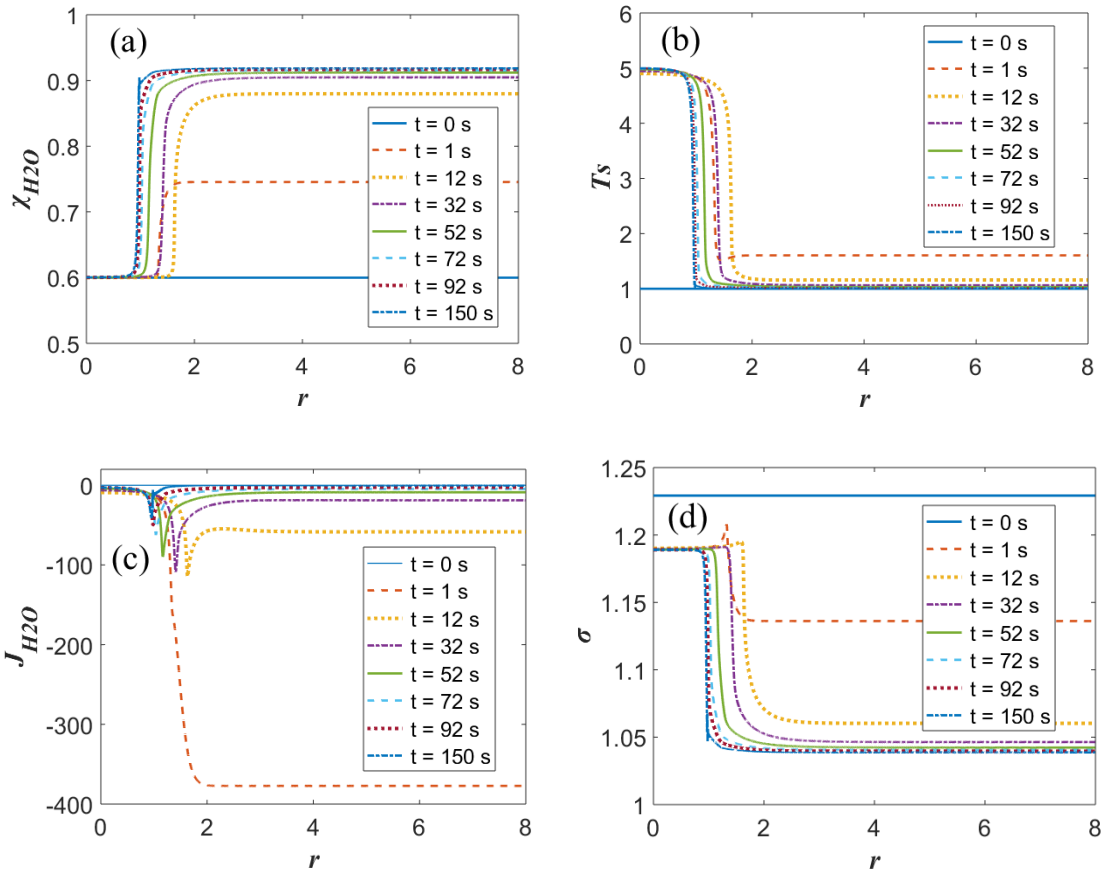

Figure 7.7 Distribution of (a) water concentration, (b) temperature, (c) mass flux, and (d) surface tension across the droplet surface at different instants of time. (χ_{H_2O} = 60%, RH = 90%.)

The absorptive mass flux causes the increase in water concentration within the droplet. At the precursor film, the water concentration increases rapidly due to the large absorptive mass flux and the extremely small film thickness (indicated by curves t = 1 s and t = 12 s in Figure 7.7(a)). The increase of water concentration and film thickness in turn decreases the driving force for vapor absorption, and causes a rapid decrease in the mass flux at the region of precursor film.

Figure 7.8 depicts the distribution of absorptive mass flux, water concentration and droplet height in the r direction at the moment of t = 65 s. At the area near contact line, the interfacial temperature, the water concentration, and the curvature of droplet profile

all experience significant variations. As a joint result of droplet height, profile curvature, water concentration, and interfacial temperature, the absorption mass flux reaches a peak value at a position close to the triple contact line.

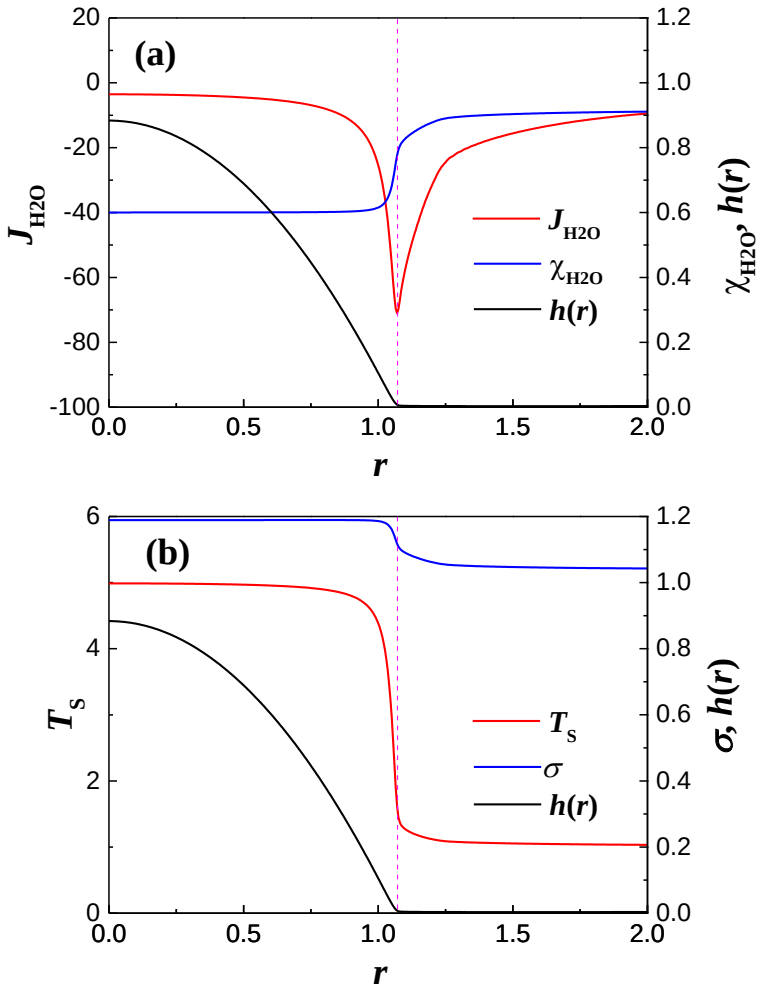

Figure 7.8 Distribution of (a) absorptive mass flux, J_{H_2O}, water concentration, χ_{H_2O}, along with droplet profile, and (b) interfacial temperature, T_S, surface tension, σ, along with droplet profile, at the moment of t = 65 s. (χ_{H_2O} = 60%, RH = 90%.)

In Chapter 6, we derived the expression of mass flux based on the Hertz-Knudsen equation and the thermodynamic equilibrium equation. From the expression of mass flux, eq. (6.62), we can decompose the mass flux as mass flux by Laplace pressure and van der Waals force, J_P, mass flux by temperature difference, $J_{\Delta T}$, and mass flux by concentration difference of water vapor, $J_{\Delta\chi}$, expressed as eqs. (7.4)-(7.6).

$$J_P = \frac{\chi_{\mathrm{H_2O}}\delta}{\mathrm{Kn}}\left(p_0 - \mathrm{St}\rho g_G h\right), \tag{7.4}$$

$$J_{\Delta T} = \frac{\chi_{\mathrm{H_2O}}\vartheta}{\mathrm{Kn}}\left(T_\mathrm{S} - T_g\right), \tag{7.5}$$

$$J_{\Delta\chi} = \frac{\chi_{\mathrm{H_2O}}}{\mathrm{Kn}}\ln\left(\frac{\chi_{\mathrm{H_2O}}}{\chi_{\mathrm{H_2O,g}}}\right). \tag{7.6}$$

Figure 7.9 depicts the decomposed mass flux across the droplet profile at the moment of t = 65 s. At the region near droplet center, due to the small absorptive mass flux and the water diffusion into the droplet bulk, the water concentration at the interface is low, while the interfacial temperature is high due to the effect of absorptive heating and the long characteristic length of heat transfer into the substrate. The low water concentration at the droplet interface tends to induce a negative mass flux, while the high interfacial temperature tends to induce a positive mass flux as indicated by the green and purple curves in Figure 7.8. The effects of high temperature and low water concentration offset with each other, causing the overall negative and small mass flux at the main central region of the droplet. Along r direction, the droplet height decreases, and at the area near triple contact line, the droplet height decreases apparently, therefore, the heat can be more efficiently transferred into the substrate. Meanwhile, as the liquid film becomes thinner, the liquid layer is easier to get saturated. However, compared to the heat transfer, the speed of mass transfer is slower, therefore, the slope of the green curve is smaller than the slope of the purple curve near contact line. As a result, a negative peak mass flux appears at a position near contact line (red solid curve in Figure 7.9).

All in all, the distribution of absorptive mass flux shares both similarities and differences with the distribution of mass flux during droplet evaporation. On one hand, both the evaporative mass flux and absorptive mass flux increase with the radius r, and reach the maximum at the region near triple contact line. On the other hand, as shown by Figure 7.7(c), the absorptive mass flux, especially its value near contact line, decreases along with time due to the decrease of driving force caused by increasing water concentration. Nevertheless, for pure volatile liquid droplets, the evaporative mass flux keeps almost constant throughout the droplet lifetime since the vapor concentration at the

liquid-air interface keeps constant for pure liquid cases.

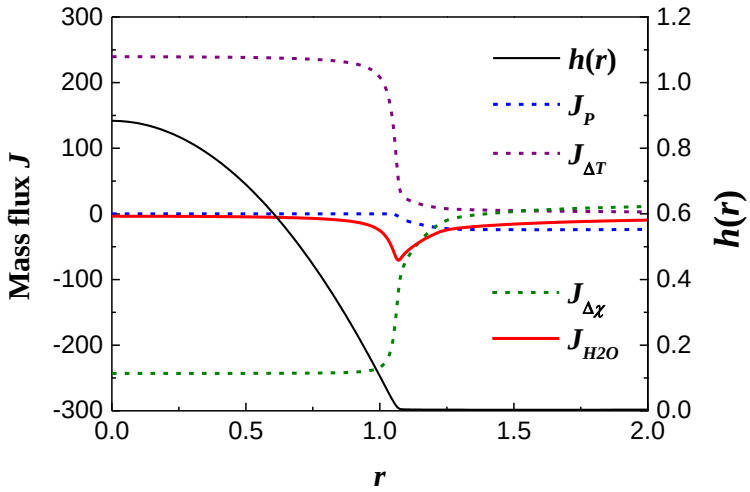

Figure 7.9 Distribution of decomposed mass fluxes along with droplet profile, at the moment of t = 65 s. (χ_{H_2O} = 60%, RH = 90%.)

Figure 7.10 depicts the decomposed flow velocity along r direction at different instants of time. The capillary effect is induced by the capillary pressure due to the gradually-converging droplet profile, which contributes to an outward capillary flow and drives the contact line to move forward. As vapor absorption takes place, the latent heat released during vapor-water phase change tends to heat up the droplet, and the distance from the substrate decides the distribution of temperature across the droplet surface as indicated by Figure 7.7(b). The spatial distribution of interfacial temperature contributes to a positive surface tension gradient, and induces positive interfacial flow from the hot area near droplet center to the cold area near triple contact line. On the other hand, the concentration gradient contributes to a negative surface tension gradient, since the surface tension at the droplet center with low water concentration is apparently higher than the surface tension near triple contact line with high water concentration. The negative surface tension gradient contributes to an inward solutal capillary flow which tends to drag back the contact line and cause the droplet to recede.

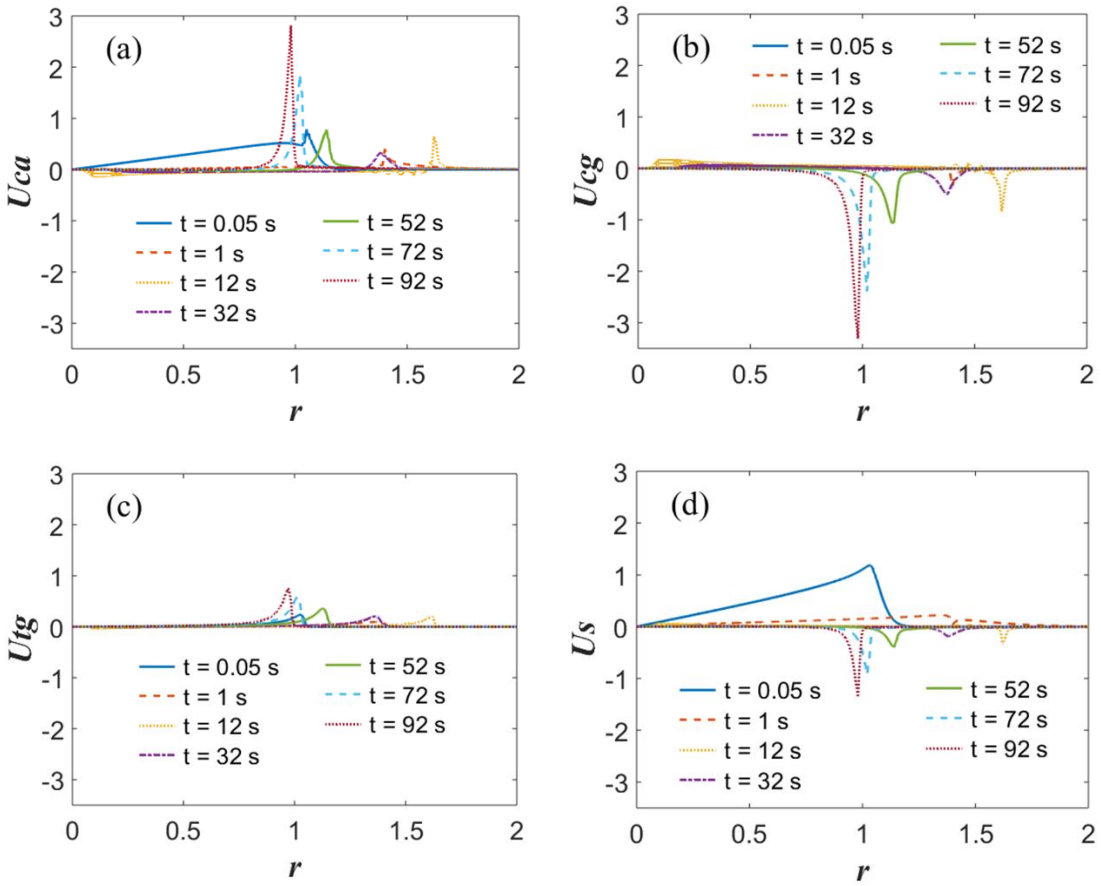

Figure 7.10 Decomposed velocities in the *r* direction: (a) capillary velocity, (b) solutocapillary velocity, (c) thermocapillary velocity. (d) flow velocity at the droplet surface. Condition: χ_{H_2O} = 60%, RH = 90%.

Quantitatively, as indicated by Figure 7.10(a), (b), and (c), the capillary flow velocity and solutocapillary flow velocity are apparently larger that the thermocapillary velocity. During the initial period of vapor absorption, *e.g.* t = 0.05 s, the capillary effect drives the droplet to spread, and the thermocapillary effect slightly enhances this process. The droplet spreading proceeds for ~ 12 s. After that, the solutocapillary effect starts to dominate the droplet dynamics, and causes the receding of the droplet. As vapor absorption goes on, the concentration gradient becomes larger due to accumulated difference of mass flux at the center and edge of the droplet. Consequently, the solutocapillary effect strenthens and speeds up the droplet receding. As the contact line recedes, the slope near the contact line becomes larger and larger. The value goes up to

infinite numerically as the process goes on, which finally makes the program fail to converge.

In our model, we apply the lubrication theory to simplify the governing equations, and release the droplet onto a thin precursor film to avoid the singularity near the triple contact line. The precursor film assumption allows the contact line to move freely, and makes it possible to reveal the droplet dynamics on an ideally smooth substrate. Nevertheless, in our experiments, there is non-negligible hysteresis at the glass substrate, and the receding contact angle is rather small according to our measurements. For cases of vapor absorption, the experimental results indicate that the droplet spreads continuously with decreasing contact angle and increasing contact radius, while the numerical results report a firstly-spreading-then-receding behavior of the droplet. Despite of the inconsistency, the numerical analyses clearly indicate the mechanisms governing the droplet dynamics, and provides reasonable theoretical explanations to the observed droplet behaviors during vapor absorption and desorption. Further modifications will be done to include the effect of hysteresis into the model.

7.3. Parametric analysis

In this section, we present the parametric analyses of four important dimensionless numbers, namely, the Stokes number, the Marangoni number, the Evaporation number, and the Péclet number. We choose the vapor desorption condition, χ_{H_2O} = 60% and RH = 30%, as the basic case, and summary the effect of different dimensionless numbers on droplet spreading and on the rate of vapor desorption.

7.3.1. Stokes number

The Stokes number appears in the gravitational term of the vertical direction momentum equation during the scaling process, defined as, $\mathrm{St} = \dfrac{\hat{\rho}_{H_2O} \hat{g} \hat{H}_0^3}{\hat{\mu}_{H_2O} \hat{u}^* R_0}$. The value of Stokes number indicates the importance of gravitational effect on the fluid kinetics in the

z direction.

Figure 7.11(a) and (b) shows the evolution of contact line position and the droplet height along with time, for Stokes number of 0.01, 1, 10, and 100. The results show that increasing Stokes number will speed up the droplet spreading along with vapor desorption. Compared to the case of St = 0.01, the contact line advances slightly faster in the case of St = 1, along with a faster decrease in the droplet height. By further increasing the Stokes number to 10 and 100, the advancing speed of the contact line greatly increases, and the droplet height decreases more rapidly.

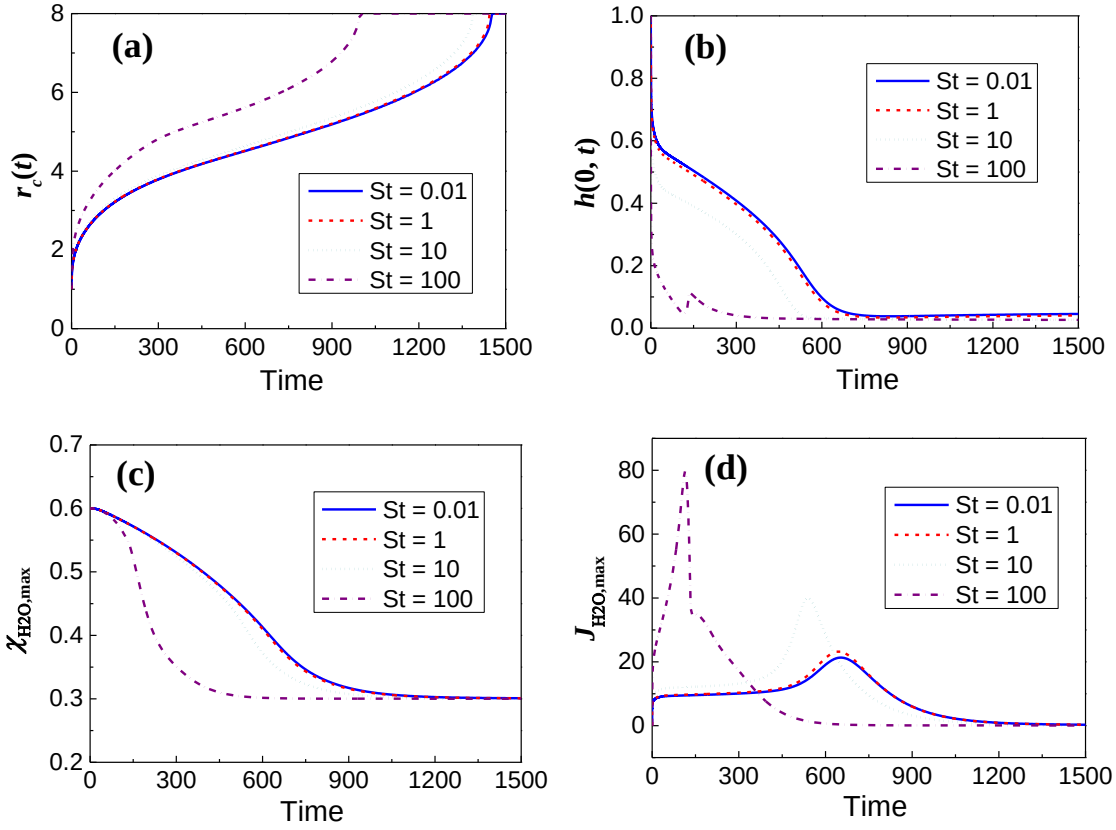

Figure 7.11 Evolution of (a) contact line position, (b) droplet height, (c) maximum water concentration, and (d) maximum mass flux for different Stokes numbers of 0.01, 1, and 100. (χ_{H_2O} = 60%, RH = 30%.)

Figure 7.11 (c) and (d) indicate the evolution of the maximum water concentration and maximum mass flux across the droplet surface. In cases of large Stokes numbers, the gravitational effect enlarges the gradient of liquid pressure in the *z* direction, and induces

vertical flow convection. The convective flow contributes to an increasing rate of solute diffusion, and enables a more efficient water supply to the liquid-air interface along with vapor desorption. Moreover, the more apparent droplet spreading also contributes to a thinner fluid film, and leads to greater mass flux at the edge of the droplet. As indicated in Figure 7.11 (d), the maximum mass flux at the droplet surface is apparently larger at large Stokes number. As a result of the large mass flux of vapor desorption, the water concentration decreases more rapidly, and the system reaches equilibrium faster in the case of large Stokes number.

7.3.2. Marangoni number

The Marangoni number evaluates the thermal Marangoni and solutal Marangoni effect. At large Marangoni numbers, the surface tension gradient is more apparently influenced by the gradient of interfacial temperature and solute concentration across the droplet surface. Figure 7.12 indicates the evolution of the contact line position, droplet height, as well as the maximum water concentration and mass flux along with time for Marangoni numbers of 0.01,0.1, and 1. It shows that the advancing speed of the contact line decreases with increasing Marangoni number, and the droplet requires more time to reach equilibrium with the ambient at large Marangoni numbers.

From our analysis above in Figure 7.4, it shows that the droplet dynamics is dominated by the capillary effect and the thermal capillary effect during vapor desorption. By increasing the Marangoni number, the inward thermal capillary effect is strengthened, which offsets the outward capillary effect, thus slows down the advancing of the triple contact line. Due to the fast droplet spreading at small Marangoni numbers, the thickness of the droplet becomes smaller, which leads to a greater evaporation mass flux indicated by the curves of Ma = 0.1 and Ma = 1 in Figure 7.12(d).

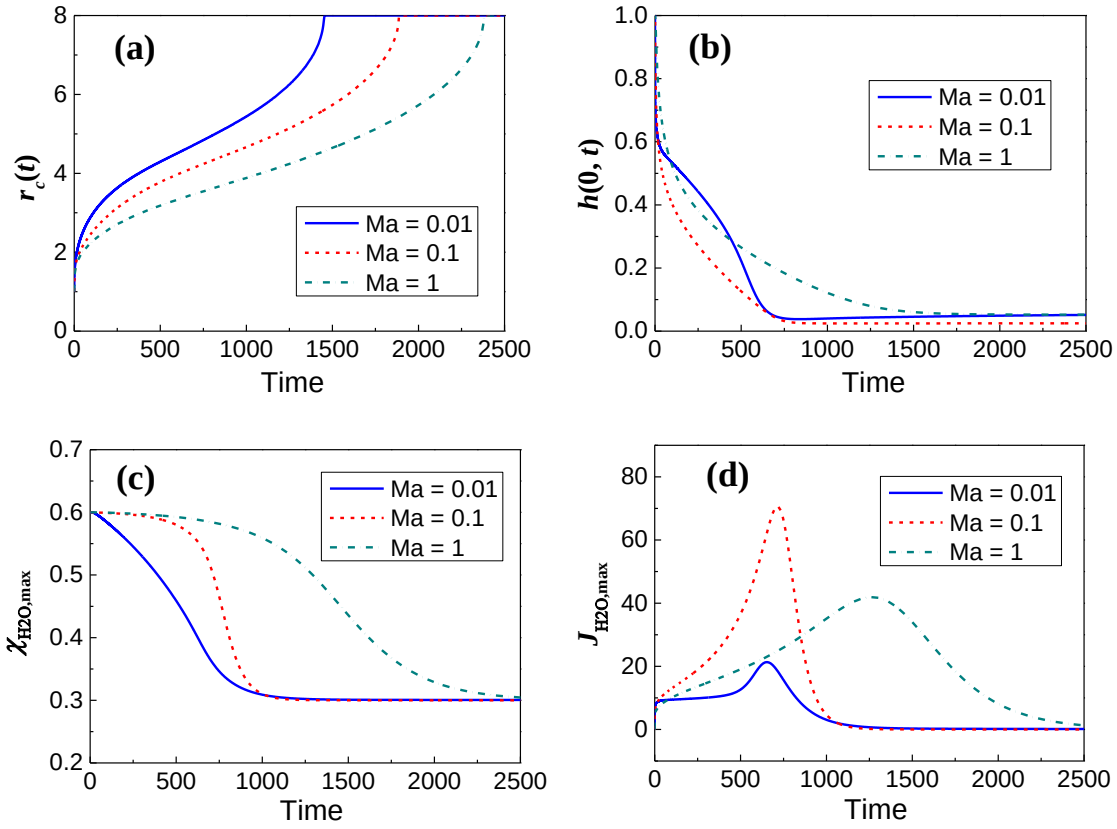

Figure 7.12 Evolution of (a) contact line position, (b) droplet height, (c) maximum water concentration, and (d) maximum mass flux for different Marangoni numbers of 0.01, 0.1, and 1. (χ_{H_2O} = 60%, RH = 30%.)

7.3.3. Evaporation number

The evaporation number appears in the scaling process of mass flux boundary condition, defined as, $E = \dfrac{\hat{D}_{H_2O}\hat{R}_0\Delta\chi_{H_2O}}{\hat{H}_0^2\hat{u}^*}$. Increasing the evaporation number enhances the intensity of water vaporization. As indicated by Figure 7.13(d), the mass flux at evaporation number of 10^{-4} increases most rapidly right after the droplet contacts with the substrate. Along with the large evaporation mass flux, the water concentration within the droplet decreases rapidly as indicated by the dash-dot curve in Figure 7.13(c). Due to the greater evaporation mass flux near the droplet edge, the water concentration near contact line becomes apparently lower than that near droplet center. The consequent surface tension gradient drives the interior flow towards the contact line, and causes the rapid

decrease in the film thickness at the droplet center (Figure 7.13 (c)). Along with the depletion of fluid at the droplet center, a ripple forms at the edge of the droplet, which develops rather slowly due to the greatly weakened capillary effect, and finally flattens out into an equilibrium state with the ambient.

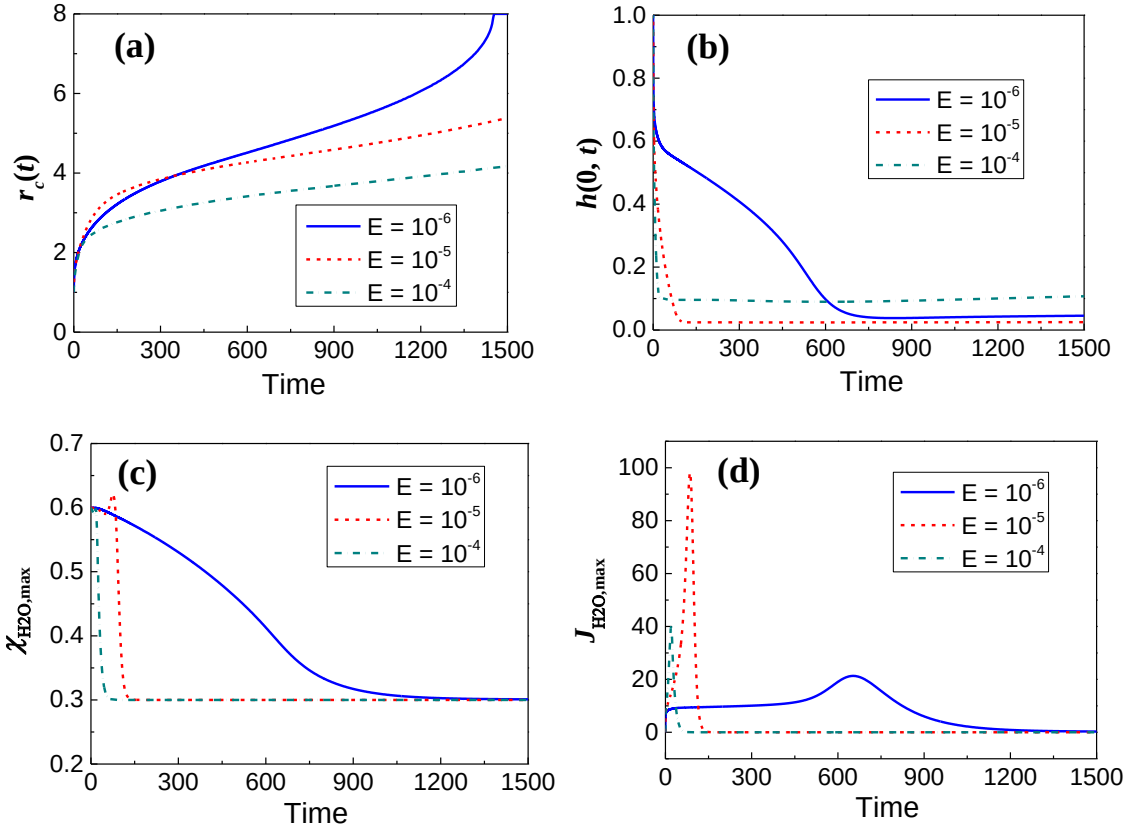

Figure 7.13 Evolution of (a) contact line position, (b) droplet height, (c) maximum water concentration, and (d) maximum mass flux for different Evaporation numbers of 10^{-6}, 10^{-5}, and 10^{-4}. (χ_{H_2O} = 60%, RH = 30%.)

When the evaporation number is low, *e.g.* $E = 10^{-6}$, the evaporation mass flux is much lower, and the desorption process sustains for a longer period indicated by the blue solid curve in Figure 13(d). Along with the slow evaporation, the water concentration within the droplet decreases slowly, and the concentration gradient is also smaller. The consequently smaller surface tension gradient leads to a slow decrease in the film thickness near droplet center (Figure 7.13(b)).

7.3.4. Péclet number

The Péclet number evaluates the relation between advective mass transfer and diffusive mass transfer, defined as, $\mathrm{Pe} = \dfrac{\hat{u}^* \hat{R}_0 \hat{\rho}_{\mathrm{H_2O}}}{\hat{D}_{\mathrm{H_2O}}}$. When Péclet number is relatively small, *e.g.* Pe = 1 and Pe = 10, rapid solute diffusion ensues within the droplets, and we apply the rapid diffusion approximation to simplify the advection diffusion equation, eq. (6.85). When the Péclet number is large, *e.g.* Pe = 100, we apply the weak diffusion approximation, eq. (6.86).

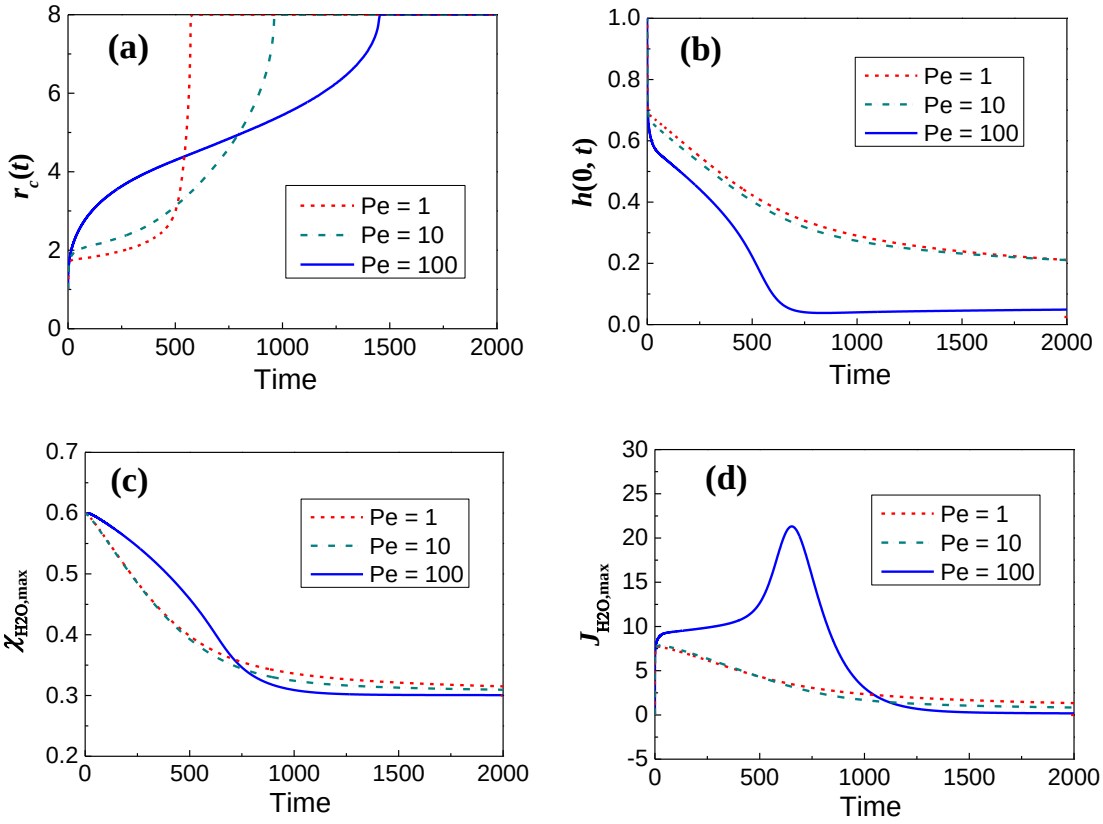

Figure 7.14 Evolution of (a) contact line position, (b) droplet height, (c) maximum water concentration, and (d) maximum mass flux for different Péclet numbers of 1, 10, 100, and 1000. ($\chi_{\mathrm{H_2O}}$ = 60%, RH = 30%.)

Figure 7.14(a) and (b) show the evolution of the position of contact line and the height of droplet center along with vapor desorption. It shows that all droplets experience a rapid spreading at the very initial seconds due to the capillary effect. After that, the contact line

of the droplet advances slowly at small Péclet numbers, then speeds up until fully spreading. For cases of large Péclet numbers, the droplet spreads rapidly in the first several hundred seconds, then slows down, and finally flattens out. All in all, droplets with large Péclet numbers take longer time to spread than droplets with small Péclet numbers.

For practical liquid desiccant droplets the diffusion coefficient of salt ions is rather low, and the Péclet number is usually large. In such cases, the solute diffusion within the droplet takes longer time, therefore, large surface tension gradient is induced due to the preferential water evaporation near the contact line. The solutal capillary flow induced by surface tension gradient drives an outward flow, and strengthen the droplet spreading during the first several hundred seconds. As the droplet becomes thinner, the maximum mass flux across the droplet surface increases, and reaches a peak at the moment of ~700s. After that, the mass flux decreases due to the apparently decreasing water concentration.

For droplets with small Péclet numbers, the water concentration decreases continuously due to efficient water supply to the liquid-vapor interface, and the droplet height decreases slowly due to the slow spreading. As a joint result of the large liquid thickness and the deceasing water concentration, the mass flux decreases continuously along with time, which differs from that of droplets with large Péclet numbers.

7.4. Summary

This chapter presents the simulation results by the lubrication-type model developed in chapter 6. The droplet behaviors are analyzed and discussed for low humidity and high humidity conditions. In the case of low humidity, slowly droplet spreading is reported along with vapor desorption. The droplet spreading is attributed to the strong capillary effect and solutal capillary effect which generates outward flow towards the triple contact line. The simulation results also provide a reasonable explanation to the experimental results of previous researchers, where patterns form at the periphery of the contact line of drying hygroscopic droplets.

In the case of high humidity, vapor absorption happens, and preferential absorptive mass flux exists near the triple contact line. Results show that the droplet firstly spreads due to the capillary effect, then recedes due to the increased inward solutal capillary flow. In our experiments, continuous droplet spreading is observed due to the strong hysteresis of glass substrates. Despite the inconsistency, the numerical analysis explicitly reveals the governing mechanisms underneath.

Further parametric analyses are carried out to reveal the effects of Stokes number, Marangoni number, Evaporation number, and Péclet number taking the vapor desorption process as an example.

Part IV Conclusions

Chapter 8 Conclusions

In the field of air conditioning, waste heat recovery, and desalination, the most crucial task is to realize directional water vapor transport, so that we can accurately control the humidity of living environment, recover the latent heat contained in flue gases, and extract fresh water for water-deficit areas. The liquid desiccant is one type of aqueous solution with hygroscopic properties. By controlling its solute concentration and temperature, the liquid desiccant can either absorb or desorb water vapor, making it possible to transport water vapor in a controllable and efficient way.

This thesis focuses on the vapor absorption process into single hygroscopic liquid desiccant droplets. In the experimental part, individual investigations are carried out to study the effect of substrate wettability and the coupling effect of heat and mass transfer. In the simulation part, we develop a lubrication-type model to reveal the distribution of mass flux, the interfacial parameters, and the interior flow within a droplet undergoing vapor absorption or desorption.

The first series of experiments aim to reveal the effects of substrate wettability and environmental condition on the droplet dynamics and on the rate of vapor absorption. Experiments are conducted on hydrophilic glass and hydrophobic PTFE substrates at controlled conditions. It shows that the rate of vapor absorption is higher on hydrophilic substrates due to the apparently shorter characteristic length for solute diffusion within the droplet. Moreover, the state of the droplet is decided by the balance of water vapor concentration between the droplet liquid-air interface and the humid air. Therefore, the final value of expansion only depends on the relative humidity of the ambient air, regardless of the experimental temperature and surface wettability. Besides, we emphasize on the apparent droplet spreading on hydrophilic glass substrates. The phenomenon is explained based on a force balance analysis at the triple contact line, by the evolution of liquid-gas droplet surface tension, and by the development of a precursor

film during vapor absorption.

The second series of experiments aim to reveal the coupling effect of the thermal transport and mass diffusion process along with vapor absorption. The evolution of droplet profile and the distribution of interfacial temperature are recorded simultaneously using optical imaging and infrared thermography. Results show that the liquid desiccant droplet experiences a rapid temperature increase during the deposition process due to fast vapor absorption. Upon contact with the substrate, the droplet temperature gradually decreases as a joint result of heat dissipation and the decreased vapor absorption rate. We further derive the vapor pressure difference between the droplet interface and the ambient taking account of the variations of interfacial temperature and solute concentration. The calculation results show good correspondence with the order of vapor absorption rate for six representative environmental conditions. Along with time, the vapor pressure difference, i.e. the driving force for vapor diffusion, decreases, which elucidates the saturation increasing trend of droplet volume during vapor absorption.

To better understand the droplet dynamics, we develop a two-dimensional model using the lubrication theory. The model allows for the free motion of the triple contact line by assuming a precursor film at the periphery of the droplet. We analyze the droplet kinetics for two representative cases: one is at low relative humidity where vapor desorption happens, and the other is at high relative humidity where vapor absorption happens.

For the case of vapor desorption, the droplet spreads rapidly at the initial stage driven by the capillary force. Along with droplet spreading, water evaporation happens and the evaporation mass flux varies spatially across the droplet surface. At the area near triple contact line, the mass flux reaches the peak due to more efficient heat supply. Due to the hygroscopic property of liquid desiccant, the liquid near contact line cannot totally vaporize, consequently, a thin ripple-like film forms. At the same time, the low water concentration near contact line induces surface tension gradient and a solutal capillary flow towards the contact line, which strengthens the spreading of the droplet. The

simulation results also provide a reasonable explanation to the experimental results of Shahidzadeh-Bonn et al. [104] and Hadj-Achour et al.[171], where dendritic anhydrous crystals and fractal patterns form at the periphery of the contact line of drying aqueous solution droplets with hygroscopic properties.

For the case of vapor absorption, simulation results show that the droplet firstly spread driven by the capillary force. As vapor absorption takes place, the heat released due to vapor-water phase change causes an increase in the interfacial temperature. At the area near contact line, the interfacial temperature keeps low due to more efficient heat removal into the substrate. The thermal effect causes the preferential distribution of absorptive mass flux near the contact line. As a result, the water concentration near contact line becomes apparently higher than that at the droplet center. As a result of the surface tension gradient induced by water concentration difference, solutal capillary flow forms towards the droplet center, and causes the receding of the triple contact line. In our experiments, nevertheless, the droplet spreads continuously due to the hysteresis effect of glass substrates. Despite of the inconsistency, the simulation clearly reveals the mechanisms governing the droplet behaviors during vapor absorption. Further modifications will be done to include the effect of hysteresis into the model.

All in all, this research concentrates on the vapor absorption process into single liquid desiccant droplet, which differs from both droplet evaporation and dropwise condensation, indicating a new research subroutine of droplet phase change. Specifically, this thesis reveals the droplet kinetics, the contact line motion, the coupled heat and mass transfer, the distribution of mass flux, and the interfacial flow of liquid desiccant droplets during vapor absorption. By combining experimental observation and numerical simulation, we elucidate the effects of substrate wettability, environmental temperature, relative humidity, and different fluid properties on the vapor absorption process. The results contribute to our present knowledge of the phase change and fluid dynamics of binary droplets. Conclusions on the effects of different influencing factors provide valuable instructions for the design and optimization of practical devices for dehumidification uses.

List of Publications

Journal articles

1. **Wang, Z.**, Orejon, D., Takata, Y., & Sefiane, K. " Coupled thermal transport and mass diffusion during vapor absorption into hygroscopic liquid desiccant droplets" *International Journal of Heat and Mass Transfer* 134 (2019): 1014-1023.

2. **Wang, Z.**, Orejon, D., Sefiane, K., & Takata, Y. "Water vapor uptake into hygroscopic lithium bromide desiccant droplets: Mechanisms of droplet growth and spreading." *Physical Chemistry Chemical Physics* 21 (2019): 1046-1058. (Back Cover)

3. Josyula, T., **Wang, Z.**, Askounis, A., Orejon, D., Harish, S., Takata, Y., Sinha Mahapatra, P. & Pattamatta, A. "Evaporation kinetics of pure water drops: Thermal patterns, Marangoni flow, and interfacial temperature difference." *Physical Review E* 98.5 (2018): 052804.

4. **Wang, Z.**, Zhang, X., Han, J., & Li, Z. "Waste heat and water recovery from natural gas boilers: Parametric analysis and optimization of a flue-gas-driven open absorption system." *Energy Conversion and Management* 154 (2017): 526-537.

5. **Wang, Z.**, Zhang, X., & Li, Z. "Investigation on the coupled heat and mass transfer process between extremely high humidity air and liquid desiccant in the counter-flow adiabatic packed tower." *International Journal of Heat and Mass Transfer* 110 (2017): 898-907.

6. **Wang, Z.**, Zhang, X., & Li, Z. "Simulation of a flue gas driven open absorption system for waste heat recovery from fossil fuel boilers." *ASHRAE Transactions* 123.1 (2017).

7. Zhang, X., **Wang, Z.**, & Li, Z. "A novel flue gas heat recovery system based on low-pressure regeneration liquid desiccant cycle." *International Journal of Low-Carbon Technologies* 13.1 (2017): 1-5.

8. **Wang, Z.**, Cao, H., & Li, Z. Cold source selection and efficiency analysis of data center cooling systems. *Journal of Engineering Thermophysics* 38(2) (2017): 326-333. (In Chinese)

9. **Wang, Z.**, Zhang, X., & Li, Z. "Evaluation of a flue gas driven open absorption system for heat and water recovery from fossil fuel boilers." *Energy Conversion and Management* 128 (2016): 57-65.

10. **Wang, Z.**, Zhang, X., Li, Z., & Luo, M. "Analysis on energy efficiency of an integrated heat pipe system in data centers." *Applied Thermal Engineering* 90 (2015): 937-944.

Conferences

1. **Wang, Z.**, Orejon, D., Sefiane, K., & Takata, Y. Vapor absorption phenomenon onto liquid desiccant droplet driven by vapor pressure difference, 5th European Conference on MicroFluidics, 2018, Strasbourg, France. (Oral, Best Presentation Award - Ranked No.1)
2. **Wang, Z.**, Orejon, D., Sefiane, K., & Takata, Y. How do single liquid desiccant droplets behave during vapour absorption? Kyushu University Energy Week, 2018, Fukuoka, Japan. (Poster, Best Poster Award)
3. **Wang, Z.**, Zhang, X., & Li, Z. Total heat recovery from industrial flue gases with varied moisture contents using the liquid desiccant technology, ASHRAE Winter Conference, 2017, Las Vegas, US. (Oral, Top Student Paper Award: Only one winner of the Master's level)
4. **Wang, Z.**, Orejon, D., Sefiane, K., & Takata, Y. Coupled thermal transport and mass diffusion during vapor absorption into hygroscopic liquid desiccant droplets, 7th International Symposium on Micro and Nano Technology, 2019, Qingdao, China. (Oral)
5. **Wang, Z.**, Orejon, D., Sefiane, K., & Takata, Y. Coupled thermal transport and mass diffusion during vapor absorption at the droplet scale, 71st Annual Meeting of the American Physical Society's Division of Fluid Dynamics, 2018, Atlanta, US. (Oral)
6. **Wang, Z.**, Orejon, D., Sefiane, K., & Takata, Y. Effect of surface wettability and relative humidity on the vapor absorption process onto liquid desiccant droplets, 10th International Conference on Boiling and Condensation Heat Transfer, 2018, Nagasaki, Japan. (Oral)
7. **Wang, Z.**, Orejon, D., Sefiane, K., & Takata, Y. Vapor absorption phenomenon into sessile liquid desiccant droplets, 16th International Heat Transfer Conference, 2018, Beijing, China. (Poster)
8. **Wang, Z.**, Orejon, D., Sefiane, K., & Takata, Y. デシカント液滴への蒸気吸収：熱物質移動過程の解析 (Vapor absorption into liquid desiccant droplets: Analysis on the heat and mass transfer process), 第 55 回日本伝熱シンポジウム, 2018, Sapporo, Japan. (Oral)
9. **Wang, Z.**, Zhang, X., & Li, Z. Investigation on the coupled heat and mass transfer process between extremely high humidity air and liquid desiccant in the counter-flow adiabatic packed tower, 4th International Forum on Heat Transfer, 2016, Sendai, Japan. (Poster)

List of Figures

List of Tables

Bibliography

[1] Young, T. "III. An essay on the cohesion of fluids." *Philosophical transactions of the royal society of London* 95 (1805): 65-87.

[2] Laplace, P. S., & Celeste, M. "Vol. 4." *Courcier, Paris* (1805).

[3] Gauss, C. F. "Principia generalia Theoriae Figurae Fluidorum in statu Aequilibrii. [General principles of the theory of fluid shapes in a state of equilibrium.]" *Göttingen, Germany: Dieterichs* (1830).

[4] Fournier, J. B., & Cazabat, A. M. "Tears of wine." *EPL (Europhysics Letters)* 20.6 (1992): 517.

[5] Maxwell, J. C. "Scientific papers, ed." *WD Niven, Cambridge* 2 (1890).

[6] Langmuir, I. "The evaporation of small spheres." *Physical review* 12.5 (1918): 368.

[7] Fick, A. "Ueber diffusion." *Annalen der Physik* 170.1 (1855): 59-86.

[8] Picknett, R. G., & Bexon, R. "The evaporation of sessile or pendant drops in still air." *Journal of Colloid and Interface Science* 61.2 (1977): 336-350.

[9] Deegan, R. D., Bakajin, O., Dupont, T. F., Huber, G., Nagel, S. R., & Witten, T. A. "Capillary flow as the cause of ring stains from dried liquid drops." *Nature* 389.6653 (1997): 827.

[10] Deegan, R. D., Bakajin, O., Dupont, T. F., Huber, G., Nagel, S. R., & Witten, T. A. "Contact line deposits in an evaporating drop." *Physical review E* 62.1 (2000): 756.

[11] Deegan, R. D. "Pattern formation in drying drops." *Physical review E* 61.1 (2000): 475.

[12] Hu, H., & Larson, R. G. "Evaporation of a sessile droplet on a substrate." *The Journal of Physical Chemistry B*106.6 (2002): 1334-1344.

[13] Hu, H., & Larson, R. G. "Analysis of the effects of Marangoni stresses on the microflow in an evaporating sessile droplet." *Langmuir* 21.9 (2005): 3972-3980.

[14] Hu, H., & Larson, R. G. "Marangoni effect reverses coffee-ring depositions." *The Journal of Physical Chemistry B*110.14 (2006): 7090-7094.

[15] Sefiane, K., Moffat, J. R., Matar, O. K., & Craster, R. V. "Self-excited hydrothermal waves in evaporating sessile drops." *Applied Physics Letters* 93.7 (2008): 074103.

[16] Karapetsas, G., Matar, O. K., Valluri, P., & Sefiane, K. "Convective rolls and hydrothermal waves in evaporating sessile drops." *Langmuir* 28.31 (2012): 11433-11439.

[17] Dunn, G. J., Wilson, S. K., Duffy, B. R., David, S., & Sefiane, K. "The strong influence of substrate conductivity on droplet evaporation." *Journal of Fluid Mechanics* 623 (2009): 329-351.

[18] Sobac, B., & Brutin, D. "Thermal effects of the substrate on water droplet evaporation." *Physical Review E* 86.2 (2012): 021602.

[19] Sefiane, K., & Bennacer, R. "An expression for droplet evaporation incorporating thermal effects." *Journal of Fluid Mechanics* 667 (2011): 260-271.

[20] David, S., Sefiane, K., & Tadrist, L. "Experimental investigation of the effect of thermal properties of the substrate in the wetting and evaporation of sessile drops." *Colloids and Surfaces A: Physicochemical and Engineering Aspects* 298.1-2 (2007): 108-114.

[21] Orejon, D., Sefiane, K., & Shanahan, M. E. "Stick–slip of evaporating droplets: substrate hydrophobicity and nanoparticle concentration." *Langmuir* 27.21 (2011): 12834-12843.

[22] Moffat, J. R., Sefiane, K., & Shanahan, M. E. "Effect of TiO_2 nanoparticles on contact line stick−slip behavior of volatile drops." *The Journal of Physical Chemistry B* 113.26 (2009): 8860-8866.

[23]Popov, Y. O. "Evaporative deposition patterns: spatial dimensions of the deposit." *Physical Review E* 71.3 (2005): 036313.

[24]McHale, G., Aqil, S., Shirtcliffe, N. J., Newton, M. I., & Erbil, H. Y. "Analysis of droplet evaporation on a superhydrophobic surface." *Langmuir* 21.24 (2005): 11053-11060.

[25]Ma, M., & Hill, R. M. "Superhydrophobic surfaces." *Current opinion in colloid & interface science* 11.4 (2006): 193-202.

[26]Gelderblom, H., Marin, A. G., Nair, H., Van Houselt, A., Lefferts, L., Snoeijer, J. H., & Lohse, D. "How water droplets evaporate on a superhydrophobic substrate." *Physical Review E* 83.2 (2011): 026306.

[27]Tam, D., von Arnim, V., McKinley, G. H., & Hosoi, A. E. "Marangoni convection in droplets on superhydrophobic surfaces." *Journal of Fluid Mechanics* 624 (2009): 101-123.

[28]Dash, S., & Garimella, S. V. "Droplet evaporation dynamics on a superhydrophobic surface with negligible hysteresis." *Langmuir* 29.34 (2013): 10785-10795.

[29]Larson, R. G. "Transport and deposition patterns in drying sessile droplets." *AIChE Journal* 60.5 (2014): 1538-1571.

[30]Fischer, B. J. "Particle convection in an evaporating colloidal droplet." *Langmuir* 18.1 (2002): 60-67.

[31]Bennacer, R., & Sefiane, K. "Vortices, dissipation and flow transition in volatile binary drops." *Journal of Fluid Mechanics*749 (2014): 649-665.

[32]Diddens, C., Tan, H., Lv, P., Versluis, M., Kuerten, J. G. M., Zhang, X., & Lohse, D. "Evaporating pure, binary and ternary droplets: thermal effects and axial symmetry breaking." *Journal of fluid mechanics* 823 (2017): 470-497.

[33]Law, C. K., Xiong, T. Y., & Wang, C. "Alcohol droplet vaporization in humid air." *International Journal of heat and mass transfer* 30.7 (1987): 1435-1443.

[34]Liu, C., Bonaccurso, E., & Butt, H. J. "Evaporation of sessile water/ethanol drops in a controlled environment." *Physical Chemistry Chemical Physics* 10.47 (2008): 7150-7157.

[35]Erbil, H. Y. "Evaporation of pure liquid sessile and spherical suspended drops: A review." Advances in colloid and interface science 170.1-2 (2012): 67-86.

[36]Kovalchuk, N. M., Trybala, A., & Starov, V. M. "Evaporation of sessile droplets." *Current opinion in colloid & interface science*19.4 (2014): 336-342.

[37]Sefiane, K. "Patterns from drying drops." *Advances in colloid and interface science* 206 (2014): 372-381.

[38]Zhong, X., Crivoi, A., & Duan, F. "Sessile nanofluid droplet drying." *Advances in colloid and interface science* 217 (2015): 13-30.

[39]Mampallil, D., & Eral, H. B. "A review on suppression and utilization of the coffee-ring effect." *Advances in colloid and interface science* 252 (2018): 38-54.

[40]Parsa, M., Harmand, S., & Sefiane, K. "Mechanisms of pattern formation from dried sessile drops." *Advances in colloid and interface science* (2018).

[41]Brutin, D., & Starov, V. "Recent advances in droplet wetting and evaporation." *Chemical Society Reviews* 47.2 (2018): 558-585.

[42]Brutin, D. (Ed.). *Droplet wetting and evaporation: from pure to complex fluids*. Academic Press, 2015.

[43]Chua, K. J., Chou, S. K., & Yang, W. M. "Liquid desiccant materials and dehumidifiers – A review." *Renewable & Sustainable Energy Reviews* 56(2016):179-195.

[44]Herold, K. E., Radermacher, R., & Klein, S. A. *Absorption chillers and heat pumps*. CRC press,

2016.

[45] Mei, L., & Dai, Y. J. "A technical review on use of liquid-desiccant dehumidification for air-conditioning application." *Renewable & Sustainable Energy Reviews* 12.3(2008):662-689.

[46] Mazzei, P., Minichiello, F., & Palma, D. "HVAC dehumidification systems for thermal comfort: a critical review." *Applied thermal engineering* 25.5-6 (2005): 677-707.

[47] Yin, Y., Qian, J., & Zhang, X. "Recent advancements in liquid desiccant dehumidification technology." *Renewable and Sustainable Energy Reviews* 31 (2014): 38-52.

[48] Lazzarin, R. M., Longo, G. A., & Piccininni, F. "An open cycle absorption heat pump." *Heat Recovery Systems and CHP* 12.5 (1992): 391-396.

[49] Wang, Z., Zhang, X., & Li, Z. "Evaluation of a flue gas driven open absorption system for heat and water recovery from fossil fuel boilers." *Energy Conversion and Management* 128 (2016): 57-65.

[50] Wang, Z., Zhang, X., Han, J., & Li, Z. "Waste heat and water recovery from natural gas boilers: Parametric analysis and optimization of a flue-gas-driven open absorption system." *Energy Conversion and Management* 154 (2017): 526-537.

[51] Wang, Y., & Yang, S. "Proposal and thermodynamic analysis of a combined open-cycle absorption heat pump and thermal desalination system driven by high-humidity exhaust gas." *Desalination* 448 (2018): 93-102.

[52] Zhao, Kang, et al. "Performance of temperature and humidity independent control air-conditioning system in an office building." *Energy and Buildings* 43.8 (2011): 1895-1903.

[53] Wang, Z., Zhang, X., & Li, Z. "Investigation on the coupled heat and mass transfer process between extremely high humidity air and liquid desiccant in the counter-flow adiabatic packed tower." *International Journal of Heat and Mass Transfer* 110 (2017): 898-907.

[54] Liu, X. H., Zhang, Y., Qu, K. Y., & Jiang, Y. "Experimental study on mass transfer performances of cross flow dehumidifier using liquid desiccant." *Energy Conversion and Management* 47.15 (2006): 2682-2692.

[55] Longo, G. A., & Gasparella, A. "Experimental and theoretical analysis of heat and mass transfer in a packed column dehumidifier/regenerator with liquid desiccant." *International Journal of Heat and Mass Transfer* 48.25 (2005): 5240-5254

[56] Dai, Y. J., & Zhang, H. F. "Numerical simulation and theoretical analysis of heat and mass transfer in a cross flow liquid desiccant air dehumidifier packed with honeycomb paper." *Energy Conversion and Management* 45.9 (2004): 1343-1356.

[57] Al-Farayedhi, A. A., Gandhidasan, P., & Al-Mutairi, M. A. "Evaluation of heat and mass transfer coefficients in a gauze-type structured packing air dehumidifier operating with liquid desiccant." *International Journal of Refrigeration* 25.3 (2002): 330-339.

[58] Liu, X. H., Chang, X. M., Xia, J. J., & Jiang, Y. "Performance analysis on the internally cooled dehumidifier using liquid desiccant." *Building and Environment*44.2 (2009): 299-308.

[59] Yin, Y., Zhang, X., Wang, G., & Luo, L. "Experimental study on a new internally cooled/heated dehumidifier/regenerator of liquid desiccant systems." *International Journal of Refrigeration* 31.5 (2008): 857-866.

[60] Jain, S., Tripathi, S., & Das, R. S. "Experimental performance of a liquid desiccant dehumidification system under tropical climates." *Energy Conversion and Management* 52.6 (2011): 2461-2466.

[61] Zurigat, Y. H., Abu-Arabi, M. K., & Abdul-Wahab, S. A. "Air dehumidification by triethylene glycol desiccant in a packed column." *Energy Conversion and Management* 45.1 (2004): 141-155.

[62] Longo, G. A., & Gasparella, A. "Experimental and theoretical analysis of heat and mass transfer

in a packed column dehumidifier/regenerator with liquid desiccant." *International Journal of Heat and Mass Transfer* 48.25-26 (2005): 5240-5254.

[63] Liu, X. H., Zhang, Y., Qu, K. Y., & Jiang, Y. "Experimental study on mass transfer performances of cross flow dehumidifier using liquid desiccant." *Energy Conversion and Management* 47.15-16 (2006): 2682-2692.

[64] Moon, C. G., Bansal, P. K., & Jain, S. "New mass transfer performance data of a cross-flow liquid desiccant dehumidification system." *International Journal of Refrigeration*32.3 (2009): 524-533.

[65] Zhang, L., Hihara, E., Matsuoka, F., & Dang, C. "Experimental analysis of mass transfer in adiabatic structured packing dehumidifier/regenerator with liquid desiccant." *International Journal of Heat and Mass Transfer*53.13-14 (2010): 2856-2863.

[66] Gao, W. Z., Liu, J. H., Cheng, Y. P., & Zhang, X. L. "Experimental investigation on the heat and mass transfer between air and liquid desiccant in a cross-flow dehumidifier." *Renewable Energy* 37.1 (2012): 117-123.

[67] Abdul-Wahab, S. A., Abu-Arabi, M. K., & Zurigat, Y. H. "Effect of structured packing density on performance of air dehumidifier." *Energy Conversion and Management* 45.15-16 (2004): 2539-2552.

[68] Bonn, D., Eggers, J., Indekeu, J., Meunier, J., & Rolley, E. "Wetting and spreading." *Reviews of modern physics* 81.2 (2009): 739.

[69] Hu, H., & Larson, R. G. "Evaporation of a sessile droplet on a substrate." *The Journal of Physical Chemistry B*106.6 (2002): 1334-1344.

[70] Maxwell, J. C. *The Scientific Papers of James Clerk Maxwell...* Vol. 2. University Press, 1890.

[71] Deegan, R. D., Bakajin, O., Dupont, T. F., Huber, G., Nagel, S. R., & Witten, T. A. "Capillary flow as the cause of ring stains from dried liquid drops." *Nature* 389.6653 (1997): 827.

[72] Deegan, R. D., Bakajin, O., Dupont, T. F., Huber, G., Nagel, S. R., & Witten, T. A. "Contact line deposits in an evaporating drop." *Physical review E* 62.1 (2000): 756.

[73] Hu, H., & Larson, R. G. "Analysis of the microfluid flow in an evaporating sessile droplet." *Langmuir* 21.9 (2005): 3963-3971.

[74] Weon, B. M., & Je, J. H. "Self-pinning by colloids confined at a contact line." *Physical review letters* 110.2 (2013): 028303.

[75] Sefiane, K., & Bennacer, R. "An expression for droplet evaporation incorporating thermal effects." *Journal of Fluid Mechanics* 667 (2011): 260-271.

[76] Nguyen, T. A., Nguyen, A. V., Hampton, M. A., Xu, Z. P., Huang, L., & Rudolph, V. "Theoretical and experimental analysis of droplet evaporation on solid surfaces." *Chemical engineering science* 69.1 (2012): 522-529.

[77] Dunn, G. J., Wilson, S. K., Duffy, B. R., David, S., & Sefiane, K. "A mathematical model for the evaporation of a thin sessile liquid droplet: comparison between experiment and theory." *Colloids and Surfaces A: Physicochemical and Engineering Aspects* 323.1-3 (2008): 50-55.

[78] Sefiane, K., Wilson, S. K., David, S., Dunn, G. J., & Duffy, B. R. "On the effect of the atmosphere on the evaporation of sessile droplets of water." *Physics of fluids* 21.6 (2009): 062101.

[79] Xu, X., & Luo, J. "Marangoni flow in an evaporating water droplet." *Applied Physics Letters* 91.12 (2007): 124102.

[80] Xu, X., Luo, J., & Guo, D. "Criterion for reversal of thermal Marangoni flow in drying drops." Langmuir 26.3 (2009): 1918-1922.

[81] Ristenpart, W. D., Kim, P. G., Domingues, C., Wan, J., & Stone, H. A. "Influence of substrate conductivity on circulation reversal in evaporating drops." *Physical Review Letters* 99.23 (2007): 234502.

[82] Girard, F., Antoni, M., Faure, S., & Steinchen, A. "Evaporation and Marangoni driven convection in small heated water droplets." *Langmuir* 22.26 (2006): 11085-11091.

[83] Girard, F., & Antoni, M. "Influence of substrate heating on the evaporation dynamics of pinned water droplets." *Langmuir* 24.20 (2008): 11342-11345.

[84] Soltman, D., & Subramanian, V. "Inkjet-printed line morphologies and temperature control of the coffee ring effect." *Langmuir* 24.5 (2008): 2224-2231.

[85] Thokchom, A. K., Gupta, A., Jaijus, P. J., & Singh, A. "Analysis of fluid flow and particle transport in evaporating droplets exposed to infrared heating." *International Journal of Heat and Mass Transfer* 68 (2014): 67-77.

[86] Hendarto, E., & Gianchandani, Y. B. "Size sorting of floating spheres based on Marangoni forces in evaporating droplets." *Journal of Micromechanics and Microengineering* 23.7 (2013): 075016.

[87] Kita, Y., Askounis, A., Kohno, M., Takata, Y., Kim, J., & Sefiane, K. "Induction of Marangoni convection in pure water drops." Applied Physics Letters 109.17 (2016): 171602.

[88] Askounis, A., Kita, Y., Kohno, M., Takata, Y., Koutsos, V., & Sefiane, K. "Influence of Local Heating on Marangoni Flows and Evaporation Kinetics of Pure Water Drops." Langmuir 33.23 (2017): 5666-5674.

[89] Josyula, T., Wang, Z., Askounis, A., Orejon, D., Harish, S., Takata, Y., ... & Pattamatta, A. "Evaporation kinetics of pure water drops: Thermal patterns, Marangoni flow, and interfacial temperature difference." *Physical Review E* 98.5 (2018): 052804.

[90] Bansal, L., Chakraborty, S., & Basu, S. "Confinement-induced alterations in the evaporation dynamics of sessile droplets." *Soft Matter* 13.5 (2017): 969-977.

[91] Xu, W., Leeladhar, R., Kang, Y. T., & Choi, C. H. "Evaporation kinetics of sessile water droplets on micropillared superhydrophobic surfaces." *Langmuir* 29.20 (2013): 6032-6041.

[92] Askounis, A., Orejon, D., Koutsos, V., Sefiane, K., & Shanahan, M. E. "Nanoparticle deposits near the contact line of pinned volatile droplets: size and shape revealed by atomic force microscopy." *Soft Matter* 7.9 (2011): 4152-4155.

[93] Antonini, C., Lee, J. B., Maitra, T., Irvine, S., Derome, D., Tiwari, M. K., Carmeliet, J., Poulikakos, D. "Unraveling wetting transition through surface textures with X-rays: Liquid meniscus penetration phenomena." *Scientific Reports* 4 (2014): 4055.

[94] Dash, S., & Garimella, S. V. "Droplet evaporation on heated hydrophobic and superhydrophobic surfaces." *Physical Review E* 89.4 (2014): 042402.

[95] Gelderblom, H., Marin, A. G., Nair, H., Van Houselt, A., Lefferts, L., Snoeijer, J. H., & Lohse, D. "How water droplets evaporate on a superhydrophobic substrate." *Physical Review E* 83.2 (2011): 026306.

[96] Sobac, B., & Brutin, D. "Triple-line behavior and wettability controlled by nanocoated substrates: influence on sessile drop evaporation." *Langmuir* 27.24 (2011): 14999-15007.

[97] Stauber, J. M., Wilson, S. K., Duffy, B. R., & Sefiane, K. "Evaporation of droplets on strongly hydrophobic substrates." *Langmuir* 31.12 (2015): 3653-3660.

[98] Soulié, V., Karpitschka, S., Lequien, F., Prené, P., Zemb, T., Moehwald, H., & Riegler, H. "The evaporation behavior of sessile droplets from aqueous saline solutions." *Physical Chemistry Chemical Physics* 17.34 (2015): 22296-22303.

[99] Zhong, X., Ren, J., & Duan, F. "Wettability effect on evaporation dynamics and crystalline patterns of sessile saline droplets." *The Journal of Physical Chemistry B* 121.33 (2017): 7924-7933.

[100] Kuznetsov, G. V., Feoktistov, D. V., Orlova, E. G., Misyura, S. Y., Morozov, V. S., & Islamova, A. G. "Evaporation modes of LiBr, $CaCl_2$, LiCl, NaCl aqueous salt solution droplets on aluminum

surface." *International Journal of Heat and Mass Transfer* 126 (2018): 161-168.

[101]Brenn, G. "Concentration fields in evaporating droplets." *International Journal of Heat and Mass Transfer* 48.2 (2005): 395-402.

[102]Misyura, S. Y. "Non-isothermal evaporation in a sessile droplet of water-salt solution." International Journal of Thermal Sciences 124 (2018): 76-84.

[103]Misyura, S. Y. "Evaporation of a sessile water drop and a drop of aqueous salt solution." Scientific reports 7.1 (2017): 14759.

[104]Shahidzadeh-Bonn, N., Rafaı, S., Bonn, D., & Wegdam, G. "Salt crystallization during evaporation: impact of interfacial properties." Langmuir 24.16 (2008): 8599-8605.

[105]Shahidzadeh, N., Schut, M. F., Desarnaud, J., Prat, M., & Bonn, D. "Salt stains from evaporating droplets." Scientific reports 5 (2015): 10335.

[106]McBride, S. A., Dash, S., & Varanasi, K. K. "Evaporative crystallization in drops on superhydrophobic and liquid-impregnated surfaces." Langmuir 34.41 (2018): 12350-12358.

[107]Kaya, D., Belyi, V. A., & Muthukumar, M. "Pattern formation in drying droplets of polyelectrolyte and salt." The Journal of chemical physics 133.11 (2010): 114905.

[108]Gorr, Heather Meloy, et al. "Salt-induced pattern formation in evaporating droplets of lysozyme solutions." *Colloids and Surfaces B: Biointerfaces* 103 (2013): 59-66.

[109]Harrington, George F., James M. Campbell, and Hugo K. Christenson. "Crystal patterns created by rupture of a thin film." *Crystal Growth & Design* 13.11 (2013): 5062-5067.

[110]Sefiane, K. "Patterns from drying drops." Advances in colloid and interface science 206 (2014): 372-381.

[111]Parsa, M., Harmand, S., & Sefiane, K. "Mechanisms of pattern formation from dried sessile drops." Advances in colloid and interface science (2018).

[112]De Gennes, P. G. "Wetting: statics and dynamics." *Reviews of modern physics* 57.3 (1985): 827.

[113]Dussan, E. B., & Davis, S. H. "On the motion of a fluid-fluid interface along a solid surface." *Journal of Fluid Mechanics* 65.1 (1974): 71-95.

[114]Greenspan, H. P. "On the motion of a small viscous droplet that wets a surface." *Journal of Fluid Mechanics* 84.1 (1978): 125-143.

[115]Ehrhard, P., & Davis, S. H. "Non-isothermal spreading of liquid drops on horizontal plates." *Journal of Fluid Mechanics* 229 (1991): 365-388.

[116]Tanner, L. H. "The spreading of silicone oil drops on horizontal surfaces." *Journal of Physics D: Applied Physics* 12.9 (1979): 1473.

[117]Cazabat, A. M., & Stuart, M. C. "Dynamics of wetting: effects of surface roughness." *The Journal of Physical Chemistry*90.22 (1986): 5845-5849.

[118]Chen, J. D., & Wada, N. "Wetting dynamics of the edge of a spreading drop." *Physical review letters* 62.26 (1989): 3050.

[119]Haley, P. J., & Miksis, M. J. "The effect of the contact line on droplet spreading." *Journal of Fluid Mechanics*223 (1991): 57-81.

[120]Hocking, L. M. "Rival contact-angle models and the spreading of drops." Journal of Fluid Mechanics 239 (1992): 671-681.

[121]Ehrhard, P. "Experiments on isothermal and non-isothermal spreading." *Journal of Fluid Mechanics* 257 (1993): 463-483.

[122]Anderson, D. M., & Davis, S. H. "The spreading of volatile liquid droplets on heated surfaces." *Physics of Fluids* 7.2 (1995): 248-265.

[123]Wayner Jr, P. C. "The effect of interfacial mass transport on flow in thin liquid films." *Colloids and Surfaces* 52 (1991): 71-84.

[124]Carey, V. P. *Liquid vapor phase change phenomena: an introduction to the thermophysics of vaporization and condensation processes in heat transfer equipment*. CRC Press, 2018: 112-120.

[125]Ajaev, V. S. "Spreading of thin volatile liquid droplets on uniformly heated surfaces." *Journal of Fluid Mechanics* 528 (2005): 279-296.

[126]Moosman, S., & Homsy, G. M. "Evaporating menisci of wetting fluids." *Journal of Colloid and Interface Science* 73.1 (1980): 212-223.

[127]Gomba, J. M., & Homsy, G. M. "Regimes of thermocapillary migration of droplets under partial wetting conditions." *Journal of Fluid Mechanics* 647 (2010): 125-142.

[128]Matar, O. K., Craster, R. V., & Sefiane, K. "Dynamic spreading of droplets containing nanoparticles." *Physical Review E* 76.5 (2007): 056315.

[129]Craster, R. V., Matar, O. K., & Sefiane, K. "Pinning, retraction, and terracing of evaporating droplets containing nanoparticles." *Langmuir* 25.6 (2009): 3601-3609.

[130]Karapetsas, G., Craster, R. V., & Matar, O. K. "On surfactant-enhanced spreading and superspreading of liquid drops on solid surfaces." *Journal of Fluid Mechanics* 670 (2011): 5-37.

[131]Karapetsas, G., Craster, R. V., & Matar, O. K. "Surfactant-driven dynamics of liquid lenses." *Physics of Fluids*23.12 (2011): 122106.

[132]Maki, K. L., & Kumar, S. "Fast evaporation of spreading droplets of colloidal suspensions." *Langmuir* 27.18 (2011): 11347-11363.

[133]Karapetsas, G., Sahu, K. C., & Matar, O. K. "Evaporation of sessile droplets laden with particles and insoluble surfactants." *Langmuir* 32.27 (2016): 6871-6881.

[134]Espín, L., & Kumar, S. "Sagging of evaporating droplets of colloidal suspensions on inclined substrates." *Langmuir* 30.40 (2014): 11966-11974.

[135]Karapetsas, G., Sahu, K. C., & Matar, O. K. "Effect of contact line dynamics on the thermocapillary motion of a droplet on an inclined plate." *Langmuir* 29.28 (2013): 8892-8906.

[136]Karapetsas, George, et al. "Thermocapillary-driven motion of a sessile drop: effect of non-monotonic dependence of surface tension on temperature." *Langmuir* 30.15 (2014): 4310-4321.

[137]Patek, J., & Klomfar, J. "A computationally effective formulation of the thermodynamic properties of LiBr–H_2O solutions from 273 to 500 K over full composition range." *International Journal of Refrigeration* 29.4 (2006): 566-578.

[138]Wang, Z., Orejon, D., Sefiane, K., & Takata, Y. "Water vapor uptake into hygroscopic lithium bromide desiccant droplets: mechanisms of droplet growth and spreading." *Physical Chemistry Chemical Physics* 21.3 (2019): 1046-1058.

[139]Hopkins, R. J., & Reid, J. P. "Evaporation of ethanol/water droplets: examining the temporal evolution of droplet size, composition and temperature." *The Journal of Physical Chemistry A* 109.35 (2005): 7923-7931.

[140]Liu, C., Bonaccurso, E., & Butt, H. J. "Evaporation of sessile water/ethanol drops in a controlled environment." *Physical Chemistry Chemical Physics* 10.47 (2008): 7150-7157.

[141]Kita, Y., Okauchi, Y., Fukatani, Y., Orejon, D., Kohno, M., Takata, Y., & Sefiane, K. "Quantifying vapor transfer into evaporating ethanol drops in humid atmosphere." *Physical Chemistry Chemical Physics* (2018).

[142]Wimby, J. M., & Berntsson, T. S. "Viscosity and density of aqueous solutions of lithium bromide, lithium chloride, zinc bromide, calcium chloride and lithium nitrate. 1. Single salt solutions." *Journal of Chemical and Engineering Data* 39.1 (1994): 68-72.

[143]Cussler, E. L. *Diffusion: mass transfer in fluid systems.* Cambridge university press, 2009.

[144]Lobo, V. M. M., Ribeiro, A. C. F., & Verissimo, L. M. P. "Diffusion coefficients in aqueous solutions of potassium chloride at high and low concentrations." *Journal of molecular liquids* 78.1-2 (1998): 139-149.

[145]Harned, H. S., & Levy, A. L. "The Differential Diffusion Coefficient of Calcium Chloride in Dilute Aqueous Solutions at 25°." *Journal of the American Chemical Society* 71.8 (1949): 2781-2783.

[146]Mitra, S., & Mitra, S. K. "Understanding the early regime of drop spreading." *Langmuir* 32.35 (2016): 8843-8848.

[147]Young, T. "An essay on the cohesion of fluids." *Philosophical Transactions of the Royal Society of London* 95 (1805): 65-87.

[148]Yao, W., Bjurstroem, H., & Setterwall, F. "Surface tension of lithium bromide solutions with heat-transfer additives." *Journal of chemical and engineering data* 36.1 (1991): 96-98.

[149]Gittens, G. J. "Variation of surface tension of water with temperature." *Journal of Colloid and Interface Science* 30.3 (1969): 406-412.

[150]Tarasevich, Y.I. & Aksenenko, E.V. J. "Interaction of water molecules with hydrophilic and hydrophobic surfaces of colloid particles." *Journal of Water Chemistry and Technology* 37.5 (2015): 224-229.

[151]Bernett, Marianne K., and W. A. Zisman. "Effect of adsorbed water on wetting properties of borosilicate glass, quartz, and sapphire." *Journal of colloid and interface science* 29.3 (1969): 413-423.

[152]Chengara, A., Nikolov, A. D., & Wasan, D. T. "Spreading of a water drop triggered by the surface tension gradient created by the localized addition of a surfactant." *Industrial & engineering chemistry research* 46.10 (2007): 2987-2995.

[153]Bertozzi, A. L., Münch, A., Fanton, X., & Cazabat, A. M. "Contact line stability and "undercompressive shocks" in driven thin film flow." *Physical review letters* 81.23 (1998): 5169.

[154]Leger, L., Erman, M., Guinet-Picard, A. M., Ausserre, D., & Strazielle, C. "Precursor film profiles of spreading liquid drops." *Physical Review Letters* 60.23(1988):2390-2393.

[155]Kavehpour, H. P., Ovryn, B., & McKinley, G. H. "Microscopic and Macroscopic Structure of the Precursor Layer in Spreading Viscous Drops." *Physical Review Letters* 91.19(2003):196104.

[156]Xu, H., Shirvanyants, D., Beers, K., Matyjaszewski, K., Rubinstein, M., & Sheiko, S. S. "Molecular motion in a spreading precursor film." *Physical review letters* 93.20 (2004): 206103.

[157]Hoang, A., & Kavehpour, H. P. "Dynamics of nanoscale precursor film near a moving contact line of spreading drops." *Physical Review Letters* 106.25(2011):254501.

[158]Ghiradella, H., Radigan, W., & Frisch, H. L. "Electrical resistivity changes in spreading liquid films." *Journal of Colloid and Interface Science* 51.3 (1975): 522-526.

[159]Carré, A., Gastel, J. C., & Shanahan, M. E. "Viscoelastic effects in the spreading of liquids." *Nature* 379.6564(1996):432-434.

[160]Wang, Z., Orejon, D., Sefiane, K., & Takata, Y. "Coupled thermal transport and mass diffusion during vapor absorption into hygroscopic liquid desiccant droplets." *International Journal of Heat and Mass Transfer* 134 (2019): 1014-1023.

[161]Nguyen, T. A., Hampton, M. A., & Nguyen, A. V. "Evaporation of nanoparticle droplets on smooth hydrophobic surfaces: the inner coffee ring deposits." *The Journal of Physical Chemistry C* 117.9 (2013): 4707-4716.

[162]Kim, J. H., Ahn, S. I., Kim, J. H., & Zin, W. C. "Evaporation of water droplets on polymer surfaces." *Langmuir* 23.11 (2007): 6163-6169.

[163]Bhardwaj, R., Fang, X., Somasundaran, P., & Attinger, D. "Self-assembly of colloidal particles from evaporating droplets: role of DLVO interactions and proposition of a phase diagram." *Langmuir* 26.11 (2010): 7833-7842.

[164]Pan, Z., Dash, S., Weibel, J. A., & Garimella, S. V. "Assessment of water droplet evaporation mechanisms on hydrophobic and superhydrophobic substrates." *Langmuir* 29.51 (2013): 15831-15841.

[165]Ristenpart, W. D., Kim, P. G., Domingues, C., Wang, J., & Stone, H. A. "Influence of substrate conductivity on circulation reversal in evaporating drops." *Physical Review Letters* 99 (2007): 234502.

[166]Dill, K., & Bromberg, S. *Molecular driving forces: statistical thermodynamics in biology, chemistry, physics, and nanoscience.* Garland Science: New York 2nd Edition, 2010.

[167]Lee, R. J., DiGuilio, R. M., Jeter, S. M., & Teja, A. S. "Properties of lithium bromide-water solutions at high temperatures and concentrations I: Thermal Conductivity." *ASHRAE Transactions* 98.2 (1992): 702-708.

[168]Yao, W., Bjurstroem, H., & Setterwall, F. "Surface tension of lithium bromide solutions with heat-transfer additives." *Journal of chemical and engineering data* 36.1 (1991): 96-98.

[169]Persad, A. H., & Ward, C. A. "Expressions for the evaporation and condensation coefficients in the Hertz-Knudsen relation." *Chemical reviews* 116.14 (2016): 7727-7767.

[170]Henry, M. "Nanocrystals from Solutions and Gels." Encyclopedia of Nanoscience and Nanotechnology. Vol. 6. No. 586. *American Scientific Publishers*, 2004. 555-586.

[171]Hadj-Achour, M., & Brutin, D. "Fractal pattern formation in nanosuspension sessile droplets via evaporation-spreading on a glass substrate." *Colloids and Interface Science Communications* 1 (2014): 43-46.